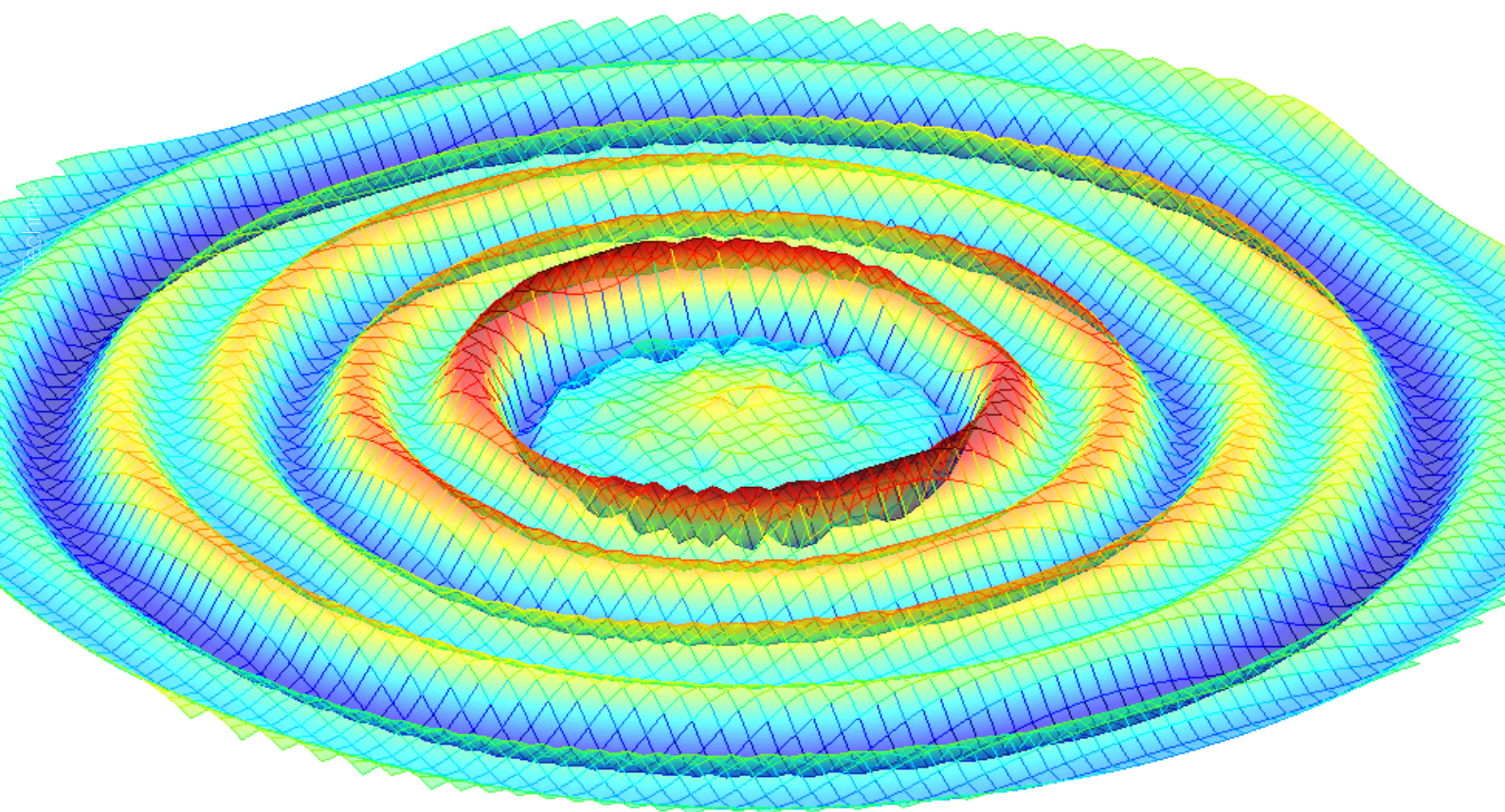


# Soil structure interaction for shallow foundations in 2D and 3D

A semi-analytic linear approach

T. Molenkamp





# Soil structure interaction for shallow foundations in 2D and 3D

A semi-analytic linear approach

by

T. Molenkamp

to obtain the degree of Master of Science  
at the Delft University of Technology,  
to be defended publicly on Friday July 11, 2018 at 01:00 PM.

Student number: 4521773  
Project duration: September 1, 2017 – July 11, 2018  
Thesis committee: Prof. dr. ir. A.V. Metrikine, TU Delft, committee chairman  
Dr. ir. A. Tsouvalas, TU Delft, daily supervisor  
Ir. F. Besseling, Witteveen + Bos, supervisor  
Dr. ir. K.N. van Dalen, TU Delft

*This thesis is confidential and cannot be made public until July 11, 2019.*

An electronic version of this thesis is available at <http://repository.tudelft.nl/>.





# Preface

This thesis is written in order to obtain the degree of Master of Science in Civil Engineering from Delft University of Technology. The research is carried out in collaboration with Witteveen+Bos and the Faculty of Civil Engineering.

I would like to express my gratefulness to my committee: Prof. dr. ir. A.V. Metrikine, Dr. ir. A. Tsouvalas, Ir. F. Besseling and Dr. ir. K. van Dalen. I want to thank you for your time, your sincere interest and help during this thesis. Without your help and motivation, it would be a lot more difficult for me to finish this thesis. Furthermore, I would like to thank my colleges from Witteveen+Bos, who make working on this thesis at the office bearable and enjoyable. I have learned a lot, explored my interest and enjoyed the process of writing this thesis, because of you. A special note to Floris and Apostolos. Floris tried to understand everything I worked on next to his daily job and even during the weekends and evenings he was available for discussion, thank you for that. Apostolos, I have learned a lot from you, I am thankful for your flexibility, especially the time that I could visit at your place after an unfortunate cancellation of a meeting through circumstances.

This thesis is to finalize my study, but a study includes more than writing a thesis. The last seven years were extremely learning, but more than all a lot of fun. I would like to thank my parents and family for giving me the change to do what I thought is right and supporting me in the choices I have made. That made my study a lot easier. I am grateful to all the friends I made through my study. The people were I spent most of my time with the last seven years. In special I want to thank my friends; from Het Dispuut Pegasus, where I spent most Sunday evenings with at SSRE, my fellow SSRE board members '14-'15, one of the best years of my life and my room-mates and friends from Delft, you made my master in a new city more enjoyable than I had expect on forehand.

Last but not least, I want to thank my girlfriend Sofia. You have supported me for the last couple of years, but especially during the last year. I am thankful for your patient and for the fact that you know what I need, when it gets a bit difficult. You have given me the freedom but also motivation I needed last year. I could not wish for a better place to go after work than home.

Friends, family, committee and colleges I could not have done this without you, thank you for that.

*In memoriam, I would like to thank my beloved grandfather, who passed away today.*

*T. Molenkamp  
Delft,  
July 5, 2018*



# Abstract

Soil structure interaction is a phenomena often neglected or under estimated in earthquake engineering. From the point of few of many engineers, neglecting soil structure interaction is seen as a conservative and save way to calculate. However, soil structure interaction can have great effects on the dynamic behaviour of the superstructure. Especially for large and heavy superstructures, e.g. liquid storage tanks and power plants, soil structure interaction is of great importance.

Modelling techniques to capture this phenomena are often over simplified or need a lot of computational effort. Therefore, it is proposed to develop a semi-analytical linear elastic model, which describes the soil structure interaction based on fundamental physics. The thesis outline is as follows:

Chapter 1 states the problem definition and objectives of this thesis. The research questions are mentioned and the research approach to answer these questions and fulfil the objective are described here.

Chapter 2 gives an introduction about the fundamental knowledge needed for this thesis. An introduction about earthquakes is given, including the different waves that are generated by earthquakes. It gives insight in the principles of dynamics. Furthermore, other modelling techniques are explained, including their pros and cons.

In chapter 3, the soil behaviour is described for a 2D plane strain case. This is done based on Green's functions. The soil behaviour is described for a single layer on bedrock. Flexibility function of the soil are derived in the frequency-wavenumber domain and transformed back by making use of contour integration and the residue theorem. The convergence of the solution is verified and the soil behavior is evaluated.

In chapter 4, a inextensible bending strip is combined with the soil model. This chapter gives insight in how both are combined. The model is validated by literature. A case study is proceeded including different loads at different frequencies. Furthermore, the influence of the flexibility of the strip on the stiffness and damping of the system is evaluated.

Chapter 5 and 6 follow the same procedure as chapter 3 and 4. Instead of the 2D plane strain case, a 3D model is developed for the soil. The model is coupled to a inextensible bending plate. The behaviour of the coupled model is evaluated and validated in these chapters.

Chapter 7 summarizes the conclusions made during this thesis. It discusses the choices made and give recommendation about further research.



# Contents

<b>1</b>	<b>Problem definition</b>	<b>1</b>
1.1	Objective . . . . .	2
1.2	Research question . . . . .	2
1.3	Subquestions . . . . .	2
1.4	Research approach . . . . .	2
<b>2</b>	<b>Literature</b>	<b>5</b>
2.1	Earthquakes . . . . .	5
2.1.1	Cause of an earthquake . . . . .	5
2.1.2	Wave types . . . . .	7
2.2	Dynamic analysis . . . . .	9
2.2.1	Structural dynamic analysis methods . . . . .	9
2.2.2	Time and frequency domain . . . . .	9
2.2.3	Damped mass-spring systems . . . . .	10
2.2.4	Continuum systems . . . . .	12
2.3	Dynamic soil structure interaction models . . . . .	13
2.3.1	Simplified spring model . . . . .	13
2.3.2	Winkler model . . . . .	13
2.3.3	Linear elastic model . . . . .	14
2.3.4	The wave equation . . . . .	15
<b>3</b>	<b>2D plane-strain soil model</b>	<b>17</b>
3.1	The decomposition of the wave equation by its potentials . . . . .	19
3.2	The stress and displacement field . . . . .	21
3.2.1	Free vibration solution . . . . .	22
3.2.2	Root-finder algorithm . . . . .	23
3.3	Force-displacement relation of the surface . . . . .	25
3.4	Contour integration . . . . .	28
3.4.1	Residue in a complex analysis . . . . .	28
3.5	Solution in the frequency-space domain . . . . .	30
3.5.1	2D soil stiffness matrix . . . . .	32
3.6	Convergence of the 2D soil problem . . . . .	34
3.7	Validation for the static case ( $\omega = 0$ ) . . . . .	36
3.8	Frequency dependency of the soil stiffness . . . . .	38
<b>4</b>	<b>2D Soil structure interaction</b>	<b>41</b>
4.1	General equations of a free-edge Euler Bernoulli beam . . . . .	41
4.2	Homogeneous solution of a free-edge EB beam . . . . .	43
4.3	Soil stiffness matrix decomposition . . . . .	45
4.4	The orthogonality principle . . . . .	47
4.5	2D SSI case study . . . . .	48
4.6	Convergence of the 2D model . . . . .	52
4.7	Influence of the foundation stiffness . . . . .	54
<b>5</b>	<b>3D model soil model</b>	<b>57</b>
5.1	Hankel-transform of the wave equation . . . . .	57
5.2	Homogeneous boundary conditions . . . . .	62
5.3	A cylindrical symmetric vertical load . . . . .	64
5.3.1	Contour integration for the cylindrical symmetric load . . . . .	65
5.4	An antisymmetric horizontal load . . . . .	67
5.4.1	Contour integration for the antisymmetric load . . . . .	68

5.5	Flexibility functions . . . . .	71
5.6	Validation . . . . .	74
5.6.1	Static stiffness . . . . .	75
5.6.2	Dynamic stiffness . . . . .	75
<b>6</b>	<b>3D Soil structure interaction</b>	<b>79</b>
6.1	SSI of a plate in cylindrical coordinates . . . . .	79
6.1.1	Free-edge plate equations . . . . .	80
6.1.2	Discretization of a circular area . . . . .	82
6.2	Orthogonality of the structural modes . . . . .	83
6.3	3D SSI case study . . . . .	84
6.4	Influence of the flexibility of a circular plate . . . . .	91
<b>7</b>	<b>Conclusions, recommendations and discussion</b>	<b>95</b>
7.1	Conclusions. . . . .	95
7.2	Recommendations . . . . .	98
7.3	Discussion . . . . .	99
<b>A</b>	<b>Rewriting the Hankel transform</b>	<b>101</b>
A.1	An integral over a Bessel J transform premultiplied with an antisymmetric function . . . . .	101
A.1.1	A cylindrical symmetric load (n=0). . . . .	101
A.1.2	An antisymmetric case (n=1). . . . .	102
A.2	A integral over a Bessel J transform premultiplied with a symmetric function. . . . .	102
A.2.1	A cylindrical symmetric load (n=0). . . . .	103
A.2.2	An antisymmetric case (n=1). . . . .	103
A.2.3	General solution . . . . .	104
<b>B</b>	<b>Derivation of the potential representation of the displacement by Helmholtz decomposition</b>	<b>105</b>
	<b>Bibliography</b>	<b>107</b>

# Nomenclature

## Abbreviations

FE	Finite element
P-	Primary
PGA	Peak ground acceleration
S-	Secondary
SDOF	Single degree of freedom
SSI	Soil structure interaction

## Greek symbols

$\chi$	Helmholtz potential related to the SH-wave
$\Delta$	Determinant of the kernel corresponding to the homogeneous boundary conditions of a single layer
$\epsilon_{ij}$	Normal or shear strain
$\lambda$	Lamé constant, based on the Poisson's ratio and Young's modulus of a linear elastic material
$\lambda$	The wavelength of a wave
$\mu$	Lamé constant/Shear modulus, based on the Poisson's ratio and Young's modulus of a linear elastic material
$\nu$	Poisson's ratio
$\omega$	Angular frequency
$\omega_n$	Natural angular frequency
$\omega_{p,1}$	Frequency corresponding to the first fundamental compressional mode of the soil layer
$\omega_{s,1}$	Frequency corresponding to the first fundamental shear mode of the soil layer
$\phi$	Helmholtz potential related to the P-wave
$\phi_j$	Modal shape j
$\psi$	Helmholtz potential related to the SV-wave
$\rho$	Material density
$\epsilon$	Volume strain

## Latin symbols

$K_s$	The frequency dependent soil stiffness matrix
$A$	Area
$a_0$	Normalized frequency over half the width of the foundation and the shear wave speed
$a_0$	Normalized frequency over half the width of the foundation and the shear wave speed
$b$	Width of a single 2D plane-strain element

$b_j$	Body force in direction j
$c$	Damping
$c_0$	Normalized damping coefficient
$c_p$	P-wave group velocity
$c_s$	S-wave group velocity
$E$	Young's modulus
$F$	External force
$f_{ii}$	Numerator of the flexibility function with index ii
$h$	Depth of the single layer on bedrock (stratum)
$I$	Second moment of area
$k$	Stiffness
$K_j$	SDOF vertical, horizontal or rocking stiffness, for indices j = z,x,r
$k_m$	Roots located in the php
$k_n$	Roots located in the nhp
$k_p$	P-wavenumber found by dividing the angular frequency over the P-wave group velocity
$k_s$	S-wavenumber found by dividing the angular frequency over the S-wave group velocity
$k_x, k_y, k_z$	Wavenumber in respectively x,y and z direction
$K_{ij}$	Component of the stiffness matrix corresponding to a displacement in j due to a force in i
$L$	Length
$m$	Mass
$M_{ml}$	Matrix describing the orthogonality of the modes m and l
$q$	Distributed external load
$r_e$	Radius of an element
$r_p$	Radius of the plate
$R_{ij}$	Flexibility function that relates force in direction i with a displacement in direction j
$S_i$	Nodal force in i
$T$	Period
$t$	Time
$u_j$	Displacement in direction of index j, for indices j = x, y, z, r or $\theta$



## Problem definition

Soil structure interaction (SSI) analysis evaluates the interaction between structure, foundation and soil. When a structure is subjected to a dynamic load, it interacts with the soil and changes the motion of the soil. Vice versa, the soil motion due to an earthquake excites a structure, but the structure will never exactly follow the soils free field movement of the soil, even when the foundation is embedded. The inability of the foundation to match the free field motion of the soil is called the kinematic interaction. Generally the SSI can be divided into two principles: kinematic interaction and inertial interaction. The inertial interaction follows from the inertia of accelerated mass of the super structure. These inertial forces transmitted to the soil through the super structure and foundation, causing additional deformations of the soil (Wolf, 1985).

Conventionally, SSI is not taken into account during the dynamic evaluation of a structure. In conventionally belief of engineers, SSI is believed to be beneficial and can be neglected in conservative design. Neglecting SSI is reasonable for light and small structures on a rather stiff soil. However, SSI is of greater importance for heavy, large and relatively stiff structures, e.g. high-rise buildings, power plants, liquid-storage tanks, build on relative soft soil. In general, the effective damping ratio will increase by considering the effects of SSI. For low-level excitation, the kinematic effects will typically be dominant causing lengthening of the system period and increase in radiation damping. However, for strong excitation, the inertial effects will dominate (Wolf, 1985).

Past earthquakes have confirmed that the seismic behaviour of a structure is not only influenced by the structure itself but also heavily by the surrounding soil. After the 1995 Kobe earthquake, the influence of SSI on the collapse of the Hanshin Expressway, i.e. a 4-lane elevated highway, has been researched. The influence was double and detrimental: the spectral acceleration at low frequencies was amplified and the natural period of the building was elongated due to the SSI. It is also shown from numerical examples that SSI does not always lead to beneficial effects when considering the seismic response of a structure. Soft soil elongates both the period of seismic waves and the increase in natural period of the structure, which may lead to resonance for low-frequency ground motion (Mylonakis et al., 2006).

Problems with practical application of SSI principles are rooted in bad understanding of the principles, incomprehensible literature about the subject, the absence of proper guidelines or over simplification of codes and standards on the principles (Consultants Joint Venture, 2012). Furthermore, there exists a traditional split between geotechnical and structural engineers. The two disciplines are also separated in earthquake engineering. Therefore, it is often preferred consider SSI as simple as possible. On the one hand, a finite element model with SSI fully included is very time consuming and often at the limit of computational possibilities. Moreover, considering the required effort, it is generally not feasible to run a finite element analysis. On the other hand, simplified analysis methods are based on boundary conditions that are often not valid, e.g. fully rigid foundation slab. Therefore, it would be of significant added value to develop a semi-analytical modelling approach for SSI that deals with the shortcoming of both aforementioned conventional methods.

## 1.1. Objective

The objective of this thesis is to find a general approach in which: the SSI for shallow foundations can be modelled and the effects of SSI can be determined in a linear designed structural model. The model should give more insight in the SSI compared to the basic approaches described in codes and be faster than time consuming finite element (FE) analysis. To accomplish this, a semi-analytical approach is proposed, i.e. an analytical (mathematical) model using some numerical (computational) modelling techniques. The model has been developed to be coupled in a subsequent phase to a semi-analytical model of a tank superstructure, based on earlier work carried out by Canny (2018). This thesis focuses on the SSI part and investigates the effects of the flexibility of a shallow foundation on the (beneficial) radiation damping. Coupling of SSI and superstructure models has not yet been covered by the present thesis but is rather trivial. The model should allow for coupling with a liquid storage tank superstructure model at a later stage.

## 1.2. Research question

*Develop and implement a semi analytical analysis method to describe SSI for rigid and flexible shallow foundations on soil.*

## 1.3. Subquestions

- *What are the implications of the semi-analytical methodology for SSI and how does it compare to alternative methods?*
- *Can the obtained model performance be validated by means of comparison to other studies available in literature?*
- *How does flexibility of the foundation on a shallow foundation affect the SSI, compared with a rigid plate?*

## 1.4. Research approach

Both 2D plane-strain and 3D soil model of the soil are combined with a shallow foundation. The generic analysis model is build along the steps shown in figure 3.13. The model is based on fundamental physics in the frequency domain. The soil, structure and interaction parts are solved for independently. This is beneficial since the structural part can easily be replaced for another structure. The soil model is based on Green's functions, which describe the flexibility of the soil due to a local force. Since the model is linear, the Green's functions may be summed to construct a flexibility and stiffness matrix. The structure analysis in this thesis is limited to a modal analysis of a simple strip or circular plate foundation. However, the model is also suitable to be coupled to more complex structures or FE models. The stiffness matrix in this thesis is coupled to a foundation by matching modes of the foundation. In case of coupling to a FE model, the stiffness matrix of the soil are straightforwardly coupled to the FE model. In this situation, the equilibrium of interaction forces and displacements can be solved.

After the model is derived, it is validated with well-known studies of Gazetas (1983) and Richart et al. (1970). The influence of the relative flexibility of the foundation with respect to the soil is investigated, which can be considered a new achievement compared to the well-known literature that mainly focus on rigid plates. Although this thesis does not include the evaluation of a fully-coupled superstructure, the SSI model works for foundation slabs and can evaluate the kinematic effects.

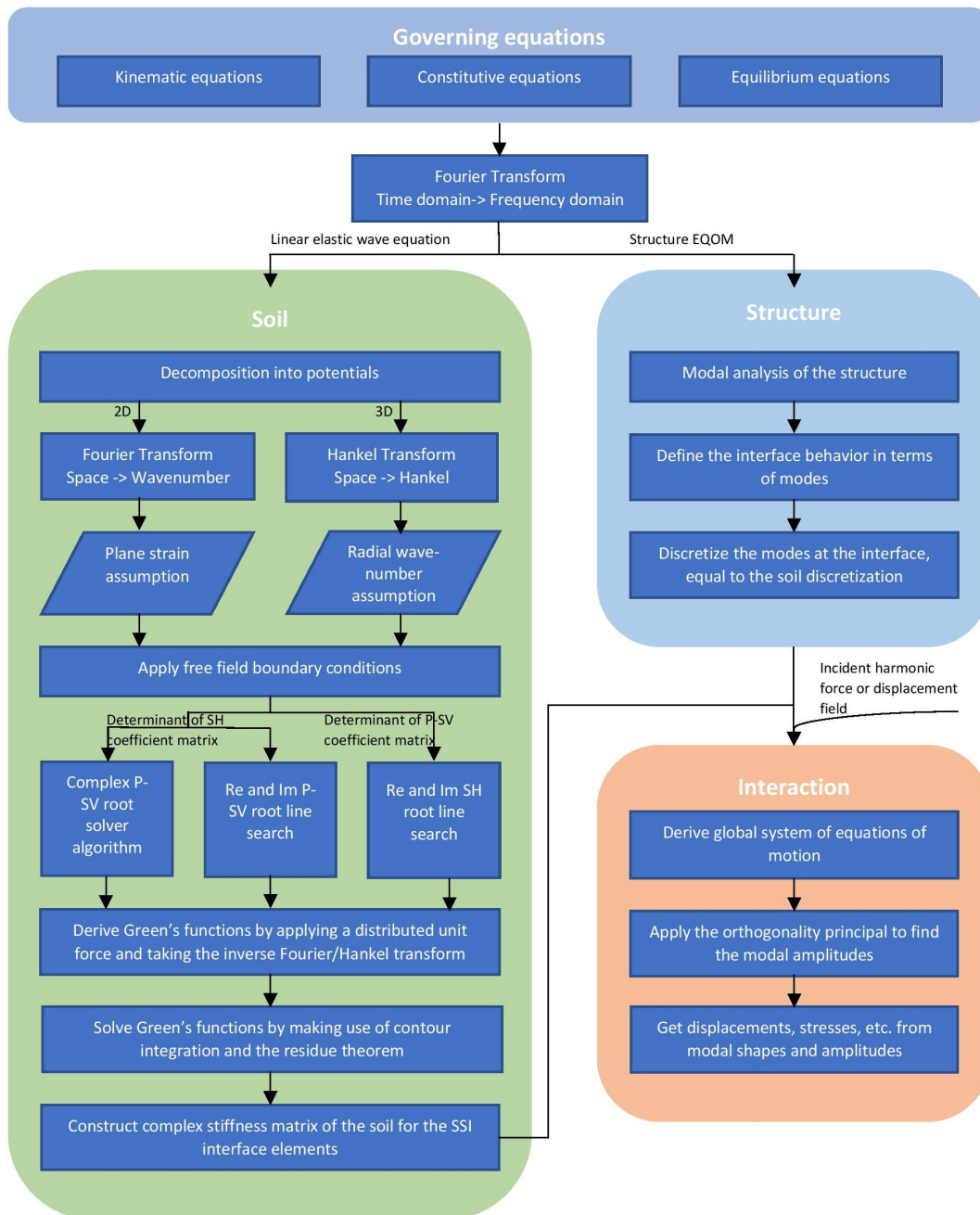


Figure 1.1: The approached steps to constructed the semi-analytical SSI model



# 2

## Literature

This chapter gives an introduction to the fundamental knowledge this thesis is based on. The principles of earthquakes, dynamics of structures, dynamics of a linear elastic medium and soil structure interaction are introduced.

### 2.1. Earthquakes

In earthquake engineering all around the world, various disciplines of engineering are combined to deal with the consequences of an earthquake. "Earthquakes are rare, low probability events with consequences that are large in terms of destruction. ... Earthquakes are a special category of hazards in that most human losses are due to failure of human-made structures - buildings, dams, lifelines, and so on. Therefore, in principle, with sufficient resources for research, development, education, followed by necessary investments in hazard reduction, earthquakes are a hazard that are within our power to respond to". (Press, 1985). The fact that earthquakes are hardly forecastable differs from many other hazards as for example hurricanes. People can be warned for hurricanes due to high level weather monitoring, but the only way for earthquake hazard reduction, is by smart engineering.

Earthquakes occur all around the world under distinctive circumstances, but earthquake engineering differs a lot due to differences in: types of earthquakes, frequency of occurrence, local regulation and wealth.

Since the aim of this thesis is to improve modelling of the structural response due to an earthquake, the fundamentals of earthquakes are briefly discussed.

#### 2.1.1. Cause of an earthquake

Earthquakes are classified by their cause. A distinction is made between two types of earthquakes; tectonic earthquakes and human induced earthquakes.

##### Tectonic earthquakes

Most natural earthquakes are caused by movement of the tectonic plates. The tectonic plates want to move relative to each other but since the boundaries of these plates are not smooth this movement is restricted and stress builds up. An earthquake occurs when the stress reaches a limit and suddenly releases. The release of stress is accompanied by displacements of the earth. The boundary interaction of tectonic plates is divided in three types shown in figure 2.1 of which also combinations are possible (Semper, 2017).

- **Divergent fault or extensional movement of plates:** At a divergent boundary, two plates move apart from each other. The tension weakens the plate crust until the rocks fracture and one block moves downwards compared to another. This results in shallow earthquakes with vertical movement. Furthermore, this phenomena create space between two plates resulting in rifts and volcanic activity, for example at the Mid-Atlantic Ridge.
- **Convergent fault or compressional movement of plates:** A convergent boundary is the opposite of a divergent boundary. Two plates are pushed to each other resulting in mountains, e.g. the Himalayas,

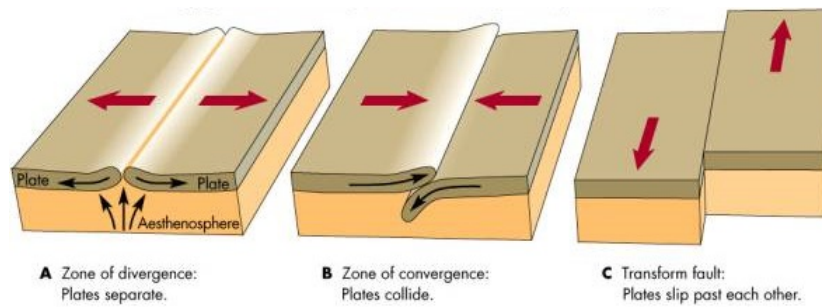


Figure 2.1: Tectonic plate motion: A) divergent fault line; B) convergent fault line; C) transform fault line (Source: J.D. Fix - Astronomy: Journey to the Cosmic Frontier)

are formed by collision between the Eurasian and Indian plate. Corresponding earthquakes vary in depth from just below the surface to many kilometres deep. The movement of the two plates relative to each other is vertical. When such earthquake takes place under the sea, the risk of a tsunami increases. The 2004 Sumatra earthquake is an example of such an earthquake causing a tsunami. Volcanic activity can be expected around the fault line and this type of earthquake results in the largest magnitudes measured.

- **Transform boundaries or sliding movement of plates:** Earthquakes occur due to tectonic plates sliding past each other, since the plates are not smooth and stress build up due to friction. When this stress is released, large horizontal displacements can be expected along the fault line like the San Andreas fault.

Tectonic earthquakes can also occur at local fault lines within a tectonic plate, also called intra-plate earthquakes. The magnitude of these intra-plate earthquakes is typically relatively small compared to earthquakes located at boundaries of tectonic plates (Semper, 2017).

### Human induced earthquakes

Natural processes such as migration of fluids, atmospheric pressure changes, sediment unloading and groundwater loss can load stress in the earth crust. These natural events can induce seismic activity, in most cases of unnoticeable scale. But since industry grows, more often earthquakes are linked to human causes. Mining- and dam-induced earthquakes are recognized for many decades. Since a couple of years the concern is growing about earthquakes induced by gas extraction, waste fluid injection and nuclear testing. Maximum global magnitudes are shown in figure 2.2 (Foulger et al., 2017).

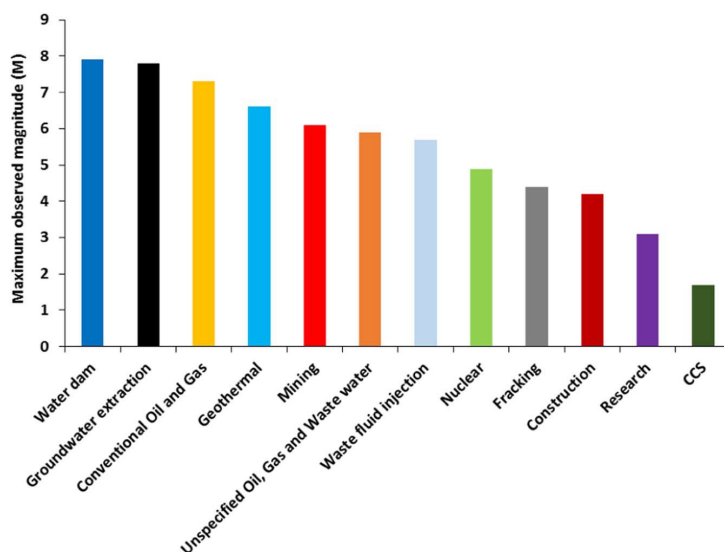


Figure 2.2: Maximum magnitude measured worldwide for human induced earthquakes with different causes (Source: Foulger et al. (2017))

The largest earthquake in The Netherlands is the 2012 Huizinge earthquake with a local magnitude ( $M_L$ ) of 3.6. In total 12 earthquakes occurred with a magnitude  $> 3.0$ , strongly related to the Groningen gas-field as shown in figure 2.3. The first seismic activity was recorded in 1991 when the reservoir reached about 28 % depletion, 28 years after the start of the gas extraction. Typical for the earthquakes in the Groningen area is that they are shallow (2.5 - 3.5 km), are short in duration but have a large peak ground acceleration (PGA) compared to the magnitude. However, the combination of frequencies, shallow depth and PGA can cause severe damage to construction and infrastructure at the surface.

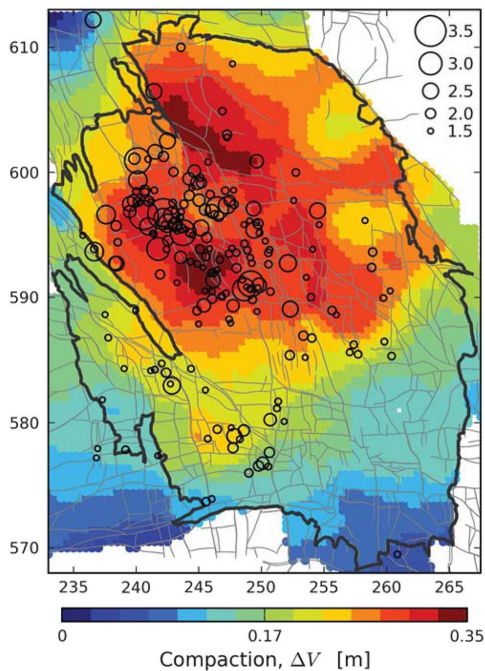


Figure 2.3: The Groningen gas-field with earthquake epicentres for events with a magnitude  $> 1.5$  in the period 1995-2012, shown on a model of reservoir compaction for 1960-2012. Thin gray lines show faults at the level of extraction. The black line closes around the gas-field. (Source: Foulger et al. (2017))

### 2.1.2. Wave types

With the sudden release of energy during an earthquake, waves are generated that carry energy away from the source to the surface. Waves travelling through the earth are called body waves. When a wave approaches a surface, other types of waves can be formed. These waves travel along the surface instead of through a body and are called surface waves. Depending on the frequency and wavelength, surface waves evanesce in depth relatively fast and are not noticeable any more at large depths.

There are two main types of body waves, a compressional wave and a shear wave. The compressional waves induce motion of the soil particles parallel to wave group direction. Therefore, compressional waves propagate by expansion and compression of the body they propagate through. This makes it possible for a compressional wave to travel through solids, liquids and gases, e.g. sound waves. The shear waves induce motion of the soil particles perpendicular to the direction of wave group propagation. It propagates by moving solid material. Therefore, this wave cannot exist in liquids or gases. The motion of both waves through a medium is shown in figure 2.5. The compressional wave propagates faster than the shear wave, which is why they are also called the primary wave (P-wave) and secondary wave (S-wave) respectively (Tomic, 2017). When a significantly large earthquake occurs, the body waves are measurable almost all around the world. Around 1930, Inge Lehmann declares why there are shadow zones for the P- and S-wave by making use of the properties of the P- and S-wave. She also found out by that fact, that the earth has a solid inner-core within the fluid outer-core shown in figure 2.4.

Surface waves can be formed at the surface of a solid, in case of earthquakes the surface is the Earth's crust.

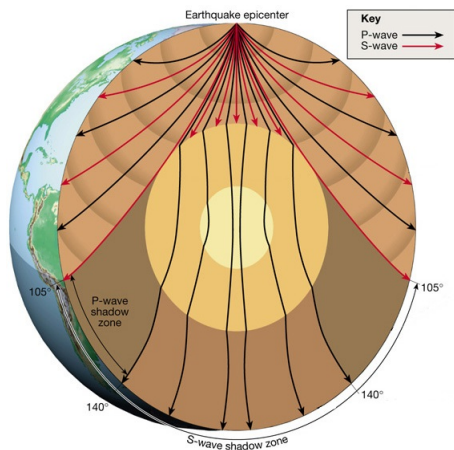


Figure 2.4: P- and S-wave propagation through the earth leading to the discovery of the earth core build up. (Source: Bakersfield college)

There are also two main types of surface waves: Rayleigh waves and Love waves. Rayleigh waves are characterized by particle motion both parallel (horizontal) and perpendicular (vertical) to the surface. The amplitude parallel to the surface is along the propagating direction. The wave propagates in an elliptic 'rolling' manner, comparable with ocean waves. If a section of the earth is made along the propagating direction of the wave, this wave will only have amplitudes in-plane. The amplitude of a Love wave is out-of-plane and based on shear deformation and has a side-to-side motion. The Love wave only has a amplitude parallel to the surface but perpendicular to its propagating direction. Surface waves are in contradiction to the body waves dispersive, meaning that they are not only material dependent but also frequency-dependent. Surface waves propagate slower than the body waves and the Love wave speed is smaller than the Rayleigh wave speed. Frequency influences the dissipative behaviour of surface waves in depth. The higher the frequency the faster the surface waves decay in depth. A visualisation of both surface waves is shown in figure 2.5.

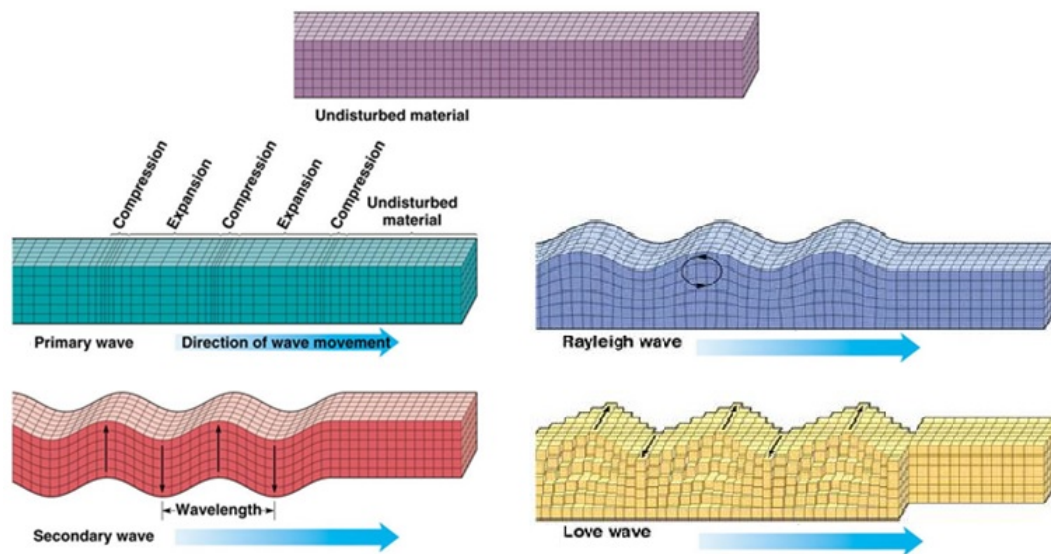


Figure 2.5: Wave types generated by an earthquake (Source: Tomic (2017))

## 2.2. Dynamic analysis

Structural analysis concerns the behaviour of structures. A structure can be loaded with many types of loads e.g. self-weight, wind, impact, snow and earthquakes. A distinction can be made between static loads and dynamics loads. Static loads are loads which (approachable) do not vary in time, self-weight is the most straightforward example of this <sup>1</sup>. Load cases that are called dynamic, vary (constantly) in time, such as wind, ocean waves or seismic loading. Therefore, time dependency is introduced in dynamic analysis, these analysis are in general more complex and time consuming than static analysis. Therefore, dynamic analysis are mainly performed when time dependency is of great important, such as in earthquake engineering. This chapter will introduce different dynamic analysis methods used in structural design, the frequency domain and fundamental knowledge of some simple linear dynamic systems.

### 2.2.1. Structural dynamic analysis methods

Different methods are used for seismic analysis of structures, from complex to rather simplified methods. The more simplified methods, used for less complex problems, have a larger uncertainty but are also respectively fast. Four often used methods (Normcommissie 351 001 "Technische Grondslagen voor Bouwconstructies", 2015) from simple to complex are:

- **Lateral force method:** In the lateral force method, dynamic forces are replaced with a static equivalents. The dynamic problem is simplified to a static problem, this is often done for wind loading.
- **Modal response method:** The modal response method is based on an eigenmode analysis of the undamped structural system, determining the eigenfrequencies and eigenmodes. These are determined by the mass and stiffness of a structure. The response of a structure is determined by the expected forces at the particular frequencies exciting the eigenmodes of the structure. The modal response method is often combined with a representation of the earthquake demand by a response spectrum.
- **Non-linear push-over method:** In this method a structure is incrementally laterally loaded into the range of a non-linear response. (Lateral modal) Forces are applied on a structure, they increase incrementally and the non-linear behaviour of the structure during loading is analysed.
- **Non-linear time history analysis:** Time history analysis analyses the dynamic response of a structure in time when subjected to a time dependent load. For example, measured earthquake records are applied on a structure. This method is the most complex method, but is the only method of the above which uses time dependent loading. Transient dynamics of structures and time dependent non linear response can be analysed.

### 2.2.2. Time and frequency domain

Any time signal can be constructed by a summation of harmonic frequencies functions with varying frequencies, amplitude and phase. The superposition of harmonic functions to construct a time domain function is done with Fourier series (Van Dalen, 2015).

$$f(t) = \frac{a_0}{2} \sum_{n=1}^{\infty} (a_n \cos(\omega_n t) + b_n \sin(\omega_n t)), \quad \omega_n = n \frac{\pi}{T} \quad (2.1)$$

In which  $\omega_n$  denotes an angular frequency of a harmonic function and

$$a_n = \frac{1}{T} \int_{-T}^T f(t) \cos(\omega_n t) dt, \quad b_n = \frac{1}{T} \int_{-T}^T f(t) \sin(\omega_n t) dt \quad (2.2)$$

Figure 2.6 gives an example of an, at first instance, random function constructed by a summation of only 4 harmonic functions. The Fourier series can be replaced by an integral over the time to translate a time dependent problem to a frequency dependent problem. This integral is called the Fourier integral. The Fourier integral may be applied forward and backward to translate a problem to the frequency domain and vice versa. Many problems are mathematically easier to solve in the frequency domain or a frequency domain can be

<sup>1</sup>Static loads are characterised by a rate of application of the load which is extremely slow compared to the fundamental eigenperiod of the structure.

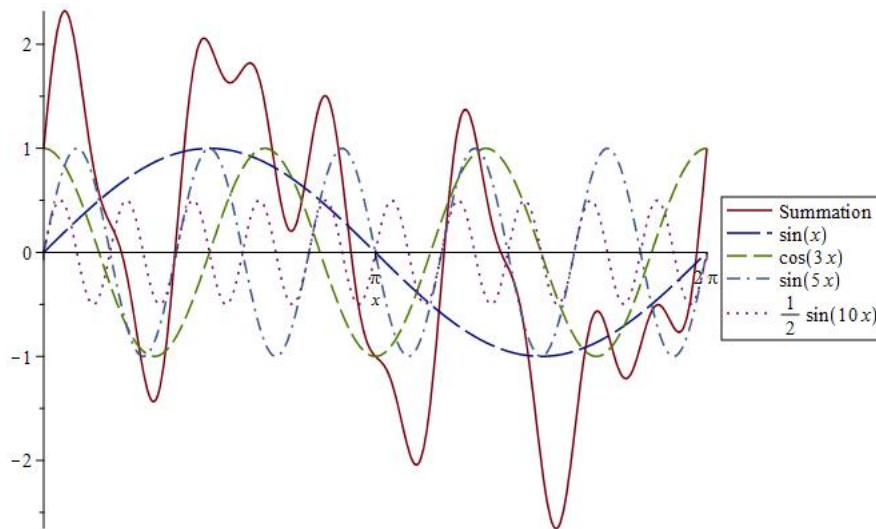


Figure 2.6: Summation of harmonic waves

created of multiple time records. During the translation from time to frequency and vice versa, the initial phases are lost.

$$\begin{aligned}
 f(t) &= \frac{1}{\sqrt{2\pi}} \int_{-\infty}^{\infty} F(\omega) e^{i\omega t} d\omega \\
 F(\omega) &= \frac{1}{\sqrt{2\pi}} \int_{-\infty}^{\infty} f(t) e^{-i\omega t} dt
 \end{aligned}
 \tag{2.3}$$

The Fourier integral can be used for the translation from the time to the frequency domain but similarly from the space to the wavenumber domain. This translation is also necessary to solve many linear dynamic problems, especially in continua. The Fourier transform may be used with different signs and premultiplications. The convention of the Fourier transforms used in this thesis is:

$$\begin{aligned}
 u(x, y, z, t) &= \left(\frac{1}{2\pi}\right)^4 \int_{-\infty}^{\infty} \int_{-\infty}^{\infty} \int_{-\infty}^{\infty} \int_{-\infty}^{\infty} \tilde{u}(k_x, k_y, k_z, \omega) e^{i(\omega t - k_x x - k_y y - k_z z)} dk_x dk_y dk_z d\omega \\
 \tilde{u}(k_x, k_y, k_z, \omega) &= \int_{-\infty}^{\infty} \int_{-\infty}^{\infty} \int_{-\infty}^{\infty} \int_{-\infty}^{\infty} u(x, y, z, t) e^{-i(\omega t - k_x x - k_y y - k_z z)} dx dy dz dt
 \end{aligned}
 \tag{2.4}$$

In which  $k_j$  are the wavenumbers in the directions  $x, y$  and  $z$ .

### 2.2.3. Damped mass-spring systems

The most simple dynamic system is the (damped) mass-spring system. This system contains only one degree of freedom and is called a single degree of freedom (SDOF) system, an example is shown in figure 2.7. The solution to this system contains the most fundamental knowledge of structural dynamics and is often used to understand the fundamental phenomena of dynamics. The model in figure 2.7 consists of a mass ( $m$ ) connected to a constrained spring ( $k$ ) and a damper/dashpot ( $c$ ) excited by a time dependent force ( $F(t)$ ). The displacement in  $x$  is denoted as  $u$ . To find the differential equation to solve this problem, three general equations need to be solved (Hölscher, 2016):

- **The equilibrium equations:** Are based Newton's equilibrium theory, which states that all acting forces present should be in equilibrium at any moment in time.
- **The constitutive equations:** Describe a relation between two physical quantities. Often related to material properties, such as stress strain relations. In linear elasticity we use Hooke's law.
- **The kinematic equations:** Describe the motion of points, bodies and systems without considering its mass or the force which is related to it. Kinematics describe the geometry of motion.

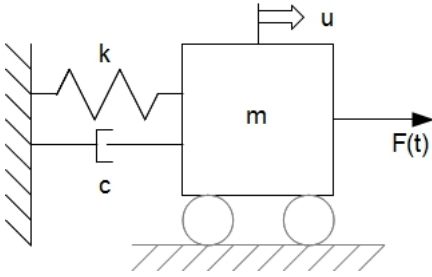


Figure 2.7: A single degree of freedom system

In case of the SDOF of figure 2.7, assuming a constant mass ( $m$ ), the equilibrium equations state that the sum of all forces acting on the mass are equal to a multiplication with its acceleration.

$$\sum F = m\ddot{u}(x) \quad (2.5)$$

in which a dot denotes the products time derivative such that  $\dot{x} = \frac{\partial x}{\partial t}$  denotes the first time derivative and  $\ddot{x} = \frac{\partial^2 x}{\partial t^2}$  denotes the second time derivative. The constitutive equations contain the force dependence of the spring and dashpot on respectively the change in displacement and velocity of the mass.

$$F_{spring} + F_{dashpot} = k\Delta u + c\Delta \dot{u} \quad (2.6)$$

The kinematic equations describe the change in motion.

$$\Delta \dot{u} = \dot{u} - \dot{u}_0, \quad \Delta u = u - u_0 \quad (2.7)$$

$u_0$  and  $\dot{u}_0$  are respectively the initial displacement and velocity. Assuming zero initial conditions the equation of motion (EQOM) of the system is described as:

$$m\ddot{u} + c\dot{u} + ku = F(t) \quad (2.8)$$

When a system consists of more degrees of freedom, the equation of motion is extended to matrix form, the size of the matrices and vectors equals the degrees of freedom. Figure 2.8 shows an example of a two degrees of freedom system with an acting force on the second mass. The corresponding equation of motion, Eq. (2.9), is similar to the one for a SDOF system and solvable in the same manner.

$$\begin{bmatrix} m_1 & 0 \\ 0 & m_2 \end{bmatrix} \begin{bmatrix} \ddot{u}_1 \\ \ddot{u}_2 \end{bmatrix} + \begin{bmatrix} c_1 + c_2 & -c_2 \\ -c_2 & c_2 \end{bmatrix} \begin{bmatrix} \dot{u}_1 \\ \dot{u}_2 \end{bmatrix} + \begin{bmatrix} k_1 + k_2 & -k_2 \\ -k_2 & k_2 \end{bmatrix} \begin{bmatrix} u_1 \\ u_2 \end{bmatrix} = \begin{bmatrix} 0 \\ F(t) \end{bmatrix}, \quad \mathbf{M}\ddot{\mathbf{u}} + \mathbf{C}\dot{\mathbf{u}} + \mathbf{K}\mathbf{u} = \mathbf{F} \quad (2.9)$$

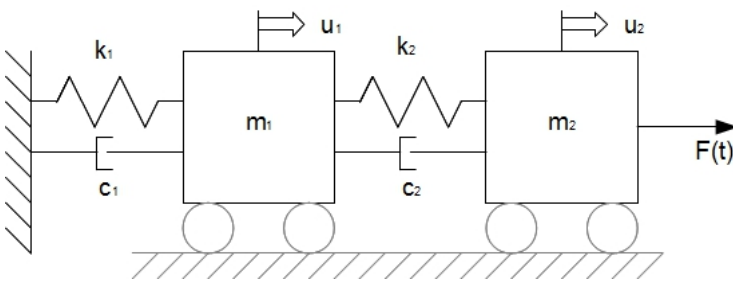


Figure 2.8: Two degrees of freedom system

The EQOM of the SDOF is solved for harmonic waves by substituting  $u = e^{-i\omega t}$  and assuming harmonic forcing with a frequency-dependent amplitude  $F_0$ . Eq. (2.8) can be rewritten as:

$$(\omega^2 m - i\omega c + k)u = F_0(\omega) \quad (2.10)$$

From the spring mass system without damping problem ( $c = 0$ ) the natural frequency can be found from the homogeneous situation.

$$\omega_n^2 = \frac{k}{m} \quad (2.11)$$

In a MDOF system, the number ( $n$ ) of natural frequencies is equal to the number of degrees of freedom. The natural frequencies of a structure is the frequency in which the structure tends to oscillate without damping, the structure is not stable. Therefore, the natural frequency of a structure is important since excitation of a structure in a frequency close by its natural frequency amplifies the response with respect to other frequencies. The solution to the problem of Eq. (2.10) in the frequency domain is:

$$u(\omega) = \frac{\frac{F_0(\omega)}{k}}{1 + 2i\zeta \frac{\omega}{\omega_n} - \frac{\omega^2}{\omega_n^2}}, \quad 2\zeta = \frac{c}{m\omega_n} = \frac{c}{\sqrt{km}} \quad (2.12)$$

From Eq. (2.12) it can be derived that, if the exciting frequency  $\omega$  approaches the natural frequency  $\omega_n$ , the displacement of the system goes to infinity (when there is only little or no damping in the system).

#### 2.2.4. Continuum systems

In the previous section, only discrete masses with discrete springs and dash-pots with no internal forces are considered. Contrary to that, there are also many examples of systems which can be represented better as a continuum system instead of a discrete system. The most simple example is a one dimensional rod, but also a beam or a plate is an example of a continuum system. This section will evaluate continuum systems based on the dynamic beam equations of a pure bending or Euler Bernoulli beam. The distributed mass and internal stiffness of a continuum system can respectively be seen as an infinite number of small masses and internal springs. The internal stiffness of a continuum system wants to force the system back to its original shape ones deformed, this component is included in the EQOM.

From the equilibrium, constitutive and kinematic equations of a beam, similar to a SDOF, the EQOM of a beam is formed:

$$EI \frac{\partial^4 u_z}{\partial z^4}(x) + \rho A \ddot{u}_z(x, t) = q(x, t) \quad (2.13)$$

Where  $E, I, \rho, A, u_z$  and  $q$  are respectively the Young's modulus, second moment of area, material density, cross-sectional area, displacement and external distributed force. A continuum system has an infinite amount of eigenfrequencies with corresponding eigenmodes. A summation of the eigenmodes can represent most of the deformations of a continuum system. The general solution to the free vibration (no external forcing) of a Euler Bernoulli beam, assuming harmonic motions, leads to the eigenfrequencies and corresponding modal shapes. The general solution can be written in different ways, but to solve for the wavenumbers ( $k_x$ ), the following representation is used instead of an exponential representation:

$$u_z(x) = A1 \cos(k_x x) + A2 \sin(k_x x) + A3 \cosh(k_x x) + A4 \sinh(k_x x) \quad (2.14)$$

In which:

$$k_x = \sqrt{\omega}^4 \sqrt{\frac{\rho A}{EI}}, \quad \omega_n = k_n^2 \sqrt{\frac{EI}{\rho A}} \quad (2.15)$$

The four unknown coefficients in the general equation can be expressed in each other by applying three of the four the boundary conditions, so one unknown remains. All boundary conditions must be satisfied for every value of the last unknown, the conditions can be satisfied by particular wavenumbers  $k_n$  which can be determined from the boundary conditions with respect to  $k_x$ . For a free-edge beam with length  $L$ , the natural wavenumbers to solve the system for are derived from the equation (Gonçalves et al., 2007).

$$\cos(k_n L) \cosh(k_n L) = 1 \quad (2.16)$$

Substitute Eq. (2.16) in the general solution results in Eq. (2.15) with  $n$  modal shapes with  $n$  unknowns. The displacement is expressed in a summation over all modal shapes  $\phi$ , which results in

$$u_z(x) = \sum_{n=1}^{\infty} A_n \phi_n(k_n) \quad (2.17)$$

The sum of the modal shapes can be solved for the prescribed boundary conditions and any particular external harmonic load.

## 2.3. Dynamic soil structure interaction models

SSI models vary from discrete approaches to continuum approach. The discrete approaches assume a rigid base below a super structure and represent the soil with a single spring per degree of freedom. The continuum approach describes the behaviour of the soil from the kinematic, constitutive and equilibrium equations (Caselunghe and Eriksson, 2012). Both methods have advantages and disadvantages. A discrete model is easy to implement, but based on assumptions and simplifications. A discrete model is often not able to describe the kinematic interaction<sup>2</sup>, but only considers the inertial interaction<sup>3</sup>. Continuum models can include both effects but are often described with time consuming FEM software. An intermediate method would be the (semi-) analytic approach. FE models are able to give detailed insight in SSI but due to their time consuming characteristic, FE models are not further considered.

### 2.3.1. Simplified spring model

A system commonly used for simplified analysis consists of a single degree of freedom representation of the structure and a flexible foundation described with (frequency-dependent) complex translational and rotational springs  $\bar{k}_u$  and  $\bar{k}_\theta$  shown in figure 2.9. The model can be used for e.g. single story structures that can be represented by a SDOF, or multi story structures that are dominated by the fundamental mode response. The model can only describe the inertial interaction. Therefore, the model neglects kinematic interaction. The frequency-dependent complex springstiffness can be described by an impedance function expressed in the form (Stewart et al., 1999):

$$\bar{k}_j = k_j(a_0, \nu) + i\omega c_j(a_0, \nu) \quad (2.18)$$

Where  $a_0$  denotes a dimensionless frequency,  $\nu$  the soil Poisson's ratio,  $k_j$  the frequency-dependent stiffness and  $c_j$  the frequency-dependent damping. The stiffness and damping parameters can be found in literature by Kausel (1974), e.g. under assumption of a rigid foundation over a homogeneous layer or half space. Modifications for soil layering or a bedrock at a certain depth are available as well.

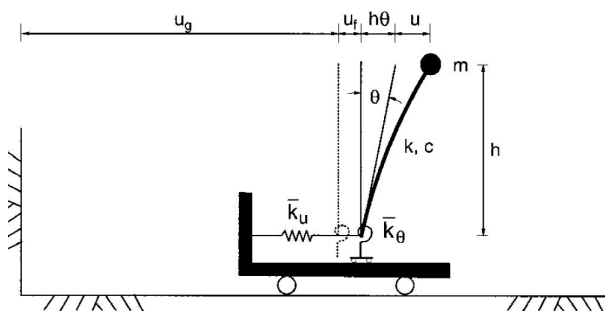


Figure 2.9: Simplified model for analysis of the inertial SSI of a SDOF structure (Source: Stewart et al. (1999))

### 2.3.2. Winkler model

An old but frequently used well-known SSI model is the Winkler model. The Winkler model is based on a foundation on linear elastic independent vertical springs. The two major shortcomings of the Winkler model are that: the springs act independent and the (complex) spring parameters need to be assumed. In case of a Winkler model with a uniform stiffness along the foundation, the stress and deformation profiles will not match reality as shown in figure 2.10. The foundation stiffness at the structures edges will be underestimated. A solution to this problem is to add additional spring stiffness at the edge of the structure. However, the additional stiffness is hard to estimate. In consequence of the independent response of the vertical springs, mathematically the stiffness matrix describing the stiffness of the Winkler springs will be diagonal (Caselunghe and Eriksson, 2012).

Possible additions to improve the Winkler models behaviour and to overcome the independence of the springs

<sup>2</sup>The presence of a (stiff) foundation interacting with the soil cause foundation motion that deviate with the free-field motion of the soil. The kinematic interaction relates motion of a (massless) foundation to the free-field motion (Stewart et al., 1999).

<sup>3</sup>Inertia developed in the structure due to its vibration results in interaction forces and moments on the soil, which in turn cause displacements of the foundation relative to the free-field (Stewart et al., 1999).

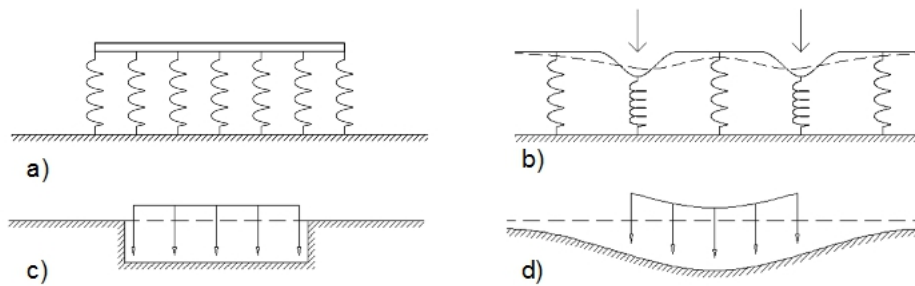


Figure 2.10: a) Schematization of a Winkler spring model; b) Deformation of a Winkler spring model compared with continuum (dashed); c) Deformation of the soil by a Winkler model; d) Real deformation of the soil (Source: Caselunghe and Eriksson (2012))

can be carried out by e.g. couple a interaction element to redistribute forces, split the springs in two layers or add additional elements which can transfer shear force only, as shown in figure 2.11. Although these ad-

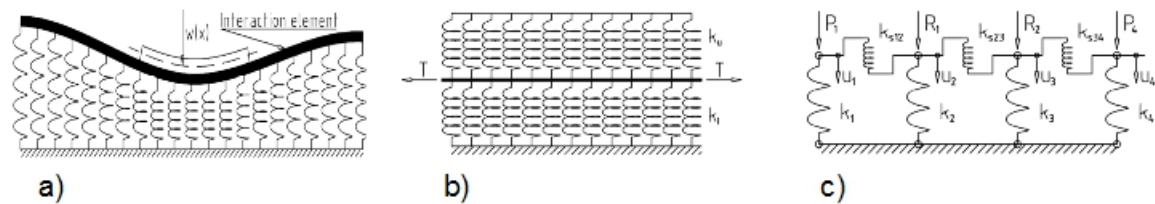


Figure 2.11: a) Winkler springs including an interaction element; b) Hybrid model with two layers of Winkler springs with a pre-tensioned layer inbetween; c) Additional shearforce elements inbetween the Winkler springs (Source: Caselunghe and Eriksson (2012))

ditions improve the Winkler model, they also introduce additional variables which are more difficult to be approximated and introduce uncertainties. When a Winkler model interacts with a rigid foundation, it has almost no benefits compared to the SDOF system aforementioned. Furthermore, a Winkler model is not able to distribute forces, which results in unrealistic stress and deformation patterns.

### 2.3.3. Linear elastic model

The representation of the soil as continuum is often done with a FEM, but there are also analytical ways to determine the soil behaviour, restricted to a linear elastic approach. The general equations for a linear elastic material underlie the method. The behaviour of the soil can be expressed in stresses and deformations of a soil deposit under the influence of a load applied on the surface. An approximation is often made in a analytical approach is an elastic half-space (Verruijt, 2010). The half-space approximation includes a homogeneous linear elastic continuum with a stress-free surface. The soil can also be represented in other configurations than a half-space as a homogeneous linear elastic medium. The conditions describing the medium are in terms of stresses, strains and displacements in a linear elastic continuum. These relations are called the conditions of equilibrium, the constitutive relations and the compatibility conditions, respectively the conditions can be described in both a Cartesian coordinate system  $(x, y, z)$ , with corresponding displacements  $(u_x, u_y, u_z)$  and in cylindrical coordinate system  $(r, \theta, z)$ , with corresponding displacements  $(u_r, u_\theta, u_z)$ . Both Einstein's summation convention (i.e. summation over repeated indices) and the tensor form are used in this section.

#### Cartesian coordinate system

The strain-displacement relation from basic linear elasticity theory covers both the normal strain  $(\epsilon_{i=j})$  and the shear strain  $(\epsilon_{i \neq j})$  relations for a Cartesian coordinate system.

$$\epsilon_{ij} = \frac{1}{2}(u_{j,i} + u_{i,j}) \quad (2.19)$$

Symmetry implies that  $\epsilon_{ij} = \epsilon_{ji}$ . The volume strain is defined as the sum of the normal strains in the three principle directions:

$$\epsilon = \epsilon_{xx} + \epsilon_{yy} + \epsilon_{zz} \quad (2.20)$$

The constitutive equations (i.e. the stress-strain displacements) follow from the generalized form of the Hooke's law. The stress equations are described as:

$$\sigma_{ij} = \lambda \epsilon_{kk} \delta_{ij} + 2\mu \epsilon_{ij} \quad (2.21)$$

In which  $\delta_{ij}$  is the Kronecker delta function ( $\delta_{ij} = 1$  if  $i = j$  and  $\delta_{ij} = 0$  if  $i \neq j$ ). Since  $\epsilon_{ij} = \epsilon_{ji}$ , it also holds that  $\sigma_{ij} = \sigma_{ji}$ .  $\lambda$  and  $\mu$  are Lamé constants and can be expressed in terms of the Young's modulus  $E$  and the Poisson's ratio  $\nu$ :

$$\lambda = \frac{\nu E}{(1 + \nu)(1 - 2\nu)} \quad (2.22)$$

$$\mu = \frac{E}{2(1 + \nu)}$$

$\mu$  is also called the shear modulus. In the absence of any external dynamic forces, the free-vibration equations of motion read:

$$\sigma_{ji,j} + b_i = \rho \ddot{u}_i \quad (2.23)$$

Wherein  $\rho$  is a mass density constant ( $kg/m^3$ ) and  $b_i$  are body forces.

### Cylindrical coordinate system

In a cylindrical coordinate system the same relations exist as for the Cartesian coordinate system. The constitutive relations are identical, only the indices (x,y,z) are replaced with (r,θ,z). A radial factor is included in the strain-displacement equations leading to:

$$\begin{aligned} \epsilon_{rr} &= u_{r,r}, & \epsilon_{r\theta} &= \frac{1}{2} \left( \frac{1}{r} u_{r,\theta} + u_{\theta,r} - \frac{u_\theta}{r} \right) \\ \epsilon_{\theta\theta} &= \frac{1}{r} (u_{\theta,\theta} + u_r), & \epsilon_{\theta z} &= \frac{1}{2} \left( u_{\theta,z} + \frac{1}{r} u_{z,\theta} \right) \\ \epsilon_{zz} &= u_{z,z}, & \epsilon_{zr} &= \frac{1}{2} (u_{r,z} + u_{z,r}) \end{aligned} \quad (2.24)$$

The equations of motion in cylindrical coordinates read:

$$\begin{aligned} \sigma_{rr,r} + \frac{1}{r} \sigma_{r\theta,\theta} + \sigma_{rz,z} + \frac{1}{r} (\sigma_{rr} - \sigma_{\theta\theta}) + b_r &= \rho \ddot{u}_r \\ \sigma_{r\theta,r} + \frac{1}{r} \sigma_{\theta\theta,\theta} + \sigma_{\theta z,z} + \frac{2}{r} \sigma_{\theta r} + b_\theta &= \rho \ddot{u}_\theta \\ \sigma_{rz,r} + \frac{1}{r} \sigma_{r\theta,z} + \sigma_{zz,z} + \frac{1}{r} \sigma_{rz} + b_z &= \rho \ddot{u}_z \end{aligned} \quad (2.25)$$

### 2.3.4. The wave equation

The equation of motion can be expressed in terms of displacements by substituting the constitutive equations and strain-displacement equation in the equation of motion. This equation is called the Cauchy-Navier equation or wave equation and holds for both Cartesian and cylindrical coordinate systems. The wave equation is one of the basic equations of elastodynamics.

$$(\lambda + \mu) \nabla(\nabla \cdot \mathbf{u}) + \mu \nabla^2 \mathbf{u} + \mathbf{b} = \rho \ddot{\mathbf{u}} \quad (2.26)$$

The bold symbols refer to vectors, the Laplace operator  $\nabla^2$  is equal to the divergence of the gradient ( $\nabla \cdot \nabla$ ). The Laplace operator may be rewritten in two terms describing dilatation and rotation. This is a practical substitution, used to distinguish the two different types of waves within the wave equation.

$$\nabla^2 \mathbf{u} = \nabla(\nabla \cdot \mathbf{u}) - \nabla \times \nabla \times \mathbf{u} \quad (2.27)$$

Wherein  $\nabla$ ,  $\nabla \cdot$  and  $\nabla \times$  denote respectively the divergence, gradient and curl. By substituting Eq. (2.27) in Eq. (2.26), the wave equation can be written as:

$$\rho \ddot{\mathbf{u}} = (\lambda + 2\mu) \nabla(\nabla \cdot \mathbf{u}) - \mu (\nabla \times \nabla \times \mathbf{u}) \quad (2.28)$$

The two different waves types that can propagate within a body are the compression wave and the shear wave. The compression wave, also called the longitudinal wave or P-wave induce motion of the soil particles parallel to the direction of the group velocity, the shear wave, also called the transverse or S-wave induce motion of the soil particles perpendicular to the direction of the group velocity. Both waves propagate with different group velocities, of which the P-wave has the highest group velocity. The group velocity squared can be found from the Navier equations by dividing the wave equation by the mass density  $\rho$  and expanding the Laplace operator  $\nabla^2$ . The wave equation is rewritten as:

$$\ddot{\mathbf{u}} = c_p^2 \nabla(\nabla \cdot \mathbf{u}) - c_s^2 (\nabla \times \nabla \times \mathbf{u}) \quad (2.29)$$

In which the P- and S-wave group velocity are described respectively by:

$$\begin{aligned} c_p &= \sqrt{\frac{\lambda + 2\mu}{\rho}} \\ c_s &= \sqrt{\frac{\mu}{\rho}} \end{aligned} \quad (2.30)$$

# 3

## 2D plane-strain soil model

This chapter considers the derivation of a dynamically loaded 2D plane-strain model of the soil. Further expansion of the model including the SSI will be based on the 2D plane-strain modelling technique. A model is called plane-strain if the out-of-plane principle strain is set to zero (i.e.  $u_{i,y} = 0$ , a constant deformation in the out-of-plane direction). By assuming a plane-strain model, the wave equation is decoupled into potentials for the coupled in-plane PSV-wave, i.e. the compressional wave and vertically polarized shear wave, and the decoupled anti-plane SH-wave, i.e. the horizontally polarized shear wave. This decoupling is derived later on in this chapter. The 2D plane-strain model can be expanded to a 3D cylindrical model which uses the same decoupling of in-plane and anti-plane waves.

The soil problem in this thesis is linearly approached, and therefore the soil behavior is assumed linear elastic, isotropic and homogeneous. For the soil structure interaction of structures with a shallow foundation, the soil behavior at the surface is most interesting. Therefore, a continuous model in horizontal and vertical direction with only a boundary at the surface could be suggested. A disadvantage of this model is that due to an infinite depth, numerical singularities in for infinite displacements occur since the bottom boundary is only described by its non-reflective behavior. Therefore, in the present thesis, a single layered model is chosen, which includes a bedrock (rigid) boundary at a certain depth.

The starting point for combining soil and superstructure are Green's equations. These equations describe the pulse response reaction at a certain distance from the pulse. So Green's principle describes a force-displacement relation for every possible location. In this thesis the force is chosen to be a stress over a certain width instead of a point load. The advantage of a stress over a width is that it overcomes the singularity which exists right below a point load. A schematization of the model is shown in figure 3.1. The solution of the

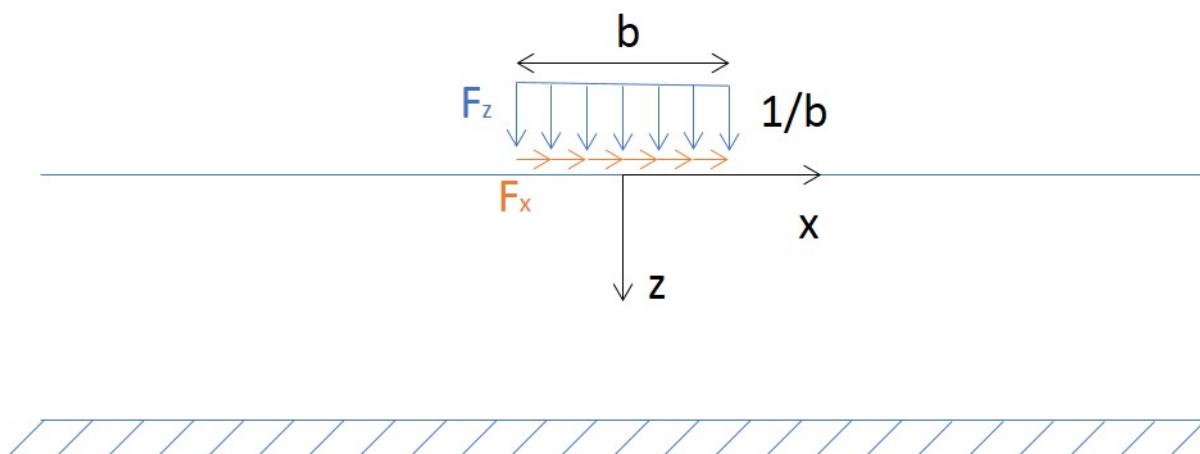


Figure 3.1: schematization of the 2D soil model.

force-displacement relation is found in the frequency-wavenumber domain and is transferred back to the frequency-space domain. This is done by decomposition of the potentials and a (inverse) Fourier transform for the wave equation. The soil properties used in this chapter are defined in table 3.1.

Characteristic	Symbol	Value	Unit
Young's modulus	$E$	$7 * 10^7$	$N / m^2$
Density	$\rho$	1700	$kg / m^3$
Poisson's ratio	$\nu$	0.4	-
Shear modulus	$\mu$	$2.5 * 10^7$	$N / m^2$
Lame parameter	$\lambda$	$1 * 10^8$	$N / m^2$

Table 3.1: Soil parameters

### 3.1. The decomposition of the wave equation by its potentials

A method to solve the wave equation by separation of potentials is the Helmholtz decomposition. This technique is used to solve the wave equation by separation of variables. The equation is rewritten such that there is a component describing the volumetric strain and a component describing the rotational vector. The P-wave propagates by a change in volumetric strain, and the S-wave propagates by shear deformation perpendicular to the propagating direction, so the S-wave is based on rotations. This will follow from the separation of variables. The starting point will be the wave equation from Eq. (2.29):

$$\ddot{\mathbf{u}} = c_p^2 \nabla(\nabla \cdot \mathbf{u}) - c_s^2 (\nabla \times \nabla \times \mathbf{u}) \quad (3.1)$$

The volumetric strain (scalar) and the rotation vector are respectively defined by:

$$\varepsilon = \nabla \cdot \mathbf{u}, \quad \boldsymbol{\Omega} = \frac{1}{2} \nabla \times \mathbf{u} \quad (3.2)$$

Substituting Eq. (3.2) in Eq. (3.1) the wave equations is written as:

$$\ddot{\mathbf{u}} = c_p^2 \nabla \varepsilon - 2c_s^2 (\nabla \times \boldsymbol{\Omega}) \quad (3.3)$$

To separate Eq. (3.3) into two equations describing the motions of the P- or S-waves, either the divergence or the curl of both sides of Eq. (3.3) is taken. Taking first the divergence leads to separation of the volumetric strain component.

$$\nabla \cdot \ddot{\mathbf{u}} = \ddot{\varepsilon} = c_p^2 \nabla \cdot \nabla \varepsilon - 2c_s^2 \nabla \cdot (\nabla \times \boldsymbol{\Omega}) \quad (3.4)$$

The volumetric component is separated by making use of the fact that the rotational vector is zero in every case. Since the volumetric strain is a scalar, the volumetric strain may be replaced by the Helmholtz scalar potential.

$$\begin{aligned} \nabla \cdot (\nabla \times \boldsymbol{\Omega}) &= 0, & \ddot{\varepsilon} &= c_p^2 \nabla^2 \varepsilon, \\ \varepsilon &\equiv \phi, & \ddot{\phi} &= c_p^2 \nabla^2 \phi \end{aligned} \quad (3.5)$$

The rotational vector is separated by the taking the curl of both sides of the wave equation, Eq. (3.1).

$$\nabla \times \ddot{\mathbf{u}} = 2\ddot{\boldsymbol{\Omega}} = c_p^2 \nabla \times \nabla \varepsilon - 2c_s^2 \nabla \times (\nabla \times \boldsymbol{\Omega}) \quad (3.6)$$

The rotational vector is separated by making use of the fact that the volumetric strain is zero in every case. Furthermore, the rotational vector may be replaced by the Helmholtz vector potential.

$$\begin{aligned} \nabla \times (\nabla \varepsilon) &= 0, & \ddot{\boldsymbol{\Omega}} &= c_s^2 \nabla^2 \boldsymbol{\Omega}, \\ 2\boldsymbol{\Omega} &\equiv \boldsymbol{\psi}, & \ddot{\boldsymbol{\psi}} &= c_s^2 \nabla^2 \boldsymbol{\psi} \end{aligned} \quad (3.7)$$

The Helmholtz decomposition holds that any vector field can be represented by a combination of the gradient of some scalar potential and the curl of a vector. These potentials are called the "Helmholtz potentials" (MIT OpenCourseWare, 2008). Assuming harmonic waves ( $\ddot{\phi} = -\omega^2 \phi$ ) the Helmholtz potentials may be written as.

$$\begin{aligned} \nabla^2 \phi + \frac{\omega^2}{c_p^2} \phi &= \nabla^2 \phi + k_p^2 \phi = 0 \\ \nabla^2 \boldsymbol{\psi} + \frac{\omega^2}{c_s^2} \boldsymbol{\psi} &= \nabla^2 \boldsymbol{\psi} + k_s^2 \boldsymbol{\psi} = 0 \end{aligned} \quad (3.8)$$

The conditions of Eq. (3.5) and Eq. (3.7) hold for the Helmholtz potentials:

$$\nabla \times (\nabla \phi) = 0, \quad \nabla \cdot (\nabla \times \boldsymbol{\psi}) = 0 \quad (3.9)$$

From which it follows that the vector  $\boldsymbol{\psi}$  has only two independent components as shown in Eq. (3.10).

$$\frac{\partial \psi_y}{\partial y} = - \left( \frac{\partial \psi_x}{\partial x} + \frac{\partial \psi_z}{\partial z} \right) \quad (3.10)$$

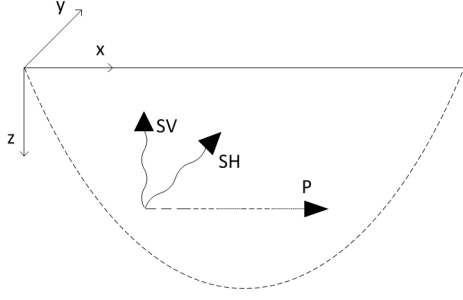


Figure 3.2: Compressional (P) wave, vertically polarized shear wave (SV) and horizontally polarized shear wave (SH)

Figure 3.2 shows the coupled in-plane compressional P-wave, the vertically polarized in-plane shear SV-wave and the horizontally polarized out-of-plane SH-wave. The general solution in 3D for the Helmholtz potentials in Eq. (3.8) is:

$$\begin{aligned}\tilde{\phi}(x, y, z, \omega) &= (a_1 e^{ik_x x} + a_2 e^{-ik_x x})(a_3 e^{ik_y y} + a_4 e^{-ik_y y})(a_5 e^{ik_z z} + a_6 e^{-ik_z z}), & k_x^2 + k_y^2 + k_z^2 &= k_p^2 \\ \tilde{\psi}(x, y, z, \omega) &= (\mathbf{b}_1 e^{ik_x x} + \mathbf{b}_2 e^{-ik_x x})(\mathbf{b}_3 e^{ik_y y} + \mathbf{b}_4 e^{-ik_y y})(\mathbf{b}_5 e^{ik_z z} + \mathbf{b}_6 e^{-ik_z z}), & k_x^2 + k_y^2 + k_z^2 &= k_s^2\end{aligned}\quad (3.11)$$

The tilde-sign refers to the frequency domain. Eq. (3.8) can also be found by substituting  $\mathbf{u} = \nabla\phi + \nabla \times \psi$  in Eq. (3.1). Through this substitution, the displacements in 3D, expressed in the Helmholtz potentials are:

$$\begin{aligned}\tilde{u}_x &= \frac{\partial \tilde{\phi}}{\partial x} + \left( \frac{\partial \tilde{\psi}_z}{\partial y} - \frac{\partial \tilde{\psi}_y}{\partial z} \right) \\ \tilde{u}_y &= \frac{\partial \tilde{\phi}}{\partial y} - \left( \frac{\partial \tilde{\psi}_z}{\partial x} - \frac{\partial \tilde{\psi}_x}{\partial z} \right) \\ \tilde{u}_z &= \frac{\partial \tilde{\phi}}{\partial z} + \left( \frac{\partial \tilde{\psi}_y}{\partial x} - \frac{\partial \tilde{\psi}_x}{\partial y} \right)\end{aligned}\quad (3.12)$$

### 3.2. The stress and displacement field

A 2D plane-strain situation is considered, i.e.  $\frac{\partial}{\partial y} = 0$ . Therefore, Eq. (3.12), describing the displacements, reduces to:

$$\begin{aligned}\tilde{u}_x &= \frac{\partial \tilde{\phi}}{\partial x} - \frac{\partial \tilde{\psi}_y}{\partial z} = \frac{\partial \tilde{\phi}}{\partial x} - \frac{\partial \tilde{\psi}}{\partial z} \\ \tilde{u}_y &= \frac{\partial \tilde{\psi}_x}{\partial z} - \frac{\partial \tilde{\psi}_z}{\partial x} = \frac{\partial \tilde{\chi}}{\partial z} - \frac{\partial \tilde{\chi}}{\partial x} \\ \tilde{u}_z &= \frac{\partial \tilde{\phi}}{\partial z} + \frac{\partial \tilde{\psi}_y}{\partial x} = \frac{\partial \tilde{\phi}}{\partial z} + \frac{\partial \tilde{\psi}}{\partial x}\end{aligned}\quad (3.13)$$

Where  $\psi$  is the Helmholtz potential to the vertical polarized SV-wave and  $\chi$  Helmholtz potential to the horizontal polarized SH-wave. The latter is decoupled from the P-wave as shown from Eq. (3.13). The expressions for the Helmholtz potentials from Eq. (3.11) also reduce due to the plane-strain assumption. Since wavenumber of the propagating waves in 2D is found by Pythagoras rule as shown in figure 3.3. A wave is evanescent in a direction when a wavenumber is imaginary or complex, although this does not affect the phase of the wave (Van Dalen, 2015).

$$\begin{aligned}\tilde{\phi}(x, z, \omega) &= (a_1 e^{ik_{z,p}z} + a_2 e^{-ik_{z,p}z}) e^{-ik_x x}, & k_{z,p} &= \sqrt{k_p^2 - k_x^2} \\ \tilde{\psi}(x, z, \omega) &= (b_1 e^{ik_{z,s}z} + b_2 e^{-ik_{z,s}z}) e^{-ik_x x}, & k_{z,s} &= \sqrt{k_s^2 - k_x^2} \\ \tilde{\chi}(x, z, \omega) &= (c_1 e^{ik_{z,s}z} + c_2 e^{-ik_{z,s}z}) e^{-ik_x x}, & k_{z,s} &= \sqrt{k_s^2 - k_x^2}\end{aligned}\quad (3.14)$$

The stresses are found by the stress-strain relations from Eq. (2.21). After substitution, Eq. (3.13) results in:

$$\begin{aligned}\tilde{\sigma}_{xz} &= \mu \left( \frac{\partial \tilde{u}_z}{\partial x} + \frac{\partial \tilde{u}_x}{\partial z} \right) = \mu \left( 2 \frac{\partial^2 \tilde{\phi}}{\partial x \partial z} + \frac{\partial^2 \tilde{\psi}}{\partial x^2} - \frac{\partial^2 \tilde{\psi}}{\partial z^2} \right) \\ \tilde{\sigma}_{yz} &= \mu \frac{\partial \tilde{u}_y}{\partial z} = \mu \left( \frac{\partial^2 \tilde{\chi}}{\partial z^2} - \frac{\partial^2 \tilde{\chi}}{\partial x \partial z} \right) \\ \tilde{\sigma}_{zz} &= \lambda \left( \frac{\partial \tilde{u}_x}{\partial x} + \frac{\partial \tilde{u}_z}{\partial z} \right) + 2\mu \frac{\partial \tilde{u}_z}{\partial z} = \lambda \left( \frac{\partial^2 \tilde{\phi}}{\partial x^2} + \frac{\partial^2 \tilde{\phi}}{\partial z^2} \right) + 2\mu \left( \frac{\partial^2 \tilde{\psi}}{\partial z^2} + \frac{\partial^2 \tilde{\psi}}{\partial x \partial z} \right)\end{aligned}\quad (3.15)$$

Substituting Eq. (3.14) in Eq. (3.13), yields the expressions for the displacements. A modification is done by shifting the  $z$  axis with the height of the layer for the reason that these exponents do not approach infinity for large  $z$ . The anti-plane SH- wave describes only a shear displacement in the anti-plane direction, and therefore the SH-wave is decoupled from the in-plane PSV- wave describing a coupled P- and SV- wave in-plane. Therefore, there are four unknowns, which need to be solved for the PSV-wave and two for the SH-

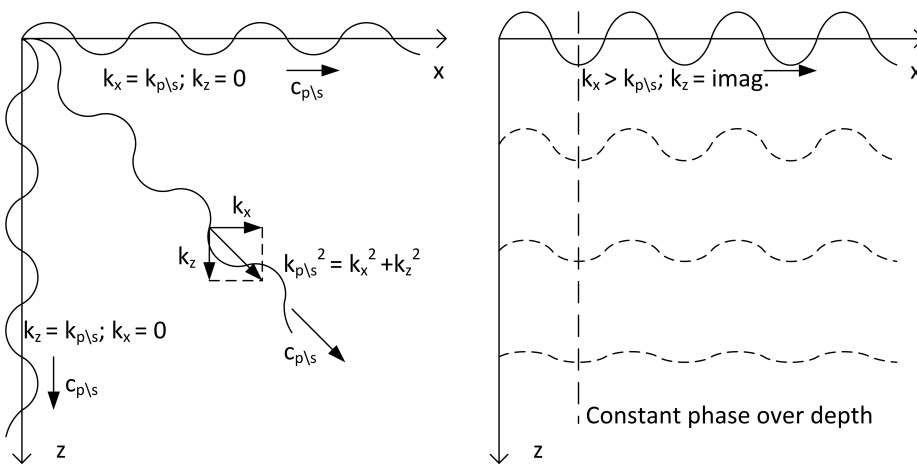


Figure 3.3: Harmonic propagating waves (left) and harmonic evanescent wave (right)

wave.

$$\begin{aligned}\tilde{u}_x &= -i \left[ k_x \left( a_1 e^{ik_{z,p}(z-h)} + a_2 e^{-ik_{z,p}z} \right) - k_{z,s} \left( b_1 e^{ik_{z,s}(z-h)} - b_2 e^{-ik_{z,s}z} \right) \right] e^{-ik_x x} \\ \tilde{u}_y &= -i \left[ c_1 e^{ik_{z,s}(z-h)} + c_2 e^{-ik_{z,s}z} \right] e^{-ik_x x} \\ \tilde{u}_z &= i \left[ k_{z,p} \left( a_1 e^{ik_{z,p}(z-h)} - a_2 e^{-ik_{z,p}z} \right) - k_x \left( b_1 e^{ik_{z,s}(z-h)} + b_2 e^{-ik_{z,s}z} \right) \right] e^{-ik_x x}\end{aligned}\quad (3.16)$$

By substituting Eq. (3.16) in Eq. (3.15), the expressions for the stresses are found, with the same unknowns as in Eq. (3.16).

$$\begin{aligned}\tilde{\sigma}_{xz} &= \mu \left[ 2k_x k_{z,p} \left( a_1 e^{ik_{z,p}(z-h)} - a_2 e^{-ik_{z,p}z} \right) + (k_{z,s}^2 - k_x^2) \left( b_1 e^{ik_{z,s}(z-h)} + b_2 e^{-ik_{z,s}z} \right) \right] e^{-ik_x x} \\ \tilde{\sigma}_{yz} &= \mu k_{z,s} \left[ c_1 e^{ik_{z,s}(z-h)} - c_2 e^{-ik_{z,s}z} \right] e^{-ik_x x} \\ \tilde{\sigma}_{zz} &= \mu \left[ - (k_{z,s}^2 - k_x^2) \left( a_1 e^{ik_{z,p}(z-h)} + a_2 e^{-ik_{z,p}z} \right) + 2k_{z,s} k_x \left( b_1 e^{ik_{z,s}(z-h)} - b_2 e^{-ik_{z,s}z} \right) \right] e^{-ik_x x}\end{aligned}\quad (3.17)$$

The SH-wave equation is described linear, while the PSV-wave is written in matrix notation:

$$\begin{aligned}\tilde{\mathbf{u}} &= \mathbf{R}_u \mathbf{E}_z \mathbf{a} e^{-ik_x x} \\ \tilde{\boldsymbol{\sigma}} &= \mathbf{R}_s \mathbf{E}_z \mathbf{a} e^{-ik_x x}\end{aligned}\quad (3.18)$$

In which:

$$\begin{aligned}\tilde{\mathbf{u}} &= [\tilde{u}_x \quad \tilde{u}_z]^T, \quad \tilde{\boldsymbol{\sigma}} = [\tilde{\sigma}_{xz} \quad \tilde{\sigma}_{zz}]^T \\ \mathbf{R}_u &= i \begin{bmatrix} -k_x & -k_x & -k_{z,s} & k_{z,s} \\ k_{z,p} & -k_{z,p} & -k_x & -k_x \end{bmatrix}, \quad \mathbf{R}_s = \mu \begin{bmatrix} 2k_x k_{z,p} & -2k_x k_{z,p} & -k_x^2 + k_{z,s} & -k_x^2 + k_{z,s} \\ k_x^2 - k_{z,s} & k_x^2 - k_{z,s} & 2k_x k_{z,s} & -2k_x k_{z,s} \end{bmatrix}, \\ \mathbf{E}_z &= \text{diag} \left[ e^{ik_{z,p}(z-h)} \quad e^{-ik_{z,p}z} \quad e^{ik_{z,s}(z-h)} \quad e^{-ik_{z,s}z} \right], \\ \mathbf{a} &= [a_1 \quad a_2 \quad b_1 \quad b_2]^T\end{aligned}\quad (3.19)$$

### 3.2.1. Free vibration solution

The solution to the free vibration of the soil is found by applying the homogeneous boundary conditions. Only the PSV-waves are considered hereafter. A solution is found for every wavenumber, with an unknown amplitude. The following homogeneous boundaries are applied at the surface:

$$\tilde{\sigma}_{xz} = \tilde{\sigma}_{zz} = 0 \quad (3.20)$$

The rigid boundary (bedrock) introduced at  $z = h$  does not allow displacements. Therefore, the other boundary conditions are:

$$\tilde{u}_x = \tilde{u}_z = 0 \quad (3.21)$$

By applying the boundary conditions from Eq. (3.20) and Eq. (3.21) on Eq. (3.17) and Eq. (3.18) the unknowns  $\mathbf{a}$ , can be found by:

$$\begin{bmatrix} \tilde{\boldsymbol{\sigma}} \\ \tilde{\mathbf{u}} \end{bmatrix} = \begin{bmatrix} \mathbf{R}_s \mathbf{E}_0 \\ \mathbf{R}_u \mathbf{E}_h \end{bmatrix} \mathbf{a} e^{-ik_x x} = \mathbf{0} \quad (3.22)$$

This equation has a non-trivial solution in the absence of external load only when the determinant of the matrix is equal to zero. The matrix is solved for the wavenumbers  $k_x$ :

$$\Delta = \text{Det} \begin{bmatrix} \mathbf{R}_s \mathbf{E}_0 \\ \mathbf{R}_u \mathbf{E}_h \end{bmatrix} = 0 \quad (3.23)$$

The determinant has infinite complex solutions  $k_n$  for variable  $k$ . The four unknowns can be substituted into each other by making use of 3 of the four equations of the boundary conditions and set one of the unknowns equal to one. The best solution is determined from sixteen sets of three equations (i.e. for each variable set to one there are four options). The best set is chosen by taking the condition number of the reduced matrix (i.e. a

3x3 matrix) which is the closest to one. This results in an infinite number of mode shapes  $\phi_n$ , depending on a corresponding wavenumbers  $k_n$  with an unknown amplitude  $A_n$ . The solution can be found by a summation over all modes.

$$u(x, z, \omega) = \sum_{n=1}^{\infty} A_n \phi_n(x, z, \omega, k_n) \quad (3.24)$$

### 3.2.2. Root-finder algorithm

An algorithm is used to find the unique solutions for the wavenumbers (roots)  $k_n$  by setting the determinant equal to zero. These roots are found along paths in the complex frequency wavenumber domain, as shown in figure 3.4 The roots are found by making use of two different algorithms. The two different techniques

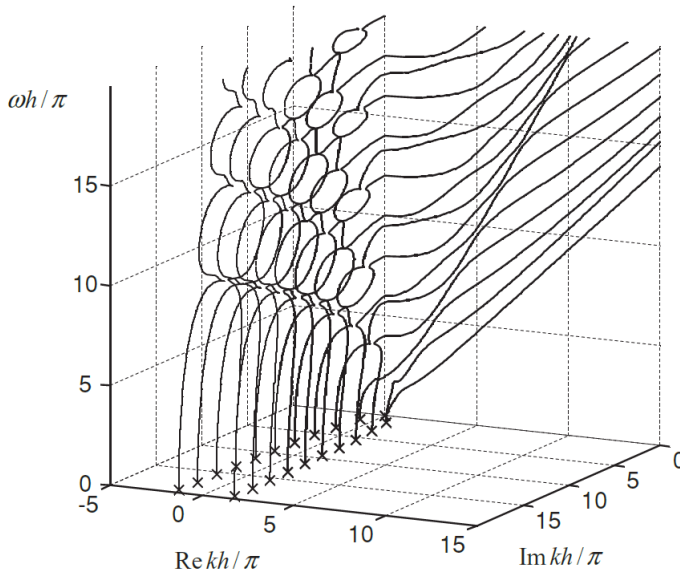


Figure 3.4: Path of symmetric roots in the complex frequency wavenumber domain for  $\nu = 0.31$ . (source: Kausel (2006))

are used to find respectively the pure real & imaginary roots and the complex roots. The two techniques the root-finder uses are:

- **A linear line-search:** This method searches linear along the real and imaginary axis to find a solution of which the real and imaginary part of the determinant is zero. The search domain on the real axis can be estimated by a multiplication of the S wavenumber. The search domain on the imaginary axis is more difficult to estimate. They are expected to be close to the origin. The only way to check whether all imaginary roots are found is by the convergence of the solution.
- **A search in the complex plane:** The roots  $k$  are found for which the dispersion relation is equal to zero. The search in the complex plane is based on the principle of the argument for a first estimation of the total roots in a pre-described area in one of the four quadrants of the complex domain since the roots can be mirrored by both axis. The algorithm divides the area in subregion, each containing one single root. Finally the roots are found by the position where the determinant is at a minimum.

Practically the algorithm will give the best approximation for the wavenumbers, which will never give a total zero solution of the determinant. The method is more extensively described in (Tsouvalas, 2015). The wavenumbers are found for normalized frequencies. The frequency ( $\omega$ ) is normalized by the shear-wave group velocity multiplied with the depth. The wavenumbers  $k_n$  are normalized with the shear-wavenumber which can be simplified by a multiplication with the height. Figure 3.5 shows the wavenumbers found for three normalized angular frequencies. The lowest frequency does not provide any roots corresponding to propagating waves while the other two higher frequencies do. The modes of the layer corresponding to the roots should fulfil the boundary conditions and the orthogonality principle. An impression of the first, second

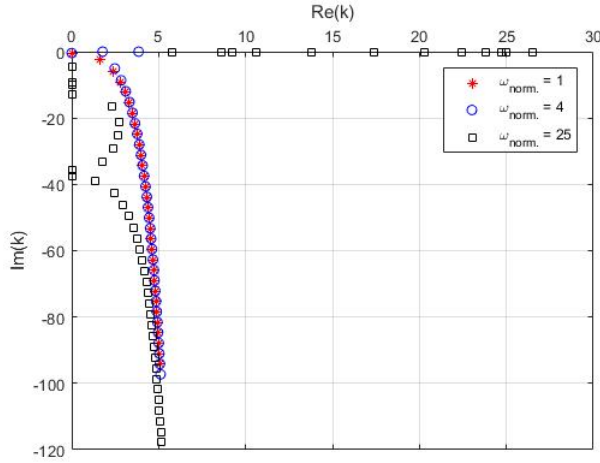


Figure 3.5: First 30 roots ( $k$ ) found in the fourth quadrant for normalized frequencies 1, 4 and 25. ( $\omega_{norm} = \frac{\omega h}{c_s}$ )

and fourth mode-shapes at  $x = 0$  over the height of the layer are shown in respectively figure 3.6, figure 3.7 and figure 3.8. The errors corresponding to the first 100 modes of the boundary conditions are shown in figure 3.9 and are negligible small. The modes fulfil the orthogonality principle, which confirms the correctness of the modes found.

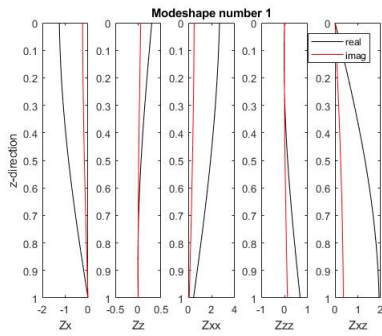


Figure 3.6: First modal deformation

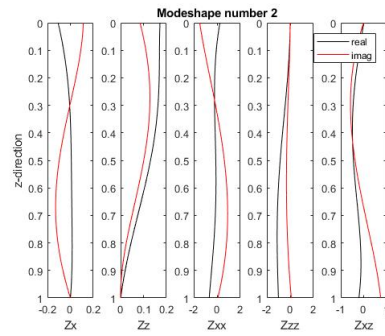


Figure 3.7: Second modal deformation

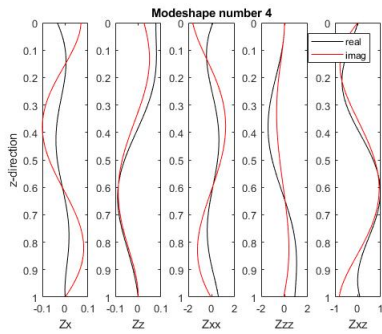


Figure 3.8: Fourth modal deformation

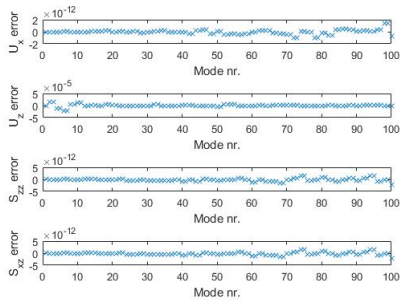


Figure 3.9: Normalized modal error at the boundaries

### 3.3. Force-displacement relation of the surface

In this subsection the force-displacement relation along the surface is determined. Therefore,  $z = 0$ . To obtain the force displacement relation, both a vertical and horizontal (shear) load are applied on the surface as shown in figure 3.1. From these two cases the relation between stress and displacement can be derived in a matrix form. The relation is written in the following way:

$$\begin{bmatrix} \tilde{u}_x(x + \delta x) \\ \tilde{u}_z(x + \delta x) \end{bmatrix} = \begin{bmatrix} R_{xx}(\delta x) & R_{zx}(\delta x) \\ R_{xz}(\delta x) & R_{zz}(\delta x) \end{bmatrix} \begin{bmatrix} \tilde{\sigma}_{xz}(x) \\ \tilde{\sigma}_{zz}(x) \end{bmatrix} \quad (3.25)$$

$\delta x$  expresses the distance from the location where the stress is applied in  $x$ . The relations can be found by substituting a unit force in either the horizontal or vertical stress boundary condition. So there are two cases of boundary conditions at the free surface ( $z = 0$ ). The boundaries are applied in the frequency wavenumber domain. The wavenumber domain is denoted with a hat above the variables. The two cases of boundary conditions can be written as:

**Case 1:**

$$\hat{\sigma}_{xz} = 0, \quad \hat{\sigma}_{zz} = \hat{F}_{zz}(k_x, \omega) \quad (3.26)$$

**Case 2:**

$$\hat{\sigma}_{zz} = 0, \quad \hat{\sigma}_{xz} = \hat{F}_{xz}(k_x, \omega)$$

The bedrock boundary at  $z = h$  remains as described in Eq. (3.21). The force is transferred to the frequency-wavenumber domain. The combination of the surface- and bedrock-boundary conditions for the first case, i.e. a vertical load is applied, reads:

$$\begin{bmatrix} \hat{\sigma}_{xz} \\ \hat{\sigma}_{zz} \\ \hat{u}_x \\ \hat{u}_z \end{bmatrix} = \begin{bmatrix} \mathbf{R}_s \mathbf{E}_0 \\ \mathbf{R}_u \mathbf{E}_h \end{bmatrix} \mathbf{a} = \begin{bmatrix} 0 \\ \hat{F}_{zz}(k_x, \omega) \\ 0 \\ 0 \end{bmatrix} \quad (3.27)$$

The unknowns  $\mathbf{a}$  in Eq. (3.27) are found analytically by making use of Maple. Substituting these unknowns into Eq. (3.18) give the full expression for the displacements and stresses.

$$\begin{aligned} a_1 &= \frac{-\hat{F}_{zz}(k_x, \omega)}{\Delta} \left( -(k_x^2 - k_{z,s}^2)(k_x^2 + k_{z,p}k_{z,s})e^{-ih(k_{z,p}+2k_{z,s})} + (k_x^2 - k_{z,s}^2)(k_x^2 - k_{z,p}k_{z,s})e^{-ik_{z,p}h} \right. \\ &\quad \left. + 4k_x^2k_{z,p}k_{z,s}e^{-ik_{z,s}h} \right) \\ a_2 &= \frac{-\hat{F}_{zz}(k_x, \omega)}{\Delta} \left( 4k_x^2k_{z,p}k_{z,s}e^{-ih(k_{z,p}+k_{z,s})} + (k_x^2 - k_{z,s}^2) \left( (k_x^2 - k_{z,p}k_{z,s})e^{-2ik_{z,s}h} - k_x^2 - k_{z,p}k_{z,s} \right) \right) \\ b_1 &= \frac{-\hat{F}_{zz}(k_x, \omega)}{\Delta} 2k_{z,p}k_x \left( (-k_x^2 - k_{z,p}k_{z,s})e^{-ih(2k_{z,p}+k_{z,s})} + (k_x^2 - k_{z,s}^2)e^{-ik_{z,p}h} - (k_x^2 - k_{z,p}k_{z,s})e^{-ik_{z,s}h} \right) \\ b_2 &= \frac{-\hat{F}_{zz}(k_x, \omega)}{\Delta} 2k_{z,p}k_x \left( (-k_x^2 + k_{z,s}^2)e^{-ih(k_{z,p}+k_{z,s})} + (k_x^2 - k_{z,p}k_{z,s})e^{-2ik_{z,p}h} + k_x^2 + k_{z,p}k_{z,s} \right) \end{aligned} \quad (3.28)$$

Where the determinant  $\Delta$  written out is:

$$\begin{aligned} \Delta &= \mu \left( \left( e^{-2ih(k_{z,p}+k_{z,s})} - e^{-2ik_{z,p}h} - e^{-2ik_{z,s}h} + 1 \right) k_x^6 \right. \\ &\quad \left. + \left( (5k_{z,p}k_{z,s} - 2k_{z,s}^2) \left( e^{-2i(k_{z,p}+k_{z,s})h} + 1 \right) + (5k_{z,p}k_{z,s} + 2k_{z,s}^2) \left( e^{-2ik_{z,p}h} + e^{-2ik_{z,s}h} \right) \right. \right. \\ &\quad \left. \left. - 16k_{z,p}k_{z,s}e^{-i(k_{z,p}+k_{z,s})h} \right) k_x^4 + \left( (k_{z,s}^4 + k_{z,p}k_{z,s}(4k_{z,p}k_{z,s} - 2k_{z,s}^2)) \left( e^{-2i(k_{z,p}+k_{z,s})h} + 1 \right) \right. \right. \\ &\quad \left. \left. + (-k_{z,s}^4 + k_{z,p}k_{z,s}(4k_{z,p}k_{z,s} - 2k_{z,s}^2)) \left( e^{-2ik_{z,p}h} + e^{-2ik_{z,s}h} \right) + 16k_{z,p}k_{z,s}^3e^{-i(k_{z,p}+k_{z,s})h} \right) k_x^2 \right. \\ &\quad \left. + \left( k_{z,p}k_{z,s}^5 \left( e^{-2ik_{z,s}h} + e^{-2ik_{z,p}h} + e^{-2i(k_{z,p}+k_{z,s})h} + 1 \right) \right) \right) \end{aligned} \quad (3.29)$$

Exactly the same procedure is done for the second case for a horizontal load:

$$\begin{bmatrix} \hat{\sigma}_{xz} \\ \hat{\sigma}_{zz} \\ \hat{u}_x \\ \hat{u}_z \end{bmatrix} = \begin{bmatrix} \mathbf{R}_s \mathbf{E}_0 \\ \mathbf{R}_u \mathbf{E}_h \end{bmatrix} \mathbf{a} = \begin{bmatrix} \hat{F}_{xz}(k_x, \omega) \\ 0 \\ 0 \\ 0 \end{bmatrix} \quad (3.30)$$

The unknowns  $\mathbf{a}$  for this case are:

$$\begin{aligned}
a_1 &= \frac{\hat{F}_{xz}(k_x, \omega)}{\Delta} 2k_{z,s}k_x \left( (k_x^2 + k_{z,p}k_{z,s})e^{-ih(k_{z,p}+2k_{z,s})} + (k_x^2 - k_{z,p}k_{z,s})e^{-ik_{z,p}h} + (-k_x^2 + k_{z,s}^2)e^{-ik_{z,s}h} \right) \\
a_2 &= \frac{-\hat{F}_{xz}(k_x, \omega)}{\Delta} 2k_{z,s}k_x \left( (-k_x^2 + k_{z,s}^2)e^{-ih(k_{z,p}+k_{z,s})} + (k_x^2 - k_{z,p}k_{z,s})e^{-2ik_{z,s}h} + k_x^2 + k_{z,p}k_{z,s} \right) \\
b_1 &= \frac{\hat{F}_{xz}(k_x, \omega)}{\Delta} \left( (-k_x^2 + k_{z,s}^2)(k_x^2 + k_{z,p}k_{z,s})e^{-ih(2k_{z,p}+k_{z,s})} + (k_x^2 - k_{z,s}^2)(k_x^2 - k_{z,p}k_{z,s})e^{-ik_{z,s}h} \right. \\
&\quad \left. + 4k_x^2k_{z,p}k_{z,s}e^{-ik_{z,p}h} \right) \\
b_2 &= \frac{\hat{F}_{xz}(k_x, \omega)}{\Delta} \left( (k_x^2 - k_{z,s}^2) \left( (k_x^2 - k_{z,p}k_{z,s})e^{-2ik_{z,p}h} - (k_x^2 + k_{z,p}k_{z,s}) \right) + 4k_x^2k_{z,p}k_{z,s}e^{-ih(k_{z,p}+k_{z,s})} \right)
\end{aligned} \tag{3.31}$$

The solution in the frequency-space domain is obtained by taking the inverse Fourier integral over Eq. (3.18) substituting the unknowns as shown in Eq. (3.32).

$$\begin{aligned}
\tilde{\sigma}_{zz} &= \frac{1}{2\pi} \int_{-\infty}^{\infty} \left[ -(k_{z,s}^2 - k_x^2) a_1 e^{ik_{z,p}z} - (k_{z,s}^2 - k_x^2) a_2 e^{-ik_{z,p}z} + 2k_{z,s}k_x b_1 e^{ik_{z,s}z} - 2k_{z,s}k_x b_2 e^{-ik_{z,s}z} \right] e^{-ik_x x} dk_x, \\
\tilde{\sigma}_{xz} &= \frac{1}{2\pi} \int_{-\infty}^{\infty} \left[ 2k_x k_{z,p} a_1 e^{ik_{z,p}z} - 2k_x k_{z,p} a_2 e^{-ik_{z,p}z} + (k_{z,s}^2 - k_x^2) b_1 e^{ik_{z,s}z} + (k_{z,s}^2 - k_x^2) b_2 e^{-ik_{z,s}z} \right] e^{-ik_x x} dk_x, \\
\tilde{u}_x &= \frac{-i}{2\pi\mu} \int_{-\infty}^{\infty} \left[ k_x a_1 e^{ik_{z,p}z} + k_x a_2 e^{-ik_{z,p}z} - k_{z,s} b_1 e^{ik_{z,s}z} + k_{z,s} b_2 e^{-ik_{z,s}z} \right] e^{-ik_x x} dk_x, \\
\tilde{u}_z &= \frac{i}{2\pi\mu} \int_{-\infty}^{\infty} \left[ k_{z,p} a_1 e^{ik_{z,p}z} - k_{z,p} a_2 e^{-ik_{z,p}z} - k_x b_1 e^{ik_{z,s}z} - k_x b_2 e^{-ik_{z,s}z} \right] e^{-ik_x x} dk_x
\end{aligned} \tag{3.32}$$

The applied force is assumed to be a stress-block around  $x = 0$ , with a normalized area, as shown in figure 3.1. Therefore, the reaction of this stress-block is in units of force. Since a linear approach is used, an amplification of the force linearly effects the displacements. For the derivation of the flexibility functions, the area  $S_{ii}$  is set to one. The force  $S_{ii}$  later-on will be the interaction force between the superstructure and the soil. Instead of a stress-block, a point load could be chosen, but a stress-block is preferred to overcome singularities.

$$\tilde{F}_{ii}(x, \omega) = -\frac{1}{b} H\left(\frac{b}{2} - |x|\right) \tag{3.33}$$

Wherein  $H(x)$  is the Heaviside formula i.e  $H(x > 0) = 1$  and  $H(x < 0) = 0$ . Taking its Fourier transform in  $x$  to write it in the applicable domain results in:

$$\tilde{F}_{ii}(x, \omega) = -\frac{1}{b} H\left(\frac{b}{2} - |x|\right) \tag{3.34}$$

$$\hat{F}_{ii}(k_x, \omega) = -\int_{-\infty}^{\infty} \tilde{F}_{ii}(x, \omega) e^{ik_x x} dx = -\int_{-\infty}^{\infty} \frac{1}{b} H\left(\frac{b}{2} - |x|\right) e^{ik_x x} dx \tag{3.35}$$

$$\hat{F}_{ii}(k_x, \omega) = -\int_{-\frac{b}{2}}^{\frac{b}{2}} \frac{1}{b} e^{ik_x x} dx = \frac{1}{ik_x b} e^{ik_x x} \Big|_{-\frac{b}{2}}^{\frac{b}{2}} = -\frac{1}{ik_x b} \left[ e^{i\frac{b}{2}k_x} - e^{-i\frac{b}{2}k_x} \right] = -\frac{1}{ik_x b} \left[ 2i \sin \frac{k_x b}{2} \right] \tag{3.36}$$

$$\hat{F}_{ii}(k_x, \omega) = -\frac{2}{k_x b} \sin\left(\frac{k_x b}{2}\right) \tag{3.37}$$

Eq. (3.37) can be substituted in Eq. (3.28) and Eq. (3.31). Since we are mainly interested in the surface loads, the substitution of  $z = 0$  is made for both situations. Obviously, as boundary condition, the stresses are equal to zero or equal to the applied stress. Therefore, the relation between stress and displacement at the surface

follows from the equations for the displacement. The flexibility functions are expressed as  $R_{ij}$ , where  $i$  is the direction of the stress and  $j$  is the direction of the displacement.

$$\begin{aligned}
\tilde{R}_{xx} &= -\frac{i}{2\pi} \int_{-\infty}^{\infty} \frac{\hat{F}_{xz}}{\Delta} k_{z,s} \left( (k_x^2 + k_{z,s}^2) \left( (k_x^2 + k_{z,p} k_{z,s}) e^{-2ih(k_{z,p} + k_{z,s})} + (k_x^2 - k_{z,p} k_{z,s}) e^{-2ik_{z,p}h} \right. \right. \\
&\quad \left. \left. + (-k_x^2 + k_{z,p} k_{z,s}) e^{-2ik_{z,s}h} - k_x^2 - k_{z,p} k_{z,s} \right) e^{-ik_x x} dk_x, \\
\tilde{R}_{zz} &= \frac{i}{2\pi} \int_{-\infty}^{\infty} \frac{\hat{F}_{zz}}{\Delta} k_{z,p} (k_x^2 + k_{z,s}^2) \left( (-k_x^2 - k_{z,p} k_{z,s}) e^{-2ih(k_{z,p} + k_{z,s})} + (k_x^2 - k_{z,p} k_{z,s}) e^{-2ik_{z,p}h} \right. \\
&\quad \left. + (-k_x^2 + k_{z,p} k_{z,s}) e^{-2ik_{z,s}h} + k_x^2 + k_{z,p} k_{z,s} \right) e^{-ik_x x} dk_x, \\
\tilde{R}_{zx} &= \frac{i}{2\pi} \int_{-\infty}^{\infty} \frac{\hat{F}_{zz}}{\Delta} k_x \left( -(k_x^2 + k_{z,p} k_{z,s}) (k_x^2 + 2k_{z,p} k_{z,s} - k_{z,s}^2) e^{-2ih(k_{z,p} + k_{z,s})} \right. \\
&\quad \left. + (12k_x^2 k_{z,p} k_{z,s} - 4k_{z,p} k_{z,s}^3) e^{-ih(k_{z,p} + k_{z,s})} + (k_x^2 - 2k_{z,p} k_{z,s} - k_{z,s}^2) (k_x^2 - k_{z,p} k_{z,s}) (e^{-2ik_{z,p}h} + e^{-2ik_{z,s}h}) \right. \\
&\quad \left. - (k_x^2 + k_{z,p} k_{z,s}) (k_x^2 + 2k_{z,p} k_{z,s} - k_{z,s}^2) \right) e^{-ik_x x} dk_x, \\
\tilde{R}_{xz} &= -\tilde{R}_{zx}
\end{aligned} \tag{3.38}$$

Together the terms in Eq. (3.38) form the flexibility matrix, i.e. it describes the displacement of a distance  $x$  from a stress-block with an area of 1 around  $x_0$ . As mentioned before, the flexibility matrix is linear. Therefore, it may be multiplied with the interaction force  $S_i$  to derive displacements for any force amplitude.

$$\begin{aligned}
\begin{bmatrix} \tilde{u}_x \\ \tilde{u}_z \end{bmatrix} &= \begin{bmatrix} \tilde{R}_{xx} & \tilde{R}_{zx} \\ \tilde{R}_{xz} & \tilde{R}_{zz} \end{bmatrix} \begin{bmatrix} \tilde{S}_x \\ \tilde{S}_z \end{bmatrix} \\
\tilde{\mathbf{u}}(x) &= \mathbf{R}(x - x_0) \tilde{\mathbf{S}}(x_0)
\end{aligned} \tag{3.39}$$

### 3.4. Contour integration

To solve the expression in the frequency-space domain, contour integration is used in combination with the residues theorem. The contour integral is formed by a summation of the integral from  $-\infty$  to  $\infty$  excluding singularities on the integration path, integration around the singularities on the integration path, and integration over the contour going to infinity. Figure 3.10 shows an integration path ( $C_\infty$ ) around the complex plane for a set of roots, indicating the php and nhp. There is one singularity on the complex plane at  $k_x = 0$  ( $C_0$ ), which is excluded out of the integration path. The positive real roots are included in the nhp and the negative real roots in the php as indicated.

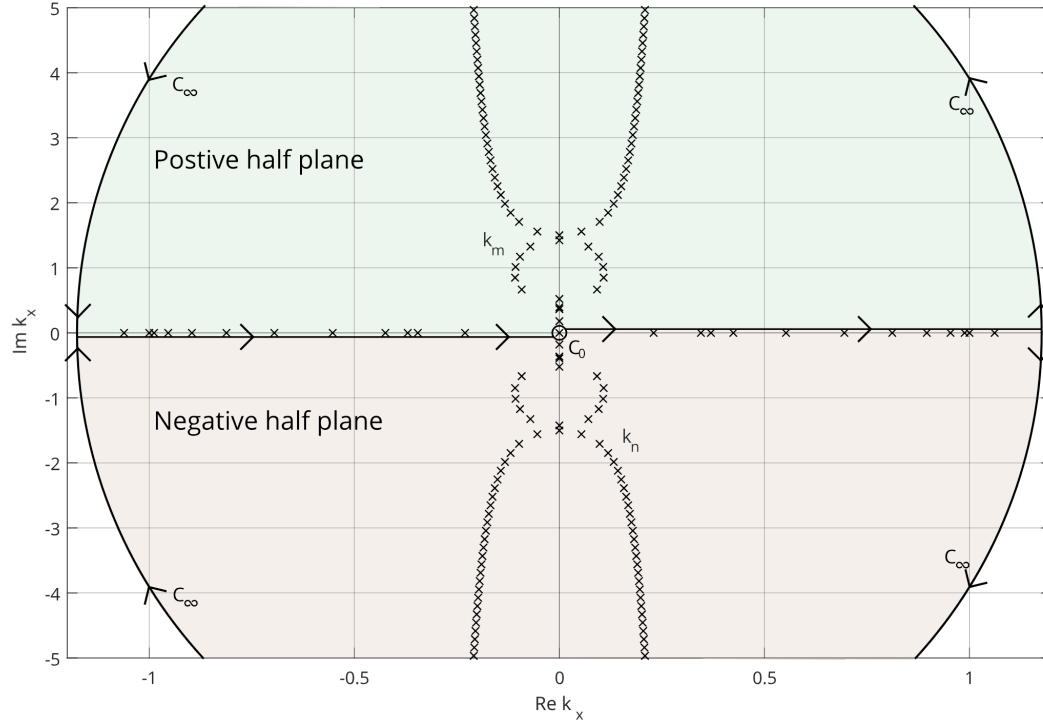


Figure 3.10: Integration around the complex plane

$$\oint_c = \int_{-\infty}^{\infty} + \int_{c_0} + \int_{C_\infty} \quad (3.40)$$

The contour integral equals the positive or negative sum of the residuals for respectively anticlockwise and clockwise integration.

$$\oint_c = \mp 2\pi i \sum_{n=1}^{\infty} \text{Res}(k_n) \quad (3.41)$$

Since the integral from  $-\infty$  to  $\infty$  needs to be solved and the integral over the contour drops, the integral results in:

$$\int_{-\infty}^{\infty} = \mp 2\pi i \sum_{n=1}^{\infty} \text{Res}(k_n) - \int_{c_0} \quad (3.42)$$

#### 3.4.1. Residue in a complex analysis

Residues are found for poles of a function in the complex plane. For simple poles, the residue can be found by setting a limit.

$$\text{Res}(f(z), c) = \lim_{z \rightarrow c} (z - c) f(z) \quad (3.43)$$

Considering a function  $f(z)$  can be written as a fraction of complex valued functions with the following condition:

$$f(z) = \frac{g(z)}{h(z)}, \quad h'(c) \neq 0, \quad \lim_{z \rightarrow c} (z - c) f(z) = \lim_{z \rightarrow c} \frac{zg(z) - cg(z)}{h(z)} = \lim_{z \rightarrow c} \frac{g(z) + zg'(z) - cg'(z)}{h'(z)} = \frac{g(c)}{h'(c)} \quad (3.44)$$



### 3.5. Solution in the frequency-space domain

Eq. (3.45) is the result of the substitution of Eq. (3.37) in Eq. (3.38). This resulting equation can be solved by making use of Eq. (3.42).

$$\begin{aligned}
\tilde{R}_{xx} &= \frac{i}{\pi b} \int_{-\infty}^{\infty} \frac{\sin\left(\frac{k_x b}{2}\right)}{k_x \Delta} k_{z,s} \left( (k_x^2 + k_{z,s}^2) \left( (k_x^2 + k_{z,p} k_{z,s}) e^{-2ih(k_{z,p} + k_{z,s})} + (k_x^2 - k_{z,p} k_{z,s}) e^{-2ik_{z,p}h} \right) \right. \\
&\quad \left. + (-k_x^2 + k_{z,p} k_{z,s}) e^{-2ik_{z,s}h} - k_x^2 - k_{z,p} k_{z,s} \right) e^{-ik_x x} dk_x \\
\tilde{R}_{zz} &= \frac{-i}{\pi b} \int_{-\infty}^{\infty} \frac{\sin\left(\frac{k_x b}{2}\right)}{k_x \Delta} k_{z,p} (k_x^2 + k_{z,s}^2) \left( (-k_x^2 - k_{z,p} k_{z,s}) e^{-2ih(k_{z,p} + k_{z,s})} + (k_x^2 - k_{z,p} k_{z,s}) e^{-2ik_{z,p}h} \right. \\
&\quad \left. + (-k_x^2 + k_{z,p} k_{z,s}) e^{-2ik_{z,s}h} + k_x^2 + k_{z,p} k_{z,s} \right) e^{-ik_x x} dk_x, \\
\tilde{R}_{zx} &= \frac{-i}{\pi b} \int_{-\infty}^{\infty} \frac{\sin\left(\frac{k_x b}{2}\right)}{k_x \Delta} k_x \left( -(k_x^2 + k_{z,p} k_{z,s}) (k_x^2 + 2k_{z,p} k_{z,s} - k_{z,s}^2) e^{-2ih(k_{z,p} + k_{z,s})} \right. \\
&\quad \left. + (12k_x^2 k_{z,p} k_{z,s} - 4k_{z,p} k_{z,s}^3) e^{-ih(k_{z,p} + k_{z,s})} + (k_x^2 - 2k_{z,p} k_{z,s} - k_{z,s}^2) (k_x^2 - k_{z,p} k_{z,s}) (e^{-2ik_{z,p}h} + e^{-2ik_{z,s}h}) \right. \\
&\quad \left. - (k_x^2 + k_{z,p} k_{z,s}) (k_x^2 + 2k_{z,p} k_{z,s} - k_{z,s}^2) \right) e^{-ik_x x} dk_x, \\
\tilde{R}_{xz} &= -\tilde{R}_{zx}
\end{aligned} \tag{3.45}$$

All integrals of Eq. (3.45) are of the following form:

$$\tilde{I}_{ii} = \frac{1}{2\pi} \int_{-\infty}^{\infty} \frac{2}{k_x b} \sin\left(\frac{k_x b}{2}\right) \frac{f_{ii}(k_x)}{\Delta(k_x)} e^{-ik_x x} dk_x \tag{3.46}$$

$$\sin\left(\frac{k_x b}{2}\right) = \frac{1}{2i} \left( e^{i\frac{k_x b}{2}} - e^{-i\frac{k_x b}{2}} \right) \tag{3.47}$$

$$e^{-ik_x x} = e^{-ix\Re(k_x) + x\Im(k_x)} \tag{3.48}$$

To apply the contour integral, Eq. (3.47) and Eq. (3.48) are substituted in Eq. (3.46). Two separate integrals appear since a sin is a summation of two exponential function.

$$\begin{aligned}
I &= I_1 + I_2 \\
I_1 &= \frac{1}{i2\pi b} \int_{-\infty}^{\infty} \frac{1}{k_x} \frac{f_{ii}(k_x)}{\Delta(k_x)} e^{i(\frac{b}{2}-x)\Re(k_x) - (\frac{b}{2}-x)\Im(k_x)} dk_x \\
I_2 &= \frac{-1}{i2\pi b} \int_{-\infty}^{\infty} \frac{1}{k_x} \frac{f_{ii}(k_x)}{\Delta(k_x)} e^{-i(\frac{b}{2}+x)\Re(k_x) + (\frac{b}{2}+x)\Im(k_x)} dk_x
\end{aligned} \tag{3.49}$$

To satisfy that the integral over the contour drops out, the real part of the integral may approach infinity, when  $x$  in the exponent approaches  $\infty$ , the following condition needs to be satisfied for both parts of the integral:  $\mp(\frac{b}{2} \mp x) \times \Im(k_x) < 0$ . This leads to the following conditions:

For  $I_1$  :

$$\frac{b}{2} - x > 0 \Rightarrow x < \frac{b}{2} \quad \rightarrow \quad \Im(k_x) > 0$$

$$\frac{b}{2} - x < 0 \Rightarrow x > \frac{b}{2} \quad \rightarrow \quad \Im(k_x) < 0$$

For  $I_2$  :

$$\frac{b}{2} + x > 0 \Rightarrow x > -\frac{b}{2} \quad \rightarrow \quad \Im(k_x) < 0$$

$$\frac{b}{2} + x < 0 \Rightarrow x < -\frac{b}{2} \quad \rightarrow \quad \Im(k_x) > 0$$

(3.50)

Eq. (3.50) leads to four equations: for every condition one equation, where  $k_m = \Im(k_x) > 0$  (i.e. the roots in the php) leads to anticlockwise contour integrating over the positive half plane (php) and  $k_n = \Im(k_x) < 0$ , i.e.

the roots in the nhp, leads to clockwise contour integrating over the negative half plane (nhp). The residue for a pole  $k_n$  of  $I_1$  and  $I_2$  are found from Eq. (3.43) and Eq. (3.44). The same procedure is done for  $k_m$  instead of  $k_n$ , which gives the results for the residues in the php.

$$\begin{aligned} \text{Res}(I_1(k_x), k_n) &= \frac{1}{i2\pi b} \frac{1}{k_n} \frac{f_{ii}(k_n)}{\frac{\partial \Delta(k_n)}{\partial k_x}} e^{i(\frac{b}{2}-x)\Re(k_n) - (\frac{b}{2}-x)\Im(k_n)}, \\ \text{Res}(I_2(k_x), k_n) &= \frac{-1}{i2\pi b} \frac{1}{k_n} \frac{f_{ii}(k_n)}{\frac{\partial \Delta(k_n)}{\partial k_x}} e^{-i(\frac{b}{2}+x)\Re(k_n) + (\frac{b}{2}+x)\Im(k_n)} \end{aligned} \quad (3.51)$$

The integral around the singularity  $k_x = 0$  depends on rotational coefficient  $\phi$  and radius  $\delta$ , of which the limit from  $\delta \rightarrow 0$  is taken.

$$k_{x0} = \lim_{\delta \rightarrow 0} \delta e^{i\phi}, \quad dk_{x0} = \lim_{\delta \rightarrow 0} i\delta e^{i\phi} d\phi \quad (3.52)$$

Depending on the integration path  $\phi = [\pi, 0]$  or  $\phi = [-\pi, 0]$  for respectively anticlockwise and clockwise integration. The contour integral around the origin is taken by substituting Eq. (3.52) in Eq. (3.49). The integral around the singularity results in:

$$\begin{aligned} \int_{c0} I_1|_{x < \frac{b}{2}} &= \frac{1}{i2\pi b} \lim_{\delta \rightarrow 0} \int_{\pi}^0 \frac{1}{\delta e^{i\phi}} \frac{f_{ii}(\delta e^{i\phi})}{\Delta(\delta e^{i\phi})} e^{i(\frac{b}{2}-x)\Re(\delta e^{i\phi}) - (\frac{b}{2}-x)\Im(\delta e^{i\phi})} i\delta e^{i\phi} d\phi \\ &= \frac{1}{2\pi b} \lim_{\delta \rightarrow 0} \int_{\pi}^0 \frac{f_{ii}(\delta e^{i\phi})}{\Delta(\delta e^{i\phi})} e^{i(\frac{b}{2}-x)\Re(\delta e^{i\phi}) - (\frac{b}{2}-x)\Im(\delta e^{i\phi})} d\phi \\ &= \frac{1}{2\pi b} \int_{\pi}^0 \frac{f_{ii}(0)}{\Delta(0)} d\phi \\ &= \frac{-\pi}{2\pi b} \frac{f_{ii}(0)}{\Delta(0)} \end{aligned} \quad (3.53)$$

$$\begin{aligned} \int_{c0} I_1|_{x > \frac{b}{2}} &= \frac{1}{i2\pi b} \lim_{\delta \rightarrow 0} \int_{-\pi}^0 \frac{1}{\delta e^{i\phi}} \frac{f_{ii}(\delta e^{i\phi})}{\Delta(\delta e^{i\phi})} e^{i(\frac{b}{2}-x)\Re(\delta e^{i\phi}) - (\frac{b}{2}-x)\Im(\delta e^{i\phi})} i\delta e^{i\phi} d\phi \\ &= \frac{\pi}{2\pi b} \frac{f_{ii}(0)}{\Delta(0)} \end{aligned} \quad (3.54)$$

$$\begin{aligned} \int_{c0} I_2|_{x > -\frac{b}{2}} &= \frac{-1}{i2\pi b} \lim_{\delta \rightarrow 0} \int_{\pi}^0 \frac{1}{\delta e^{i\phi}} \frac{f_{ii}(\delta e^{i\phi})}{\Delta(\delta e^{i\phi})} e^{-i(\frac{b}{2}+x)\Re(\delta e^{i\phi}) + (\frac{b}{2}+x)\Im(\delta e^{i\phi})} i\delta e^{i\phi} d\phi \\ &= \frac{-\pi}{2\pi b} \frac{f_{ii}(0)}{\Delta(0)} \end{aligned} \quad (3.55)$$

$$\begin{aligned} \int_{c0} I_2|_{x < -\frac{b}{2}} &= \frac{-1}{i2\pi b} \lim_{\delta \rightarrow 0} \int_{-\pi}^0 \frac{1}{\delta e^{i\phi}} \frac{f_{ii}(\delta e^{i\phi})}{\Delta(\delta e^{i\phi})} e^{-i(\frac{b}{2}+x)\Re(\delta e^{i\phi}) + (\frac{b}{2}+x)\Im(\delta e^{i\phi})} i\delta e^{i\phi} d\phi \\ &= \frac{\pi}{2\pi b} \frac{f_{ii}(0)}{\Delta(0)} \end{aligned} \quad (3.56)$$

Substituting Eq. (3.51), Eq. (3.53), Eq. (3.54), Eq. (3.55) and Eq. (3.56) in Eq. (3.42) gives the solution to the complete integral, making use of Heaviside functions.

$$\begin{aligned} \int_{-\infty}^{\infty} I_{ii} &= \frac{1}{b} \left( \sum_{m=1}^m \frac{1}{k_m} \frac{f_{ii}(k_m)}{\frac{\partial \Delta(k_m)}{\partial k_x}} e^{i(\frac{b}{2}-x)\Re(k_m) - (\frac{b}{2}-x)\Im(k_m)} H\left(\frac{b}{2} - x\right) - \frac{1}{k_m} \frac{f_{ii}(k_m)}{\frac{\partial \Delta(k_m)}{\partial k_x}} e^{-i(\frac{b}{2}+x)\Re(k_m) + (\frac{b}{2}+x)\Im(k_m)} H\left(-\frac{b}{2} - x\right) \right. \\ &\quad + \sum_{n=1}^n \frac{1}{k_n} \frac{f_{ii}(k_n)}{\frac{\partial \Delta(k_n)}{\partial k_x}} e^{i(\frac{b}{2}-x)\Re(k_n) - (\frac{b}{2}-x)\Im(k_n)} H\left(-\frac{b}{2} + x\right) + \frac{1}{k_n} \frac{f_{ii}(k_n)}{\frac{\partial \Delta(k_n)}{\partial k_x}} e^{-i(\frac{b}{2}+x)\Re(k_n) + (\frac{b}{2}+x)\Im(k_n)} H\left(\frac{b}{2} + x\right) \\ &\quad \left. + \frac{1}{2} \frac{f_{ii}(0)}{\Delta(0)} \left( H\left(\frac{b}{2} - x\right) - H\left(-\frac{b}{2} - x\right) - H\left(-\frac{b}{2} + x\right) + H\left(\frac{b}{2} + x\right) \right) \right) \end{aligned}$$

(3.57)

Eq. (3.57) is a general solution of the integrals within the flexibility function described in Eq. (3.45). Applying this integration to the flexibility functions describes a linear relation between one stress-block and a displacement at any point. Since the relations are all linear, in the case of multiple stress-blocks, the displacements can be found by the sum of the effect of each, or in a more analytic way, the total displacement can be found by integrating over all stress-blocks having infinite small width  $dx$  (resulting in the Dirac method). For the SSI later-on, numerical integration is used, which results in the summation over all forces  $S_{ii}$  present at the interface. Therefore, a full flexibility matrix is formed and from the inverse, a stiffness matrix. As an example, figure 3.11 shows the solution of the flexibility function with the material properties of the soil from table 3.1 for harmonic loads with frequencies 0.77, 3.09 and 19.30 Hz and a corresponding amplitude of 1 kN over a width of 1 meter.

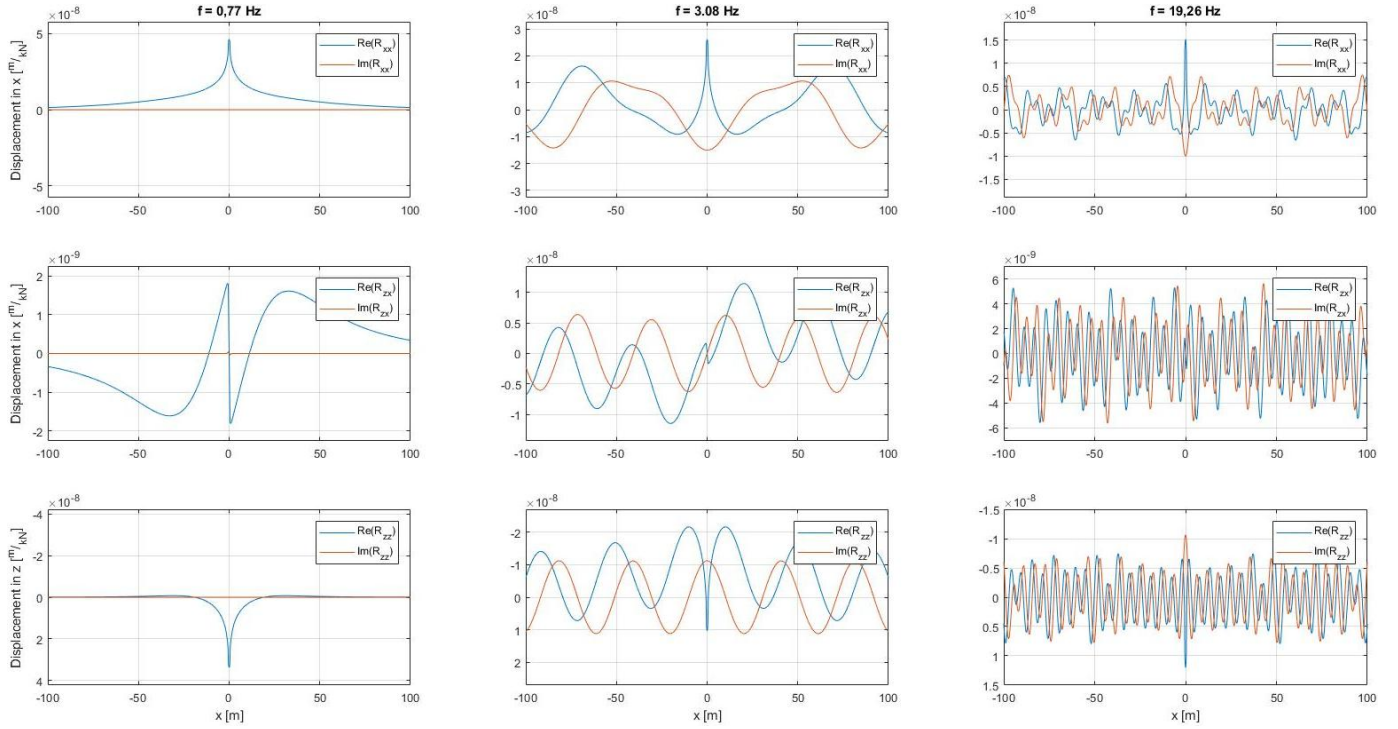


Figure 3.11: Resulting displacements due to stress-block around 0, derived from the flexibility functions

### 3.5.1. 2D soil stiffness matrix

A global stiffness matrix is formed by summation of flexibility functions. The global matrix is based on an elements with a single node in the center. Therefore, the flexibility function relates  $n$  displacements at a distance  $r$  corresponding to  $n$  stress-blocks.

$$\tilde{\mathbf{u}}_n = \mathbf{R}_r \tilde{\mathbf{S}} = \begin{bmatrix} R_{xx} & R_{zx} \\ R_{xz} & R_{zz} \end{bmatrix}_r \begin{bmatrix} \tilde{S}_x \\ \tilde{S}_z \end{bmatrix}_n \quad (3.58)$$

This can be written in a  $2n \times 2n$  global matrix, where the flexibility functions in  $xx$ ,  $zz$  and the cross relations are separated.

$$\begin{bmatrix} \tilde{u}_{x,1} \\ \vdots \\ \tilde{u}_{x,n} \\ \tilde{u}_{z,1} \\ \vdots \\ \tilde{u}_{z,n} \end{bmatrix} = \begin{bmatrix} \tilde{\mathbf{R}}_{xx,[n,n]} \\ \tilde{\mathbf{R}}_{xz,[n,n]} \end{bmatrix} \begin{bmatrix} \tilde{\mathbf{R}}_{zx,[n,n]} \\ \tilde{\mathbf{R}}_{zz,[n,n]} \end{bmatrix} \begin{bmatrix} \tilde{S}_{x,1} \\ \vdots \\ \tilde{S}_{x,n} \\ \tilde{S}_{z,1} \\ \vdots \\ \tilde{S}_{z,n} \end{bmatrix} \quad (3.59)$$

$$\tilde{\mathbf{u}} = \tilde{\mathbf{R}} \tilde{\mathbf{S}}$$

By inverting the global flexibility matrix the frequency-dependent stiffness matrix can be formed, i.e.  $\tilde{\mathbf{K}}_s = \tilde{\mathbf{R}}^{-1}$ . This stiffness matrix is widely used in dynamics and is used for the SSI wherein the subscript s indicates soil.

$$\tilde{\mathbf{S}}_s = \tilde{\mathbf{K}}_s \tilde{\mathbf{u}}_s \quad (3.60)$$

### 3.6. Convergence of the 2D soil problem

The correctness of the solution depends on the amount of soil modes included. In theory there is an infinite amount of soil modes which should be included, but from theory, it is known that the higher complex modes have less influence on the solution since their influence is very local. Missing one of the real or imaginary roots on the contrary has a rather large effect on the accuracy of the solution. To control whether enough complex roots are included and no major roots are missing, the convergence of the solution is checked. A way to verify whether the solution converges, is to check the smoothness of the flexibility functions. The solution is build up out of four, of which two symmetrical domains, separated with Heaviside formulas, on both sides of the borders of the applied stress block. For the frequencies 3.09 Hz and 19.30 Hz both flexibility functions  $R_{zz}$  and  $R_{xx}$  are shown with and without complex modes in figure 3.12. The difference in smoothness around

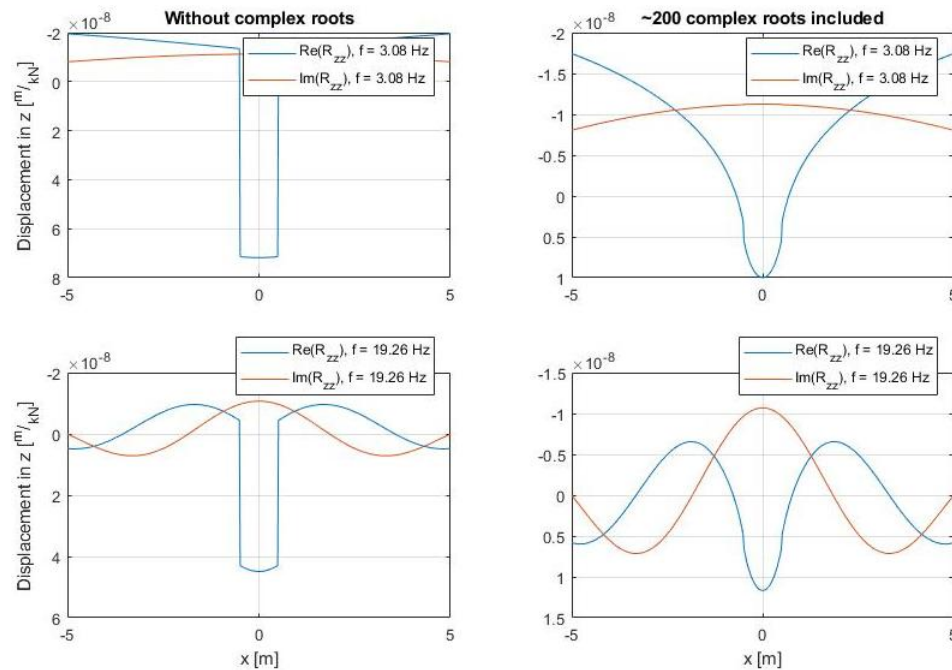


Figure 3.12: Discontinuity in displacement field with and without including complex modes

$\pm 0.5$  is clearly visible. The size of the discontinuity reduces a lot by including complex modes. The amount of complex roots included mainly influences the near field since their influence will decay rapidly further away from the source. The effect of the real, imaginary and complex roots on the size of the discontinuity are shown in figure 3.13 and figure 3.14. The two graphs on top show the influence of every single root on the discontinuity for respectively the real (left) and imaginary (right) part of the flexibility functions  $R_{xx}$  (red) and  $R_{zz}$  (blue), where the bottom two graphs show respectively the cumulative influence, i.e. zero means no discontinuity. The frequencies 3.09 Hz and 19.30 Hz have respectively two and twelve real roots and one and four imaginary roots. Both cases clearly show that the real and imaginary roots have the largest influence on the continuity of the flexibility functions. If the function does not converge, it is most likely that a real or imaginary root is missing. The complex roots cause the final convergence. Loads with a high frequency need more complex roots to converge than low frequency loads. It is expected that when SSI is applied, the solution will be sensitive to the amount of complex roots included.

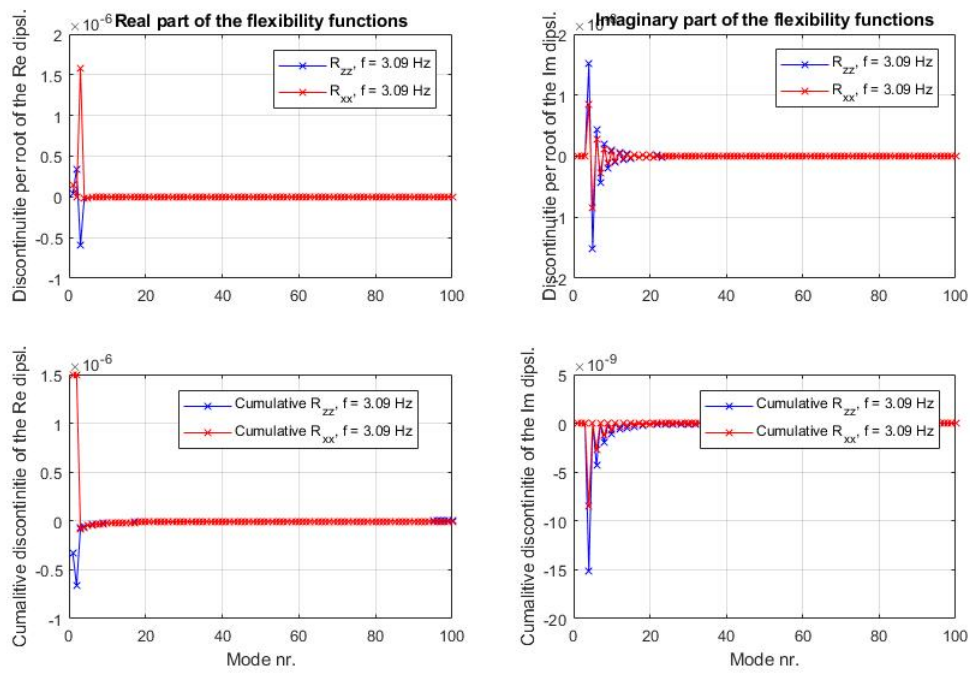


Figure 3.13: Convergence of the flexibility function in terms of the size of the discontinuity  $R_{xx}$  and  $R_{zz}$  ( $f = 3.09$  Hz)

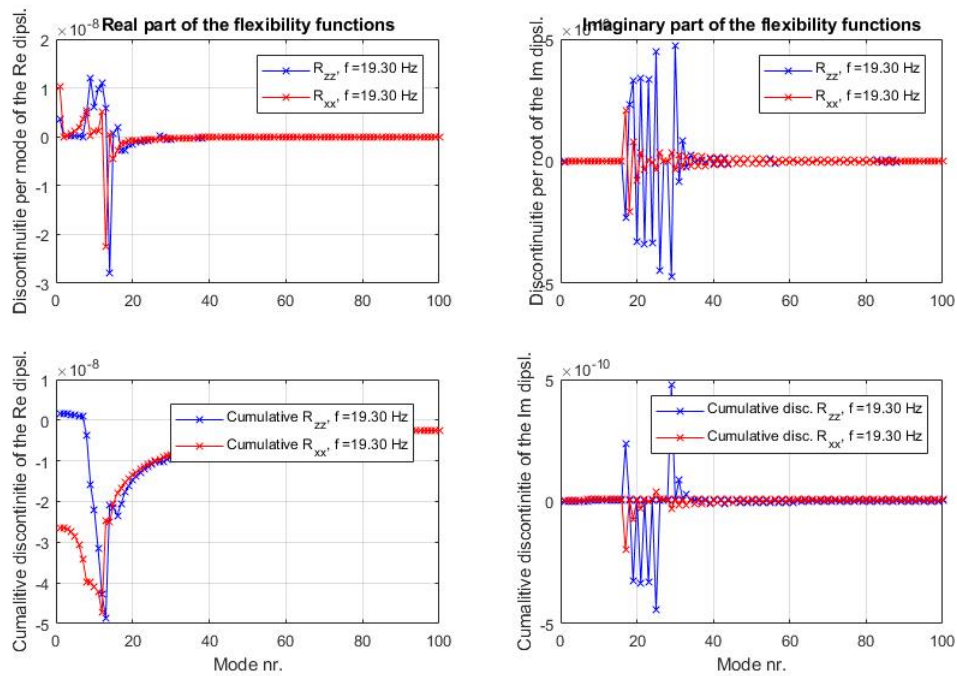


Figure 3.14: Convergence of the flexibility function in terms of the size of the discontinuity  $R_{xx}$  and  $R_{zz}$  ( $f = 19.30$  Hz)

### 3.7. Validation for the static case ( $\omega = 0$ )

The 2D soil model is validated for the static case. The static situation is approximated by a very low frequency of 0.08 Hz. This frequency is a lot lower than the first resonance frequency of the system. Therefore, it approximates the static case. The model is validated with respect to well-known work of Gazetas (1983), which refers to a rigid massless strip foundation on a shallow soil layer over a rigid bedrock. The static stiffness is described for the vertical, horizontal and rocking stiffness, depending on the depth-width ratio of the soil layer and strip. The vertical and horizontal stiffness of the model are determined by integration over the interaction stress that corresponds to an applied uniform vertical or horizontal displacement. The 'rocking' stiffness of the model is determined by integration over the vertical interaction stresses corresponding to linearly decaying vertical displacement of the beam. The strip is not restricted to rotate in case of horizontal loading and vice versa. All cases are shown in figure 3.15. The values for the stiffness are found by Eq. (3.61) (Gazetas, 1983).

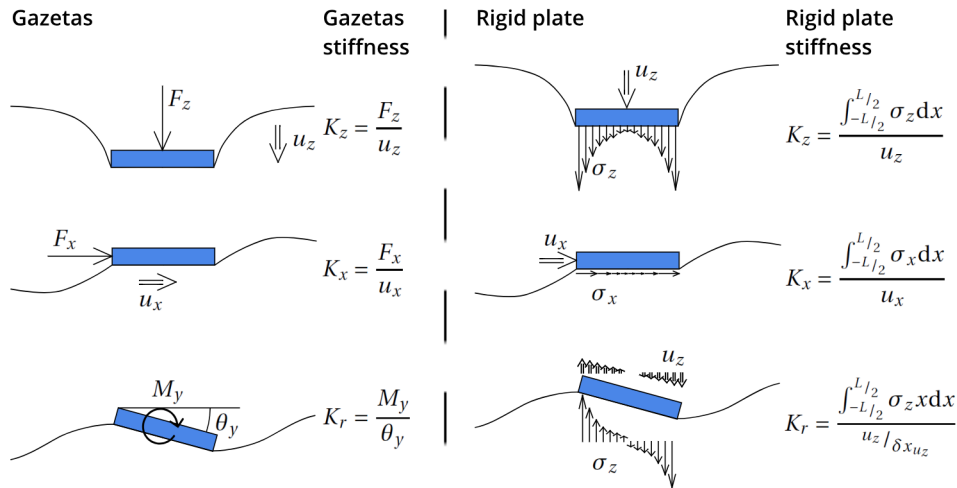


Figure 3.15: Convergence of the flexibility function in terms of the size of the discontinuity  $R_{xx}$  and  $R_{zz}$  ( $f = 3.09$  Hz)

$$\begin{aligned}
 K_z = \frac{F_z}{u_z} &= \frac{1.23\mu}{1-\nu} \left(1 + \frac{7a}{2h}\right) & 1 \leq \frac{h}{a} \leq 10 \\
 K_x = \frac{F_x}{u_x} &= \frac{2.1\mu}{2-\nu} \left(1 + \frac{a}{2h}\right) & 1 \leq \frac{h}{a} \leq 8 \\
 K_r = \frac{M_y}{\varphi_y} &= \frac{\pi\mu a^2}{8(1-\nu)} \left(1 + \frac{a}{5h}\right) & 1 \leq \frac{h}{a} \leq 3
 \end{aligned} \tag{3.61}$$

Wherein the width of the strip used by Gazetas (1983) is equal to half of the width used aforementioned:  $a = \frac{b}{2}$ . However the range of validity is limited, Gazetas (1983) states that also outside the range the expressions provide a good estimation of the stiffness. The vertical and horizontal stiffness are also compared to the stiffness of a single element derived from Eq. (3.45). The stiffness is determined by dividing the average displacement under the load. It is assumed that the load over the element is constant, the response of the soil is not restricted, and therefore the soil is fully flexible.

h/a	Gazetas	Rigid plate	Error	Single element	Error
2	1.41e8	1.50e8	7%	1.39e8	-1%
3	1.11e8	1.10e8	-1%	1.02e8	-8%
4	9.61e7	9.06e7	-6%	8.48e7	-13%
25	5.84e7	4.45e7	-31%	3.92e7	-33%

Table 3.2: Validation of the vertical stiffness  $K_z$  of a rigid strip in [N/m] and relative error [%]

The stiffnesses are compared in table 3.2 to table 5.3. The 2D model matches the analytical of Gazetas (1983) within 7% in all cases within the domain of validity. The stiffness of a single element is obviously less, since the deformation of the soil is not restricted. In general, the model preforms as expected compared to the reference.

h/a	Gazetas	Rigid plate	Error	Single element	Error
2	6.56e7	6.53e7	0%	6.24e7	-5%
3	5.47e7	5.51e7	1%	5.28e7	-3%
4	4.92e7	4.94e7	0%	4.75e7	-3%
25	3.54e7	2.93e7	-17%	2.86e7	-19%

Table 3.3: Validation of the horizontal stiffness  $K_x$  of a rigid strip in [N/m] and relative error [%]

h/a	Gazetas	Rigid plate	Error
2	1.12e10	1.2e10	7%
3	4.85e9	4.88e9	1%
4	2.68e9	2.65e9	-1%
25	6.60e7	6.27e7	-5%

Table 3.4: Validation of the rocking stiffness  $K_r$  of a rigid strip in [N/m] and relative error [%]

### 3.8. Frequency dependency of the soil stiffness

The complex stiffness of the soil varies for different frequencies. The frequencies in the model are represented normalized with respect to the height and shear wave speed of the soil layer ( $\omega_{norm.} = \frac{\omega h}{c_s}$ ). The normalized frequencies considered are 0.5, 1, 2, 3, 4, 5, 10, 15, 20 and 25 corresponding to respectively 0.39, 0.77, 1.54, 2.32, 3.09, 3.86, 7.72, 11.58, 15.44 and 19.30 Hz. To examine the frequency-dependent stiffness of the layer, first the frequencies of the resonance modes of the soil are found. The dispersion relation for the ten lowest modes of the layer vibrations are shown in figure 3.16 based on a zero determinant from Eq. (3.27). Resonance frequencies of the layer are found for  $k_x = 0$ . The first frequency of the fundamental shear and compression

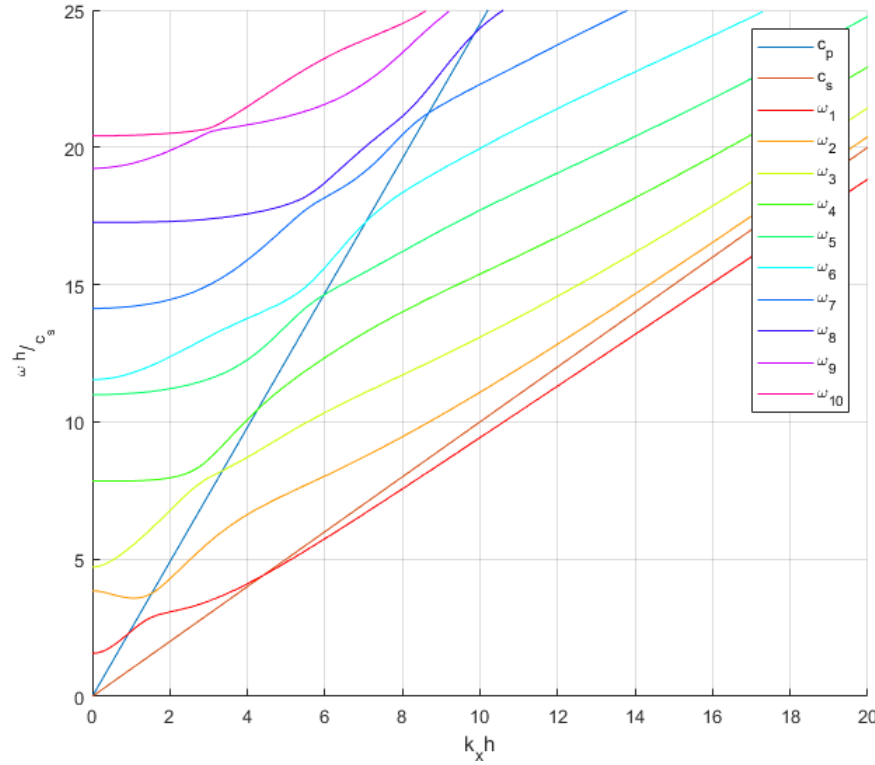


Figure 3.16: Dispersion relation for the ten lowest modes

mode of a single layer on bedrock can be found by the 1D approximation from Dobry et al. (1976). Based on the first mode shape  $\phi = \cos(\frac{\omega}{c})z$  with  $\omega_1 = \frac{\pi c}{2h}$  to satisfy the boundary conditions. The fundamental frequencies of the shear and compression mode are found by substituting the shear and compression wave speed in  $c$ .

$$\begin{aligned} \omega_{s,1} &= \frac{\pi c_s}{2h} & \Rightarrow & \frac{\omega_{s,1} h}{c_s} = \frac{\pi}{2} \approx 1.57 \\ \omega_{p,1} &= \frac{\pi c_p}{2h} & \Rightarrow & \frac{\omega_{p,1} h}{c_s} = \frac{\pi c_p}{2c_s} \approx 3.85 \end{aligned} \quad (3.62)$$

The frequencies found in Eq. (3.62) match the first and second fundamental frequency shown in figure 3.16. To examine the frequency-dependent stiffness of the soil, the complex stiffness  $\mathbf{K}$  is split in a real and imaginary part representing the stiffness and damping. The frequency-dependent stiffness and damping are normalized with respect to the static stiffness  $K_s$ :

$$\mathbf{K} = K_s (k + i\omega c) \quad (3.63)$$

It is convenient to normalize the frequency with the half of the strip width and shear wave length ratio to compare results of different  $h/a$  ratios:

$$a_0 = \frac{\omega a}{c_s} \quad (3.64)$$

Therefore, the damping coefficient in Eq. (3.63) modifies:

$$c_0 = c \frac{c_s}{a} \quad (3.65)$$

Substituting Eq. (3.65) in Eq. (3.63) results in:

$$\mathbf{K} = K (k + i a_0 c_0) \quad (3.66)$$

Figure 3.17 to figure 3.22 show the dependence of the stiffness and damping-coefficient on normalized frequencies for different  $h/a$  ratios. The first three normalized frequencies from figure 3.16 of the fundamental modes for ratio 3, 4, and 25 are:

$h/a$	$a_{0,1} = a_{0,s1}$	$a_{0,2} = a_{0,p1}$	$a_{0,3}$
3	0.52	1.28	1.57
4	0.39	0.96	1.18
25	0.06	0.15	0.19

Table 3.5: First three natural frequencies of a single layer

### Vertical stiffness and damping

The vertical stiffness and damping are strongly sensitive to a variation in frequency. The material is undamped and fully elastic, and therefore no damping is observed for the static case. Since no propagating surface waves can exist for frequencies under the first resonance frequency, no energy propagates horizontally away from the beam and because of the bedrock condition energy cannot leave the system downwards. The steep fluctuation in stiffness and damping can be declared by the absence of hysteretic and material damping. Figure 3.17 and figure 3.18 show the normalized frequency-dependent vertical stiffness and damping for  $h/a$  ratios 3, 4 and 25. The vertical lines show the second (and ninth) resonance frequency that match noticeably good with the reduction in stiffness. The second resonance frequency matches the frequency of the first fundamental compression mode as aforementioned. This is reasonable since the vertical stiffness of the shallow soil layer corresponds to compression of the soil by a rigid plate.

### Horizontal stiffness and damping

The horizontal stiffness and damping similar to the vertical stiffness and damping are strongly sensitive to a variation in frequency. No damping is observed before the first resonance frequency of the layer and the fluctuation of both stiffness and damping is rather steep. Figure 3.19 and figure 3.20 show the normalized frequency-dependent horizontal stiffness and damping for  $h/a$  ratios 3, 4 and 25. The vertical lines show the first, third and seventh resonance frequency that match noticeably good with the reduction in horizontal stiffness. As aforementioned, the first natural frequency is related to the frequency of the fundamental shear mode. It is reasonable that the horizontal stiffness and damping strongly depend on the fundamental shear mode, since the displacement of the rigid strip is parallel to the bedrock.

### Rocking stiffness and damping

The rocking stiffness and damping are less sensitive to the frequency. The stiffness reduces slightly with an increasing frequency. Damping is observed after the first resonance frequency of the soil, but quickly approaches an almost constant value. Figure 3.20 and figure 3.21 show the normalized frequency dependent rocking stiffness and damping. The vertical lines show the first and second resonance frequency of the layer, corresponding to the fundamental shear and compressional mode of the layer. The rocking stiffness is not clearly susceptible to one of the two.

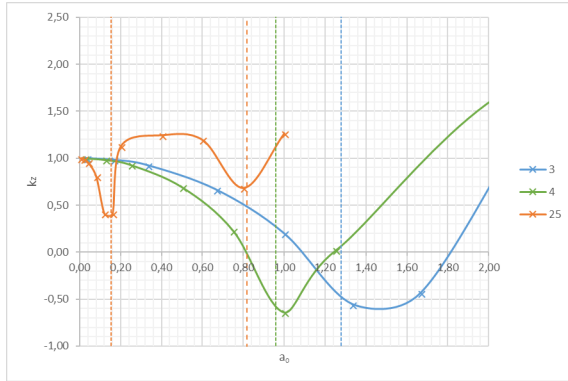


Figure 3.17: Normalized stiffness coefficient  $k_z$ .

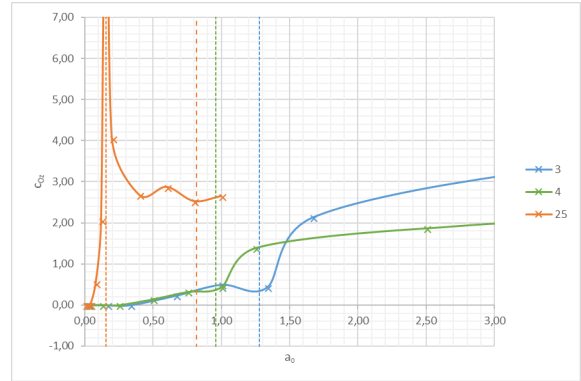


Figure 3.18: Normalized damping coefficient  $c_z$ .

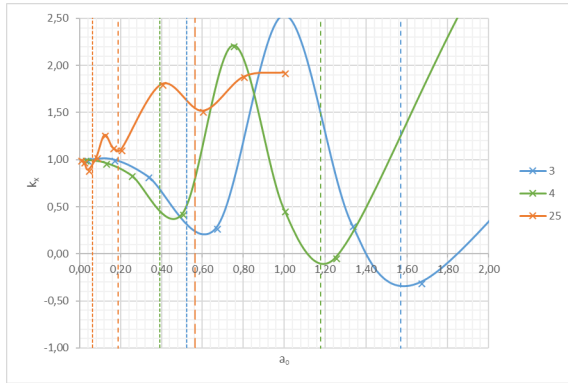


Figure 3.19: Normalized stiffness coefficient  $k_x$ .

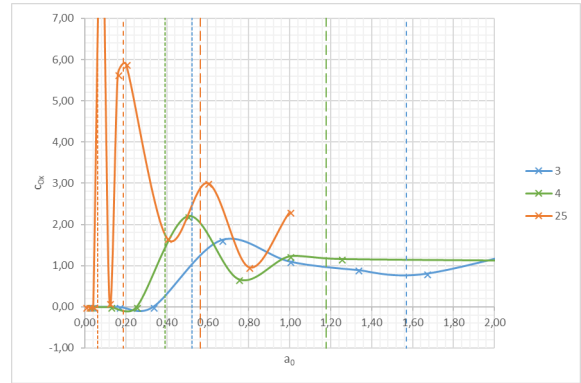


Figure 3.20: Normalized damping coefficient  $c_x$ .

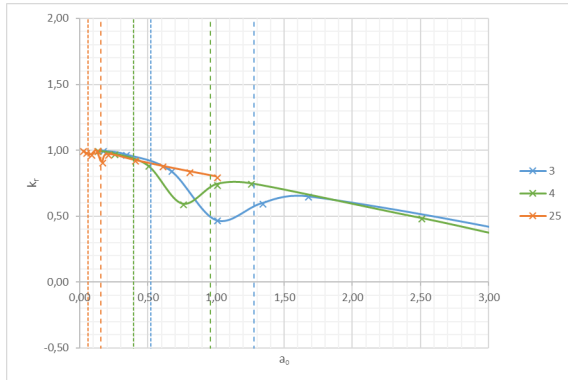


Figure 3.21: Normalized stiffness coefficient  $k_r$ .

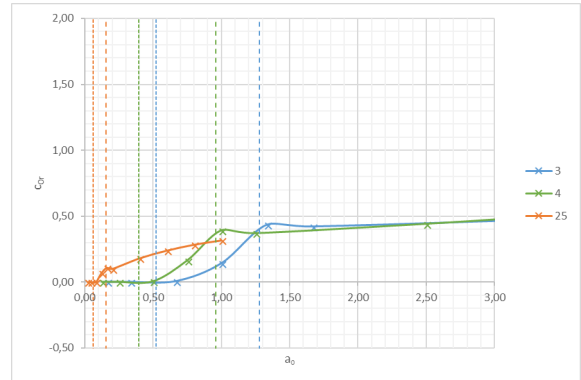


Figure 3.22: Normalized damping coefficient  $c_r$ .

# 4

## 2D Soil structure interaction

To determine the influence of the soil on the super structure, a coupling between them needs to be established. The soil structure interaction is constructed in the frequency domain. There are multiple ways to couple a linear structure to the soil model derived in chapter 3. However, it is chosen to elaborate the coupling of an inextensible foundation strip based on the orthogonality of the structural modes. The orthogonality of the modes of the foundation are used to include the soil behaviour in the dynamic response of the combined system. Numerical integration is used to solve the coupled equations. The SSI between the soil and a simple Euler Bernoulli, i.e. a pure bending beam, due to a point-load on the beam is performed first. The beam is assumed to be inextensible, and therefore has a constant horizontal displacement. Therefore, the system in x direction is reduced to a single degree of freedom system. The applied force used in this chapter, is either a point load or an incident soil displacement field.

### 4.1. General equations of a free-edge Euler Bernoulli beam

In this chapter, a foundation strip is coupled to the soil. The behaviour of the foundation strip is chosen to be equal to an inextensible Euler Bernoulli beam. In this case, a concrete strip of one meter height and a length of 10 meters is used. On top of the beam at some point  $x_0$  a harmonic load or an incident harmonic displacement field of the soil is applied. The depth of the soil is chosen to be 25 meters. The case is shown in 4.1. For the SSI the interface is discretized in  $n$  single node elements with the node in the center of the element ( $n = L/b$ ). The material properties of the beam are summarized in table 4.1.

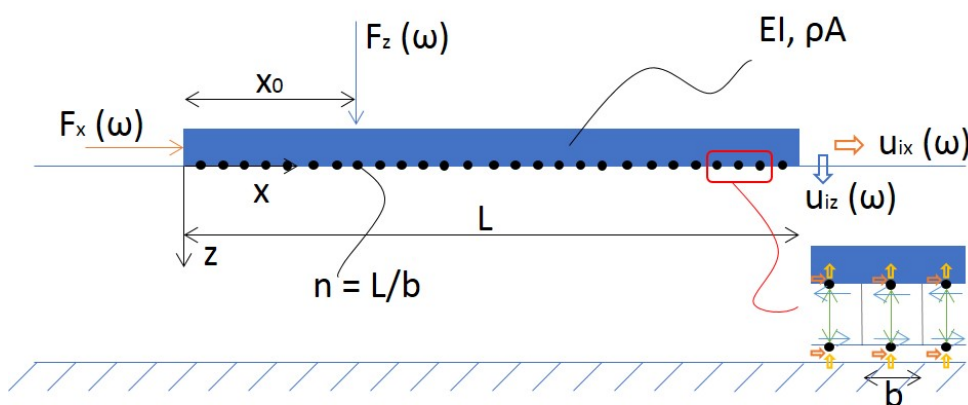


Figure 4.1: Schematisation of a finite beam supported on linear elastic soil

The governing equations of the SSI system for this case consist of the stiffness equation of the soil (Eq. (3.60)), the vertical and horizontal system equation of motion (Eq. (4.1) & Eq. (4.2)), the boundary condition of the foundation strip (Eq. (4.3) & Eq. (4.4)), the kinematic equilibrium of the displacement of the soil and founda-

Characteristic	Symbol	Value	Unit
Young's modulus	E	$30 * 10^9$	$N/m^2$
Second moment of area	I	$1/12$	$m^4$
Density	$\rho$	2407	$kg/m^3$

Table 4.1: Beam material properties

tion (Eq. (4.5)) and the assumption of an in-plane inextensible foundation strip (Eq. (4.6)).

$$EI \frac{d^4 \tilde{u}_{z,b}}{dx^4} - \omega^2 \rho_b A_b \tilde{u}_{z,b} + \tilde{S}_{z,s} = \tilde{F}_z \delta(x - x_0) \tilde{S}_{z,i} \quad (4.1)$$

$$- \omega^2 \rho_b A_b L_b \tilde{u}_{x,b} + \tilde{S}_{x,s} = \tilde{F}_x + \tilde{S}_{x,i} \quad (4.2)$$

$$\frac{d^2 \tilde{u}_{z,b}}{dx^2} \Big|_{x=0} = \frac{d^2 \tilde{u}_{z,b}}{dx^2} \Big|_{x=L} = 0 \quad (4.3)$$

$$\frac{d^3 \tilde{u}_{z,b}}{dx^3} \Big|_{x=0} = \frac{d^3 \tilde{u}_{z,b}}{dx^3} \Big|_{x=L} = 0 \quad (4.4)$$

$$u_{z,b} = u_{z,s}, \quad u_{x,b} = u_{x,s} \quad (4.5)$$

$$u_{x,b} = \text{constant for } 0 \leq x \leq L \quad (4.6)$$

$$(4.7)$$

Where  $\tilde{S}_{z,s}$  and  $\tilde{S}_{x,s}$  are respectively the vertical and horizontal interaction forces,  $\tilde{S}_{z,i}$  and  $\tilde{S}_{x,i}$  respectively the vertical and horizontal stresses due to an incident wave field and  $\tilde{F}_z$  and  $\tilde{F}_x$  are respectively vertical and horizontal harmonic point loads. The subscripts  $b$ ,  $s$  and  $i$  refer to the beam, soil and incident field respectively.

## 4.2. Homogeneous solution of a free-edge EB beam

The out-of-plane equation of motion, Eq. (4.1) of the beam is solved for by a summation over the modal displacements of the beam. To find these modal displacements, first the homogeneous equation of motion is solved, and therefore homogeneous boundaries are applied, i.e. no interaction with the soil and external loads ( $\tilde{S}_{i,z,s} = \tilde{S}_{z,s} = \tilde{F}_z = 0$ ). Eq. (4.1) is rewritten after the substitution of  $\lambda$  as:

$$\begin{aligned} EI \frac{d^4 \tilde{u}_{z,b}}{dx^4} - \omega^2 \rho_b A_b \tilde{u}_{z,b} &= 0 \\ \frac{d^4 \tilde{u}_{z,b}}{dx^4} - \frac{\omega^2 \rho_b A_b}{EI} \tilde{u}_{z,b} &= 0 \\ \frac{d^4 \tilde{u}_{z,b}}{dx^4} - \lambda^4 \tilde{u}_{z,b} &= 0 \\ \lambda^4 &= \frac{\omega^2 \rho_b A_b}{EI} \end{aligned} \quad (4.8)$$

The general solution of  $\tilde{u}_{z,b}$  in Eq. (4.8) is a combination of both positive and negative, both real and imaginary exponents times unknowns which may be rewritten as.

$$\begin{aligned} \tilde{u}_{z,b} &= A e^{\lambda x} + B e^{-\lambda x} + C e^{i\lambda x} + D e^{-i\lambda x} \\ \tilde{u}_{z,b} &= A_1 \sin(\lambda x) + A_2 \cos(\lambda x) + A_3 \sinh(\lambda x) + A_4 \cosh(\lambda x) \end{aligned} \quad (4.9)$$

By Applying the boundary conditions (Eq. (4.2) and Eq. (4.3)) at  $x = 0$  it results that:

$$A_3 = A_1, \quad A_4 = A_2 \quad (4.10)$$

The boundary conditions at  $x = L$  results in two homogeneous equations with two unknowns:

$$\begin{bmatrix} -\sin(\lambda L) + \sinh(\lambda L) & -\cos(\lambda L) + \cosh(\lambda L) \\ -\cos(\lambda L) + \cosh(\lambda L) & \sin(\lambda L) + \sinh(\lambda L) \end{bmatrix} \begin{bmatrix} A_1 \\ A_2 \end{bmatrix} = \begin{bmatrix} 0 \\ 0 \end{bmatrix} \quad (4.11)$$

This matrix is solved by setting the determinant of the matrix to zero. This leads to:

$$\cos(\lambda L) \cosh(\lambda L) = 1 \quad (4.12)$$

Since the length of the beam is unequal to 0, the equation is solved for an infinite amount of wavenumbers  $\lambda_m$ . The wavenumbers correspond to modal shapes  $\phi_m$ , which can be found by solving Eq. (4.11) for  $A_2$ , leaving one unknown, and substituting the wavenumbers  $\lambda_m$ .

$$\begin{aligned} \phi_m &= \frac{1}{\cos(\lambda_m L) - \cosh(\lambda_m L)} (-\sinh(\lambda_m x) - \sin(\lambda_m x)) \cosh(\lambda_m L) \\ &\quad + (\sin(\lambda_m x) + \sinh(\lambda_m x)) \cos(\lambda_m L) + (\cos(\lambda_m x) + \cosh(\lambda_m x)) (-\sin(\lambda_m L) + \sinh(\lambda_m L)) \end{aligned} \quad (4.13)$$

$$\tilde{u}_{z,b} = \sum_m A_m \phi_m \quad (4.14)$$

The eigenfrequencies corresponding to the modes are found from the substitution of  $\lambda$  done in Eq. (4.8).

$$\lambda_m^4 = \frac{\omega_m^2 \rho_b A_b}{EI}, \quad \omega_m = \lambda_m^2 \sqrt{\frac{EI}{\rho_b A_b}} \quad (4.15)$$

The first two beam modes correspond to the rigid body modes of the beam ( $\omega_m = 0$ ). All uneven modes are symmetric and all even modes asymmetric. The first 5 modes shapes for both the displacement and its 4<sup>th</sup> spatial derivative are shown in 4.2. The rigid body modes do not influence the spatial derivatives of the mode shapes, since there is no deformation of the beam.

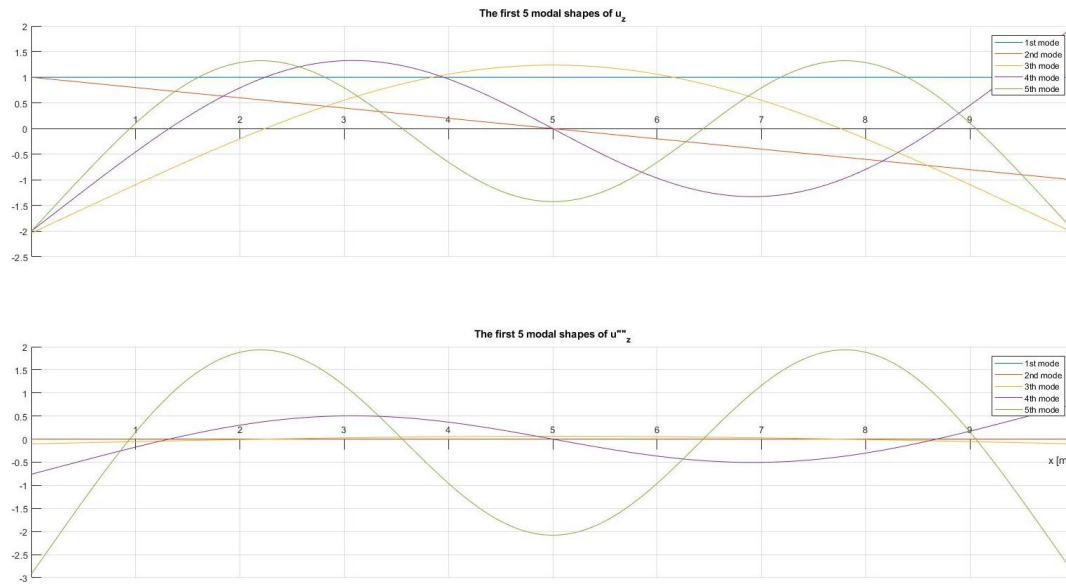


Figure 4.2: First 5 beam mode shapes

### 4.3. Soil stiffness matrix decomposition

The frequency-dependent stiffness matrix found in Eq. (3.59), corresponds to full matrix, depending both on the horizontal and vertical forces and displacements. The dimensions of the stiffness-matrices are given in-between the square brackets, to clarify how the stiffness matrix is modified.

$$\begin{bmatrix} \tilde{S}_{x1} \\ \vdots \\ \tilde{S}_{xn} \\ \tilde{S}_{z1} \\ \vdots \\ \tilde{S}_{zn} \end{bmatrix} = \begin{bmatrix} \tilde{\mathbf{K}}_{xx,[n,n]} \\ \tilde{\mathbf{K}}_{xz,[n,n]} \end{bmatrix} \begin{bmatrix} \tilde{\mathbf{K}}_{zx,[n,n]} \\ \tilde{\mathbf{K}}_{zz,[n,n]} \end{bmatrix} \begin{bmatrix} \tilde{u}_{x1} \\ \vdots \\ \tilde{u}_{xn} \\ \tilde{u}_{z1} \\ \vdots \\ \tilde{u}_{zn} \end{bmatrix} \quad (4.16)$$

The forces due to the incident wave field are derived directly from Eq. (4.16). Due to the assumption of an infinite stiff in-plane foundation strip in Eq. (4.6), the horizontal system of the foundation are reduced from an continuum system to an SDOF system. Therefore, the displacements in  $x$  are all equal and the forces in  $x$  can be summed:

$$\begin{aligned} \tilde{S}_{x,i} &= \sum_{j=1}^n \tilde{S}_{xj,i} \\ \tilde{S}_{x,s} &= \sum_{j=1}^n \tilde{S}_{xj,s} \\ \tilde{u}_{x1,s} &= \tilde{u}_{x2,s} = \tilde{u}_{xn,s} = \tilde{u}_{x,s} \end{aligned} \quad (4.17)$$

The stiffness matrix of the soil coupled to the foundation is split and reduced in size by making use of Eq. (4.17):

$$\begin{aligned} \tilde{S}_{x,s} &= \tilde{\mathbf{K}}_{xx,[1,1]} \tilde{u}_{x,s} + \begin{bmatrix} \tilde{\mathbf{K}}_{zx,[1,n]} \end{bmatrix} \begin{bmatrix} \tilde{u}_{z1,s} \\ \vdots \\ \tilde{u}_{zn,s} \end{bmatrix} \Rightarrow \tilde{S}_{x,s} = \tilde{\mathbf{K}}_{xx} \tilde{u}_{x,s} + \tilde{\mathbf{K}}_{zx} \tilde{\mathbf{u}}_{z,s} \\ \begin{bmatrix} \tilde{S}_{z1,s} \\ \vdots \\ \tilde{S}_{zn,s} \end{bmatrix} &= \begin{bmatrix} \tilde{\mathbf{K}}_{xz,[n,1]} \end{bmatrix} \tilde{u}_{x,s} + \begin{bmatrix} \tilde{\mathbf{K}}_{zz,[n,n]} \end{bmatrix} \begin{bmatrix} \tilde{u}_{z1,s} \\ \vdots \\ \tilde{u}_{zn,s} \end{bmatrix} \Rightarrow \tilde{\mathbf{S}}_{z,s} = \tilde{\mathbf{K}}_{xz} \tilde{u}_{x,s} + \tilde{\mathbf{K}}_{zz} \tilde{\mathbf{u}}_{z,s} \end{aligned} \quad (4.18)$$

Eq. (4.18) is substituted in the horizontal equation of motion from Eq. (4.2), to express the horizontal rigid body motion into the vertical displacements and external forces. The substitution of the horizontal interaction force results in:

$$-\omega^2 \rho_b A_b L_b \tilde{u}_{x,b} + \tilde{\mathbf{K}}_{xx} \tilde{u}_{x,s} + \tilde{\mathbf{K}}_{zx} \tilde{\mathbf{u}}_{z,s} = \tilde{F}_x + \tilde{S}_{x,i} \quad (4.19)$$

Since  $\tilde{u}_{x,s} = \tilde{u}_{x,b}$ , the horizontal displacement is separated and expressed in terms of the vertical displacement and external forces.

$$\tilde{u}_{x,s} = \frac{\tilde{F}_x + \tilde{S}_{x,i}}{\tilde{\mathbf{K}}_{xx} - \omega^2 \rho_b A_b L_b} - \frac{\tilde{\mathbf{K}}_{zx} \tilde{\mathbf{u}}_{z,s}}{\tilde{\mathbf{K}}_{xx} - \omega^2 \rho_b A_b L_b} \quad (4.20)$$

By substituting Eq. (4.20) into the second equation of motion Eq. (4.18), the vertical interaction forces are found independent of the horizontal displacement and interaction forces, but only depend on the external load and vertical displacement.

$$\begin{aligned} \tilde{\mathbf{S}}_{z,s} &= \tilde{\mathbf{K}}_{xz} \left( \frac{\tilde{F}_x + \tilde{S}_{x,i}}{\tilde{\mathbf{K}}_{xx} - \omega^2 \rho_b A_b L_b} - \frac{\tilde{\mathbf{K}}_{zx} \tilde{\mathbf{u}}_{z,s}}{\tilde{\mathbf{K}}_{xx} - \omega^2 \rho_b A_b L_b} \right) + \tilde{\mathbf{K}}_{zz} \tilde{\mathbf{u}}_{z,s} \\ &= \left( \tilde{\mathbf{K}}_{xz} - \frac{\tilde{\mathbf{K}}_{xz} \tilde{\mathbf{K}}_{zx}}{\tilde{\mathbf{K}}_{xx} - \omega^2 \rho_b A_b L_b} \right) \tilde{\mathbf{u}}_{z,s} + \frac{\tilde{\mathbf{K}}_{xz}}{\tilde{\mathbf{K}}_{xx} - \omega^2 \rho_b A_b L_b} (\tilde{F}_x + \tilde{S}_{x,i}) \\ &= \tilde{\mathbf{K}}_{z-u_z} \tilde{\mathbf{u}}_{z,s} + \tilde{\mathbf{C}}_x (\tilde{F}_x + \tilde{S}_{x,i}) \end{aligned} \quad (4.21)$$

Where the matrix  $\tilde{\mathbf{K}}_{z-u_z}$  and vector  $\tilde{\mathbf{C}}_x$  represent respectively the effective vertical stiffness of the soil and the vertical displacement due to horizontal forcing.

$$\tilde{\mathbf{K}}_{z-u_z} = \left( \tilde{\mathbf{K}}_{zz} - \frac{\tilde{\mathbf{K}}_{xz}\tilde{\mathbf{K}}_{zx}}{\tilde{\mathbf{K}}_{xx} - \omega^2 \rho_b A_b L_b} \right) \quad \& \quad \tilde{\mathbf{C}}_x = \frac{\tilde{\mathbf{K}}_{xz}}{\tilde{\mathbf{K}}_{xx} - \omega^2 \rho_b A_b L_b} \quad (4.22)$$

By substituting Eq. (4.21), the vertical system equation of motion, Eq. (4.1) is independent from the horizontal displacement and can be solved by making use of the orthogonality principle.

#### 4.4. The orthogonality principle

To solve the system equation of motion, the principle of orthogonality is used. A condition of modes is that they are orthogonal to each other, which is checked for all modes derived in Eq. (4.13). For normalized modes of a 2D beam, it holds that the multiplication of two different modes result in a zero solution and two the same modes results in length integrating over:

$$\int_0^L \phi_l(x)\phi_m(x)dx = L\delta_{ml} \quad (4.23)$$

The orthogonality of modes is applied on Eq. (4.1) to solve the dynamic SSI. First Eq. (4.14) and Eq. (4.21) are substituted in Eq. (4.1). This results in the SSI dynamic equation of motion, expressed in a summation of modal shapes. Since the stiffness matrix of the soil is discretized and the modal shapes of the beam are continuous, the same discretization is applied on the modal shapes  $\phi$  of the beam. The single node elements, with size  $b$  equal to the soil boundary elements is used, resulting in the same size vectors. All external force components are put on the right-hand side in the system equation of motion.

$$\begin{aligned} \sum_m A_m \left[ \lambda_m^4 EI \phi_m \frac{\rho_b A_b}{\rho_b A_b} - \omega^2 \rho_b A_b \phi_m + \tilde{\mathbf{K}}_{z-u_z} \phi_m \right] + \tilde{\mathbf{C}}_x (\tilde{F}_x + \tilde{S}_{x,i}) &= \tilde{F}_z \delta(x-x_0) + \tilde{\mathbf{S}}_{z,i} \\ \sum_m A_m [(\omega_m^2 - \omega^2) \rho_b A_b \phi_m + \tilde{\mathbf{K}}_{z-u_z} \phi_m] &= \tilde{F}_z \delta(x-x_0) + \tilde{\mathbf{S}}_{z,i} - \tilde{\mathbf{C}}_x (\tilde{F}_x + \tilde{S}_{x,i}) \end{aligned} \quad (4.24)$$

Where  $\delta_{ml}$  is the Kronecker delta function. The orthogonality is applied by multiplying Eq. (4.24) with another mode  $l$  and integrating over the length. This results in an infinite number of non-homogeneous equations, with an equal amount of unknowns  $A_m$ , which describe the amplification of each mode.

$$\sum_m A_m \int_0^L [(\omega_m^2 - \omega^2) \rho_b A_b \phi_l \cdot \phi_m + \phi_l \cdot \tilde{\mathbf{K}}_{z-u_z} \phi_m] = \phi_l \cdot (\tilde{F}_z \delta(x-x_0) + \tilde{\mathbf{S}}_{z,i} - \tilde{\mathbf{C}}_x (\tilde{F}_x + \tilde{S}_{x,i})) dx \quad (4.25)$$

To solve Eq. (4.25), numerical integration is used by summation over the indices of the vectors. By making use of the characteristics of the modes from Eq. (4.23), the properties of the Dirac delta and Kronecker delta function Eq. (4.25) results in:

$$\begin{aligned} \sum_m A_m [(\omega_m^2 - \omega^2) \rho_b A_b b \phi_m^T \phi_m \delta_{lm} + \phi_l^T \tilde{\mathbf{K}}_{z-u_z} \phi_m] &= \phi_l(x_0) \tilde{F}_z + \phi_l^T \tilde{\mathbf{S}}_{z,i} - \phi_l^T \tilde{\mathbf{C}}_x (\tilde{F}_x + \tilde{S}_{x,i}) \\ \sum_m A_m [(\omega_m^2 - \omega^2) \rho_b A_b L b \delta_{lm} + \phi_l^T \tilde{\mathbf{K}}_{z-u_z} \phi_m] &= \phi_l(x_0) \tilde{F}_z + \phi_l^T \tilde{\mathbf{S}}_{z,i} - \phi_l^T \tilde{\mathbf{C}}_x (\tilde{F}_x + \tilde{S}_{x,i}) \end{aligned} \quad (4.26)$$

Calling the equation between the square brackets  $M$  and the right-hand side  $F$ , Eq. (4.26) has  $m-1$  unknowns  $A_m$ , but since there are an equal number of modes  $l$  and  $m$  considered,  $M$  results in a square matrix. By taking the inverse, the unknowns are found for every discrete number of modes considered:

$$\begin{aligned} \mathbf{M}_{ml} \mathbf{A}_m &= \tilde{F}_l \\ \mathbf{A}_m &= \mathbf{M}_{ml}^{-1} \tilde{F}_l \end{aligned} \quad (4.27)$$

The total vertical displacement is found by substituting Eq. (4.27) in Eq. (4.14). From the vertical displacement and external forces, the horizontal displacement is found by Eq. (4.20) and the vertical interaction forces from Eq. (4.21).

## 4.5. 2D SSI case study

Three analysis are performed for three different frequencies, 0.77, 3.09 and 19.30 Hz to observe how the model behaves. For all cases the convergence is discussed. The frequencies are chosen such that the first frequency is a rather low frequency in absence of any propagating waves, the second frequency includes propagating waves and is commonly expected during an earthquake, the third frequency is a relatively high frequency during an earthquakes. This section shows results of load cases in terms of the displacements of both the beam and the soil. It shows how both foundation and soil influence each other. Furthermore, for frequency 3.09 Hz, the interaction stresses and moment- and shear-line of the foundation are shown. The length and height of the beam considered are respectively 10 and 1 meter. Further material properties of the beam are described in table 4.1. The first 20 natural frequencies corresponding to the free-edged beam considered are derived from Eq. (4.15) and shown in table 4.2. The first two beam modes are related to the rigid body

Mode nr.	Hz	Mode nr.	Hz
1	0	11	1445
2	0	12	1765
3	36	13	2117
4	100	14	2501
5	196	15	2918
6	324	16	3366
7	484	17	3846
8	676	18	4358
9	900	19	4903
10	1157	20	5479

Table 4.2: First 20 free-free beam natural frequencies

displacements of the beam (rocking and uniform displacement). Due to the stiffness of the beam, the third beam mode is already larger than the frequencies occurring in an earthquake. Therefore, it is expected that mainly the rigid body motions and the first deflection mode will be dominant in all load cases. The three load cases considered are: first, a point load of 1 kN at  $x_0 = L/3$ , second, a uniform vertical incident wave field and third, a incident propagating (Rayleigh) wave. The response to the three cases are discussed separately.

### Point load

The first load case considered is a harmonic point of 1 kN load at  $x = L/3$ . The point load is asymmetric, and therefore both symmetric and asymmetric beam modes are triggered. Figure 4.3 shows the vertical displacement of both beam and soil, the vertical interaction stresses between the beam and soil and the moment & shear line of the beam due to the point load. The largest interaction stresses are found at the edge of the foundation, what is expected due to load spreading effects of a rather stiff foundation. The largest moment and shear force are obviously located at the place where the point load is applied. Both moment and shear force are zero at the edge of the beam, and therefore fulfil the boundary conditions. Although 100 beam modes are used to describe the deformation of the beam. More are needed to describe shear-force smoothly, in case of a point load. For three frequencies, the vertical and horizontal displacement of the beam and soil due to a point load are shown in figure 4.6. The vertical displacement at 0.77 Hz is in phase with the load, while due to the soil properties, the higher frequencies have a clear phase difference. The horizontal displacement of the beam is only little due to the asymmetric load.

### Incident uniform vertical displacement

The second load case is based on a uniform vertical incident displacement of the soil. The uniform displacement is symmetric, and therefore only symmetric modes are triggered. The interaction stresses, moment- and shear-line are also symmetric, shown in figure 4.4. The amplitude of the incident uniform displacement is  $10^{-3}$ m. Figure 4.7 shows the vertical and horizontal displacement field for the three frequencies. At 0.77 Hz, the displacement almost matches the incident wave field and the imaginary displacement is zero. Therefore, the system has no damping, what is reasonable since the frequency is to low for propagating waves to exist. The two other frequencies show a clear difference between the incident and reaction wave field. The inertial interaction of the beam cause propagating waves, and therefore energy propagates away from the beam.

### Incident propagating wave

The incident propagating wave contains a coupled vertical and horizontal motion. The motion is asymmetric, and therefore both symmetric and asymmetric beam modes are activated. The interaction stresses, moment and shear-force along the beam changes with the phase of the load but always fulfil the boundary conditions. The beam follows the displacement of the soil respectively good at 0.77 Hz and 3.09 Hz as shown in figure 4.8. However, at 19.30 Hz, the kinematic SSI has great influence. The beam is too stiff to match the incident wave of the soil. Therefore, the wave field changes significantly due to the presence of the foundation on both left and right side of the soil.

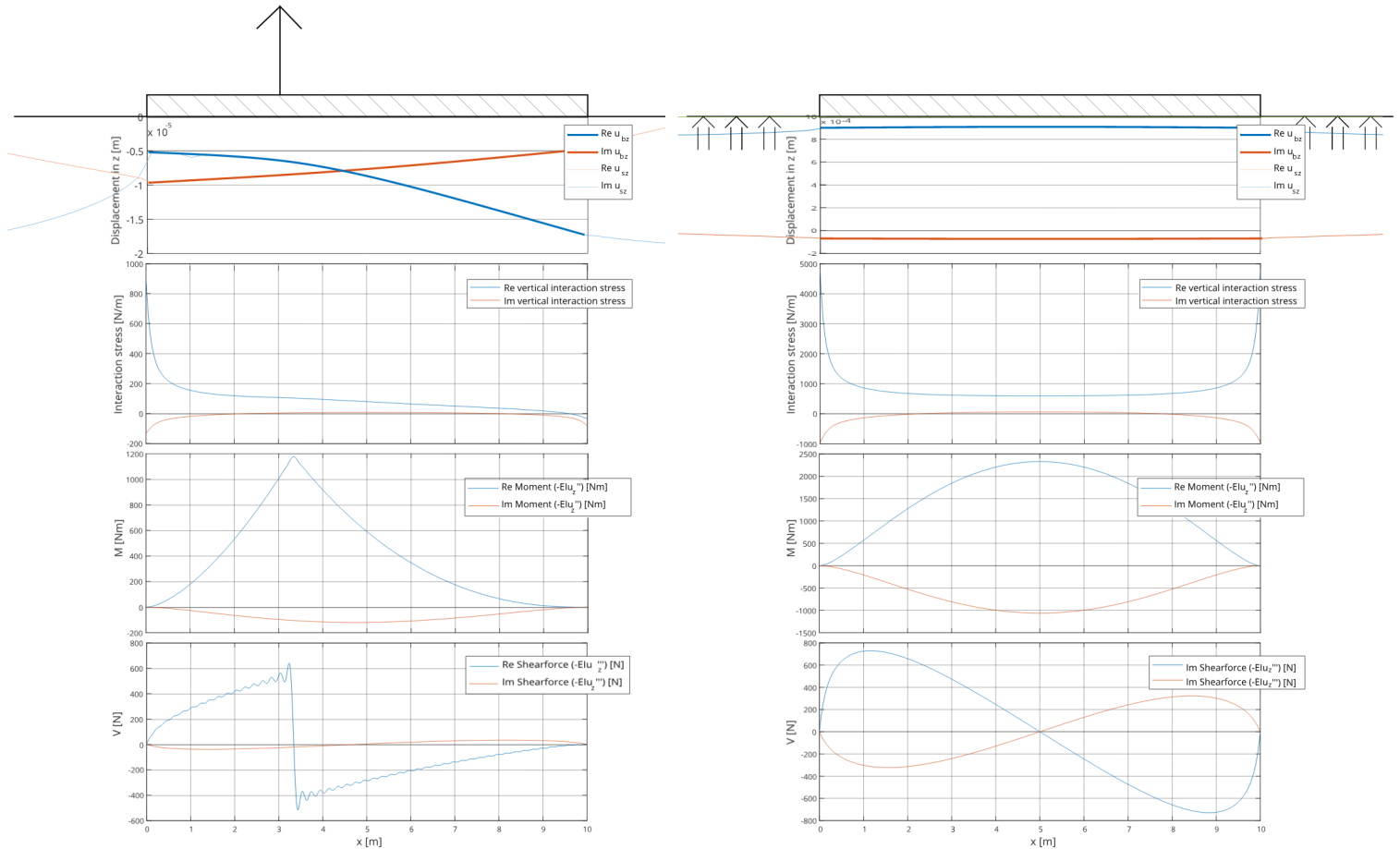


Figure 4.3: Deformation, interaction stress, moment and shear line of the strip, excited by a harmonic point load ( $f = 3.09$  Hz).  
 Figure 4.4: Deformation, interaction stress, moment and shear line of the strip, excited by an incident uniform displacement ( $f = 3.09$  Hz).

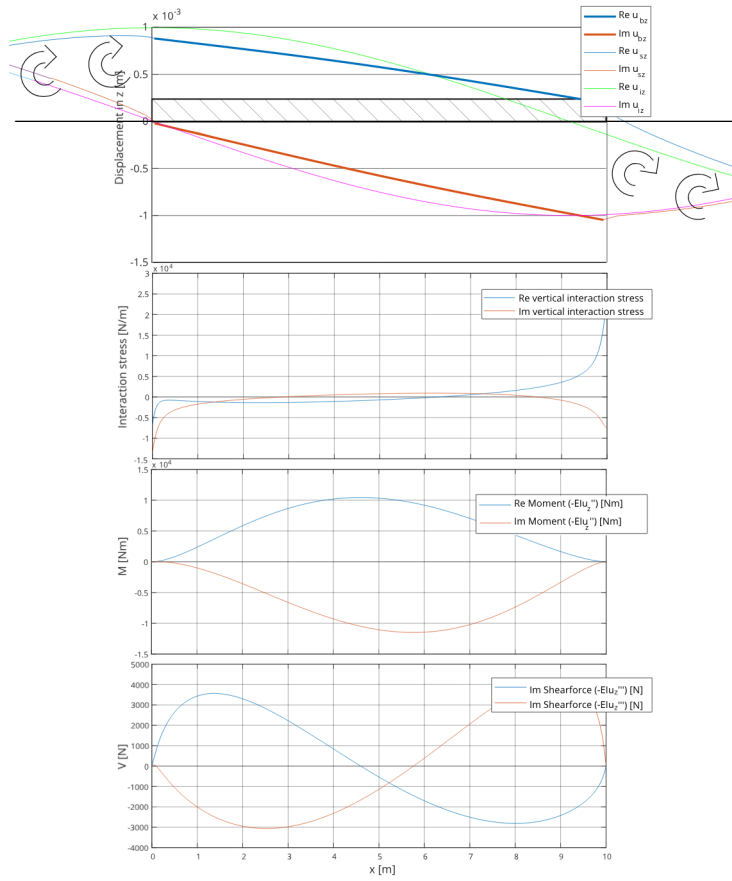


Figure 4.5: Deformation, interaction stress, moment and shear line of the strip, excited by a propagating wave ( $f = 3.09$  Hz).

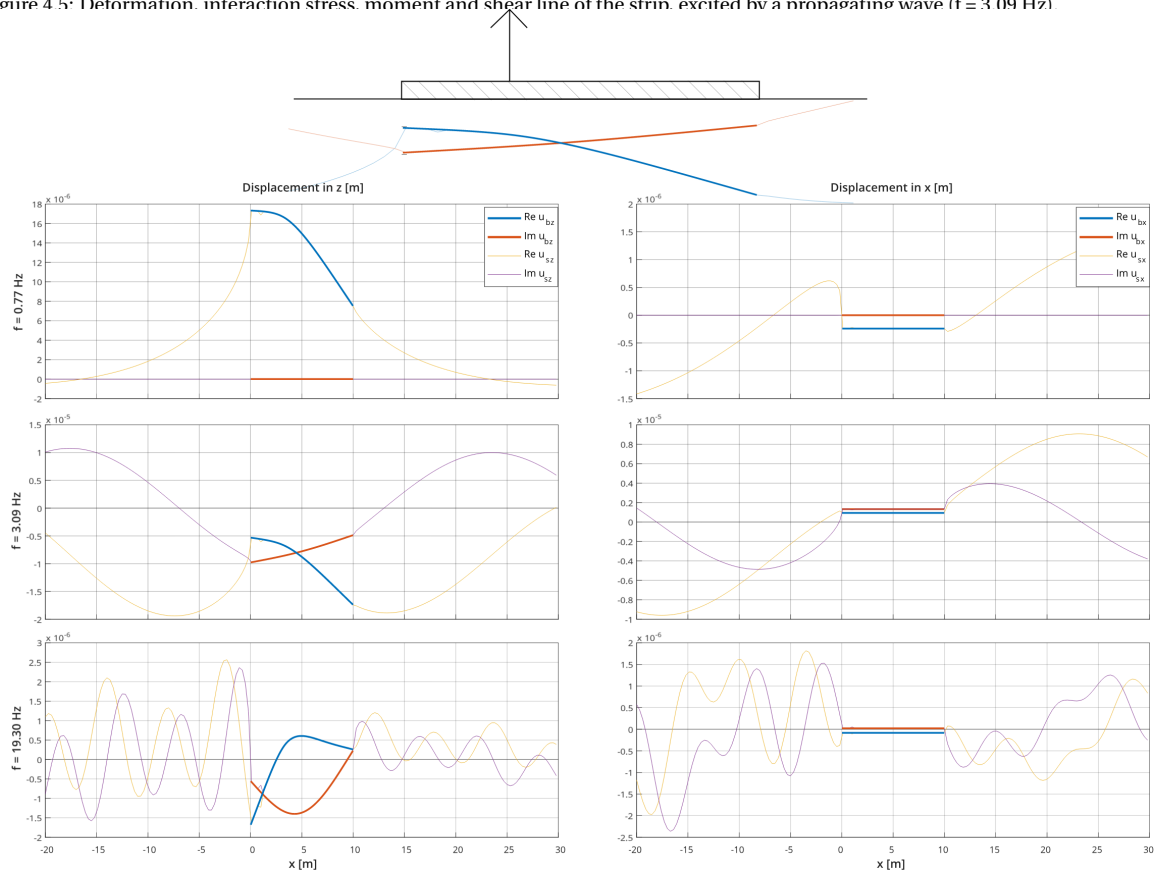


Figure 4.6: Displacement of strip and surrounding, excited with a harmonic point load ( $f = 0.77$  Hz, 3.09 Hz & 19.30 Hz).

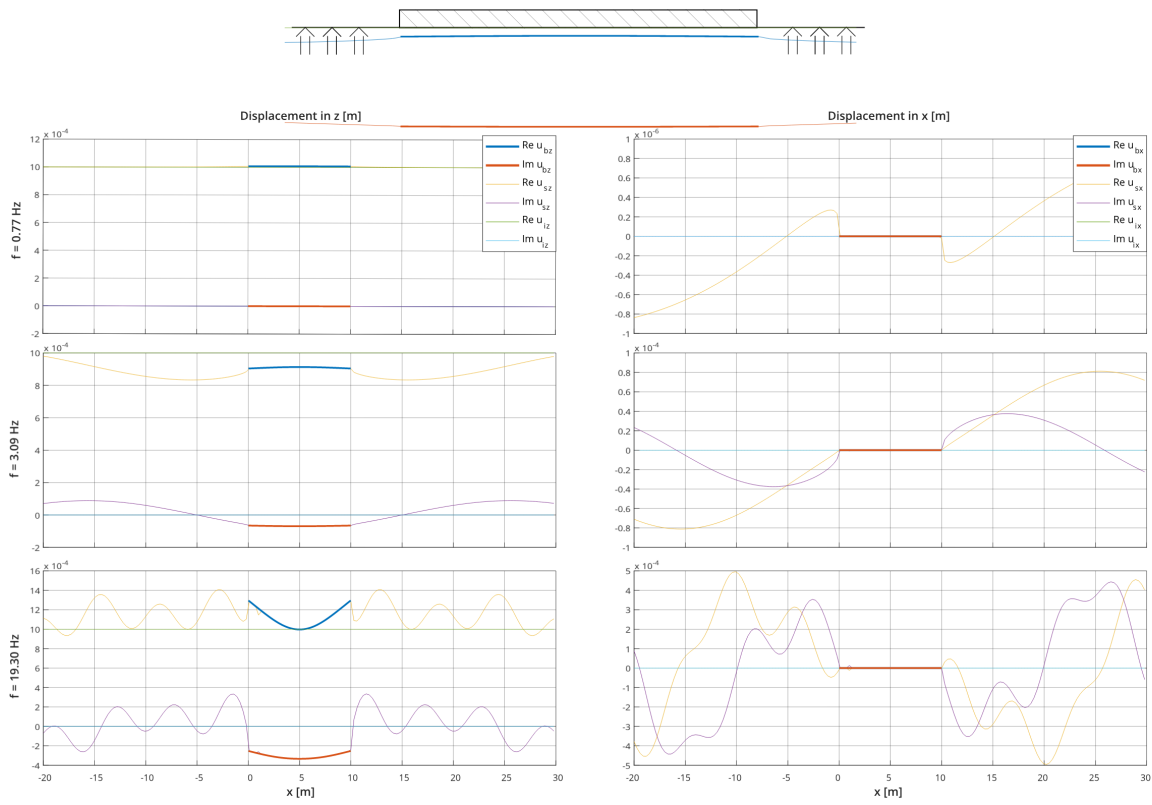


Figure 4.7: Displacement of strip and surrounding, excited with an incident uniform displacement field ( $f = 0.77$  Hz, 3.09 Hz & 19.30 Hz).

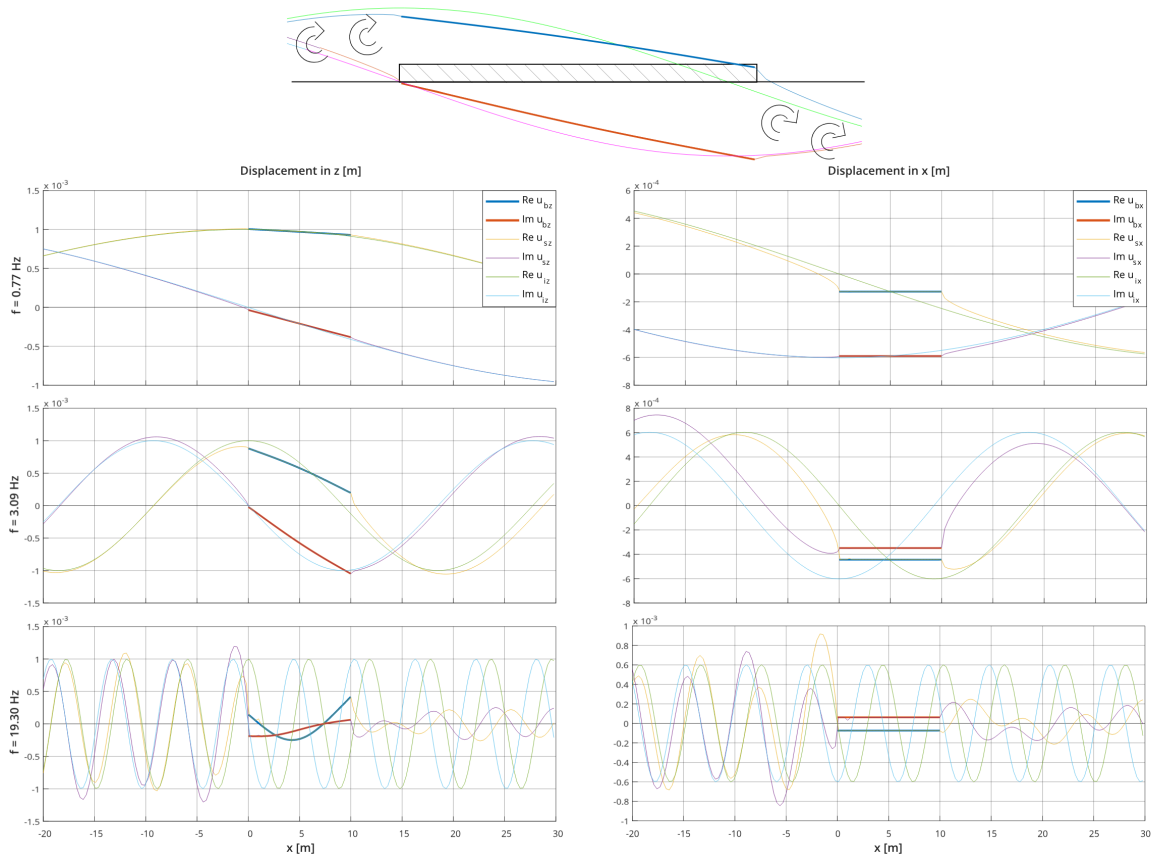


Figure 4.8: Displacement of strip and surrounding, excited with an incident propagating wave ( $f = 0.77$  Hz, 3.09 Hz & 19.30 Hz).

## 4.6. Convergence of the 2D model

The convergence of the model depends mainly on the number of elements, beam modes and soil modes included. For the three cases from section 4.5 the convergence is observed. To check the influence of the number of beam and soil modes included, a reference run is done with 110 beam modes and 220 soil modes. The error with respect to the reference run is calculated by:

$$\text{Error} = \frac{|u_{z,b_i} - u_{z,b_r,z}|}{|u_{z,b_r}|} \quad (4.28)$$

In which  $r$  denotes the reference run.

### Number of elements

The starting point for the number of elements included, is that there are at least 6 elements needed to describe a full sinus (Wolf, 1985). Therefore, the model has a minimum of 3 elements per beam mode, because the first flexible beam mode shape corresponds to a half sinus, the second to a full sinus etc. From numerical test, it results that this assumption is sufficient in almost all cases, only when few beam modes and many soil modes are included, this starting point does not hold any more. This is validated by taking the difference in displacement of the beam compared to a case with 10 additional elements. When the results differ less than 0.1%, the number of elements was assumed sufficient. For frequencies significantly smaller than the first ten eigenfrequencies of the structure, making use 100-300 elements will be sufficient for the SSI, since it is expected that the beam will mainly deform in the first few modal shapes.

### Number of beam modes

The number of beam modes that influence the SSI outcome is expected to be little. Figure 4.9 confirms that expectation, since the outcome converges already after 5 to 10 beam modes in both cases of a point load and uniform incident displacement field. Convergence of the modes, has little dependence of the range of frequencies used in this case, but is influenced by the load type strongly (local or uniform). The displacement of the beam is described by its first four modal shapes for more than 95%, in all load cases. Generally, the higher modes are activated by local loads only for the range of frequencies considered. To describe the response of uniform or smooth load cases, including a few beam modes seems to be sufficient.

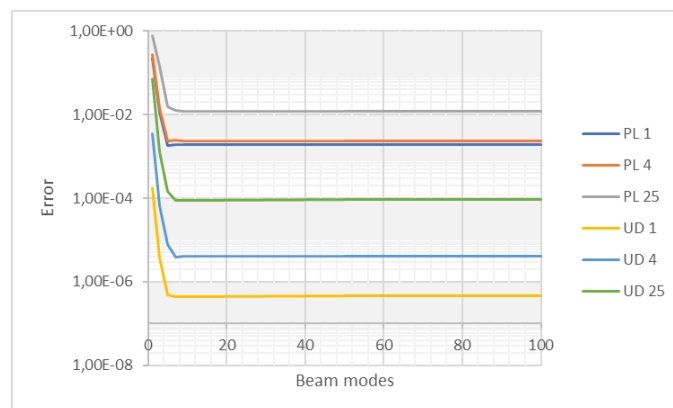


Figure 4.9: Influence of the number of included beam modes on SSI analysis for a point load (PL) and uniform displacement (UD) for the normalized frequencies 1, 4 and 25, 200 soil modes are included.

### Number of soil modes

The SSI analysis is more sensitive to the number of soil modes included. Figure 4.10 indicates that even a high number of complex soil modes do still contribute to the SSI analysis, although the convergence is logarithmic. Including 100 beam modes should be sufficient since the results differ less than 1% with respect to the reference case, except for the case of a high frequency point load. It appears that the number of soil modes that need to be included to reach convergence is dependent on frequency and type of load case. However, in earthquake engineering local forces are not expected and the higher frequency included does almost not occur during an earthquake, including 100 soil modes will lead to a solution within 1 % of the exact solution.

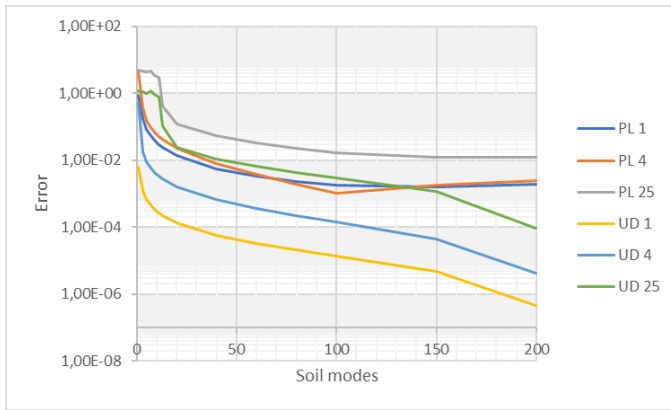


Figure 4.10: Influence of the number of included soil modes on SSI analysis for a point load (PL) and uniform displacement (UD) for the normalized frequencies 1, 4 and 25, 100 beam modes are included

### 4.7. Influence of the foundation stiffness

The stiffness of the SSI system depends on both soil and structure stiffness. The stiffness of the foundation influences the stress profile acting on the soil. A complete flexible foundation will transfer the load on top of the strip, directly to soil. However, the interaction stress of a rigid strip differs to an applied stress on top of the strip. For symmetrical loads, the distribution of the interaction stress will be the largest at the edge and the smallest in the center due to load spreading effects. Figure 4.12 illustrates the influence of a flexible foundation on the load spreading effects. Figure 4.12 also illustrates that the static stiffness of the soil

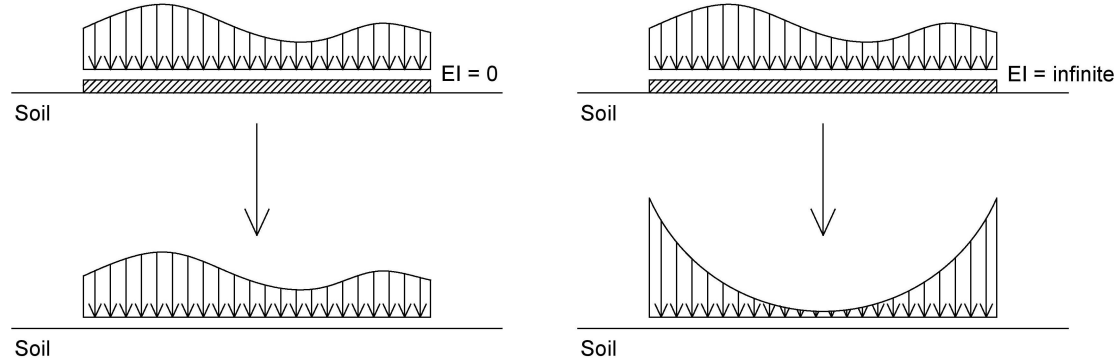


Figure 4.11: Redistribution of stresses due to a rigid strip

fluctuates over the interaction area. For both flexible and rigid strips, the soil stiffness is the largest at the edges since the stress-displacement ratio is the largest.

To give a normalized value to the stiffness of the foundation, the relative flexibility formulation of Gazetas (1983) is used:

$$RF = \frac{E_b}{E_s} \left( \frac{t_b}{a} \right)^3 (1 - \nu_b^2) \quad (4.29)$$

For different relative flexibility ratios, the system stiffness and damping are determined with respect to the rigid strip foundation from section 3.7. Only the kinematic interaction is evaluated. Therefore, inertial forces are neglected since the mass will add force but should not affect the stiffness, i.e. the mass of the strip is set equal to zero. Only the vertical and rocking stiffness and damping are evaluated. The system equation of motion, Eq. (4.24) turns into:

$$\sum_m A_m [E_b I_b \lambda_m^4 L_b \delta_{lm} + \boldsymbol{\phi}_l^T \mathbf{K}_{z-u_z} \boldsymbol{\phi}_m] = \phi_l(x_0) \tilde{F}_z(\omega) + \boldsymbol{\phi}_l^T \tilde{\mathbf{S}}_{i_z n, s} \quad (4.30)$$

The rigid foundation is approached as a single degree of freedom system, stiffness and damping do not vary over the width of the foundation. This does not hold for a flexible foundation. The stiffness of the flexible foundation is evaluated by the average displacement, center displacement and edge displacement. Figure 4.12 shows how the complex stiffness is obtained. The damping is obtained by taking the imaginary part of the stiffness. The stiffness and damping of the system turn out to be almost independent on the frequencies. Therefore, the stiffness and damping are averaged over the frequencies  $0 \leq a_0 \leq 1$  for ratios  $\frac{h}{a} = 4$  and  $\frac{h}{a} = 25$ . Table 4.3 and table 4.4 show the differences in stiffness and damping for both ratios. The influence of the flexibility of the beam is only little for ratio  $\frac{h}{a} = 25$ . Only fully flexible beams, e.g. without stiffness show significant reductions in stiffness. Furthermore, the stiffness and damping increase at the edge of a flexible plate and decrease in the center with respect to the average stiffness and damping. This is expected due to stress distribution patterns as aforementioned. The small influence are declared by the large depth width ratio, since the soil stiffness will be dominant in the stiffness of the SSI system for all cases.

The variation of stiffness and damping is larger for ratio  $\frac{h}{a} = 4$ . The rocking stiffness and damping are more sensitive to the flexibility of the plate than the vertical. The reduction average reduction of the vertical and rocking stiffness is respectively 5% and 20%. The reduction in damping is even larger with respectively 15% and 35%.

The system stiffness differs more along the width of the strip for flexible foundation strips. The vertical and

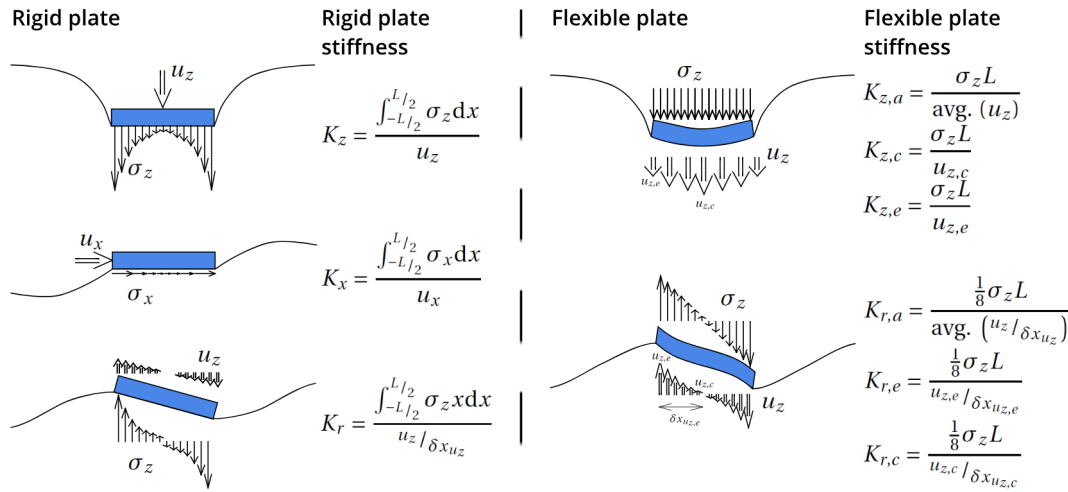


Figure 4.12: Derivation of the SSI stiffness including a rigid and flexible foundation

rocking system stiffness can reduce in the center of the strip with respectively 10% and 30% and increase at the edges with 20% and 25%. The damping is even more sensitive to the stiffness of the plate.

From these results, it concludes that the flexibility of the foundation is important for determining both the stiffness and damping of the SSI. Furthermore, the flexibility of the foundation influences the stress distribution between soil and foundation. In case of a relatively stiff foundation strip, the system reduces to a system with one rotational, vertical and horizontal spring, explained in section 2.3, but for more flexible foundations this assumption is not valid any more due to the large variation along the interaction plane.

RF	Averaged $k_a$		Averaged $c_a$		Center $k_c$		Center $c_c$		Edge $k_e$		Edge $c_e$	
	$k_z$	$k_r$	$c_z$	$c_r$	$k_z$	$k_r$	$c_z$	$c_r$	$k_z$	$k_r$	$c_z$	$c_r$
<b>0</b>	-5%	-20%	-14%	-36%	-13%	-32%	-21%	-71%	18%	24%	27%	13%
<b>0,001</b>	-5%	-15%	-15%	-28%	-12%	-27%	15%	-58%	12%	13%	15%	25%
<b>0,01</b>	-4%	-4%	-12%	-10%	7%	-10%	16%	-24%	7%	5%	16%	14%
<b>0,1</b>	-1%	1%	-4%	0%	2%	0%	6%	-2%	2%	2%	6%	3%
<b>1</b>	0%	2%	0%	1%	0%	2%	1%	1%	0%	2%	1%	2%
<b>10</b>	0%	2%	0%	2%	0%	2%	0%	2%	0%	2%	0%	2%
<b>100</b>	0%	2%	0%	2%	0%	2%	0%	2%	0%	2%	0%	2%

Table 4.3: Relative SSI stiffness and damping for a strip over a single layer on bedrock ( $\frac{h}{a} = 4$ )

RF	Averaged $k_a$		Averaged $c_a$		Center $k_c$		Center $c_c$		Edge $k_e$		Edge $c_e$	
	$k_z$	$k_r$	$c_z$	$c_r$	$k_z$	$k_r$	$c_z$	$c_r$	$k_z$	$k_r$	$c_z$	$c_r$
<b>0</b>	-1%	-18%	9%	-33%	3%	-30%	-3%	-56%	-30%	26%	46%	52%
<b>0,001</b>	0%	1%	-1%	-6%	-1%	1%	2%	-7%	-1%	1%	2%	-5%
<b>0,01</b>	0%	1%	0%	-6%	0%	1%	0%	-6%	0%	1%	0%	-6%
<b>0,1</b>	0%	1%	0%	-5%	0%	1%	0%	-6%	0%	1%	0%	-6%
<b>1</b>	0%	1%	0%	-6%	0%	1%	0%	-6%	0%	1%	0%	-6%
<b>10</b>	0%	1%	0%	-6%	0%	1%	0%	-6%	0%	1%	0%	-6%
<b>100</b>	0%	1%	0%	-6%	0%	1%	0%	-6%	0%	1%	0%	-6%

Table 4.4: Relative SSI stiffness and damping for a strip over a single layer on bedrock ( $\frac{h}{a} = 25$ )



# 5

## 3D model soil model

This chapter considers the derivation, which describes the response of a dynamically loaded 3D soil model on the surface in cylindrical coordinates. A cylindrical area is loaded with a harmonic force and the displacements at every point expressed in cylindrical coordinates are derived. This case includes both cylindrical symmetric (due to vertical) and non-symmetric (due to horizontal) load cases. Both cylindrical symmetric and non-symmetric load cases correspond to a circumferential mode number  $n$ . The circumferential mode number  $n$  is respectively zero and one for a cylindrical symmetric and antisymmetric load. Higher mode numbers are not considered, since only a vertical and horizontal load on an element are included. For both a vertical and horizontal load, Green's functions are derived to describe the flexibility of the soils surface. Hereafter, the surface is discretized and the flexibility and stiffness matrix are constructed.

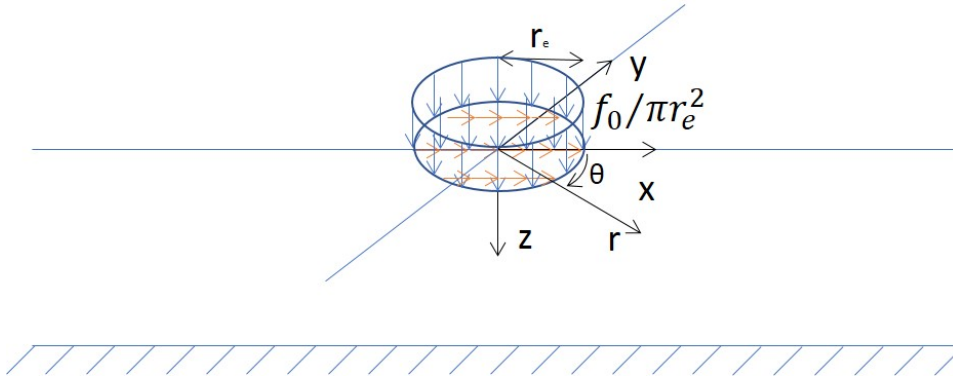


Figure 5.1: Schematisation of the applied harmonic load on the soil

### 5.1. Hankel-transform of the wave equation

For the general derivation which includes both cylindrical symmetric and non-symmetric modes, the wave equation is rewritten in Helmholtz potentials  $\phi, \psi$  &  $\chi$  corresponding to the P-, SV- and SH- waves respectively, as introduced in Aki and Richards (2002). A brief derivation of the potentials and Eq. (5.1) by Helmholtz decomposition is preformed in appendix B. The displacement field is expressed as:

$$\tilde{\mathbf{u}}(r, \theta, z, \omega) = \nabla \tilde{\phi} + \nabla \times \nabla \times (0, 0, \tilde{\psi}) + \nabla \times (0, 0, \tilde{\chi}) \quad (5.1)$$

The vector potential related to the P-wave can easily be obtained. The SV- and SH- wave vectors are described by:

$$\begin{aligned} \nabla \times \nabla \times (0, 0, \tilde{\psi}) &= \left[ \frac{\partial^2 \tilde{\psi}}{\partial r \partial z} \hat{\mathbf{r}} + \frac{1}{r} \frac{\partial^2 \tilde{\psi}}{\partial \theta \partial z} \hat{\boldsymbol{\theta}} - \frac{1}{r} \left( \frac{\partial}{\partial r} \left( \frac{r \partial \tilde{\psi}}{\partial r} \right) + \frac{1}{r} \frac{\partial^2 \tilde{\psi}}{\partial \theta^2} \right) \hat{\mathbf{z}} \right], \\ \nabla \times (0, 0, \tilde{\chi}) &= \left[ \frac{1}{r} \frac{\partial \tilde{\chi}}{\partial \theta} \hat{\mathbf{r}} - \frac{\partial \tilde{\chi}}{\partial r} \hat{\boldsymbol{\theta}} \right] \end{aligned} \quad (5.2)$$

This results in:

$$\begin{aligned}\tilde{u}_r(r, \theta, z, \omega) &= \frac{\partial \tilde{\phi}}{\partial r} + \frac{\partial^2 \tilde{\psi}}{\partial r \partial z} + \frac{1}{r} \frac{\partial \tilde{\chi}}{\partial \theta}, \\ \tilde{u}_\theta(r, \theta, z, \omega) &= \frac{\partial \tilde{\phi}}{r \partial \theta} + \frac{1}{r} \frac{\partial^2 \tilde{\psi}}{\partial \theta \partial z} - \frac{\partial \tilde{\chi}}{\partial r}, \\ \tilde{u}_z(r, \theta, z, \omega) &= \frac{\partial \tilde{\phi}}{\partial z} - \frac{1}{r} \frac{\partial}{\partial r} \left( \frac{r \partial \tilde{\psi}}{\partial r} \right) - \frac{1}{r^2} \frac{\partial^2 \tilde{\psi}}{\partial \theta^2}\end{aligned}\quad (5.3)$$

The corresponding stresses are obtained by the standard stress strain relations:

$$\begin{aligned}\tilde{\sigma}_{zr}(r, \theta, z, \omega) &= \mu \left( \frac{\partial \tilde{u}_r}{\partial z} + \frac{\partial \tilde{u}_z}{\partial r} \right), \\ \tilde{\sigma}_{z\theta}(r, \theta, z, \omega) &= \mu \left( \frac{1}{r} \frac{\partial \tilde{u}_z}{\partial \theta} + \frac{\partial \tilde{u}_\theta}{\partial z} \right), \\ \tilde{\sigma}_{zz}(r, \theta, z, \omega) &= (\lambda + 2\mu) \frac{\partial \tilde{u}_z}{\partial z} + \lambda \left( \frac{1}{r} \frac{\partial (r \tilde{u}_r)}{\partial r} + \frac{1}{r} \frac{\partial \tilde{u}_\theta}{\partial \theta} \right)\end{aligned}\quad (5.4)$$

Each potential is chosen such that it satisfies a decoupled equation of motions in the frequency domain:

$$\begin{aligned}\nabla^2 \tilde{\phi}(r, \theta, z, \omega) + \frac{\omega^2}{c_p^2} \tilde{\phi}(r, \theta, z, \omega) &= 0, \\ \nabla^2 \tilde{\psi}(r, \theta, z, \omega) + \frac{\omega^2}{c_s^2} \tilde{\psi}(r, \theta, z, \omega) &= 0, \\ \nabla^2 \tilde{\chi}(r, \theta, z, \omega) + \frac{\omega^2}{c_s^2} \tilde{\chi}(r, \theta, z, \omega) &= 0\end{aligned}\quad (5.5)$$

Wherein the lambda operator in circular coordinates is given as:

$$\nabla^2 = \frac{\partial^2}{\partial r^2} + \frac{1}{r} \frac{\partial}{\partial r} + \frac{1}{r^2} \frac{\partial^2}{\partial \theta^2} + \frac{\partial^2}{\partial z^2}\quad (5.6)$$

The separation of variables creates a  $\theta$  independent function:

$$\begin{aligned}\tilde{\phi}(r, \theta, z, \omega) &= \cos(n\theta) \hat{\phi}(r, z, \omega), \\ \tilde{\psi}(r, \theta, z, \omega) &= \cos(n\theta) \hat{\psi}(r, z, \omega), \\ \tilde{\chi}(r, \theta, z, \omega) &= -\sin(n\theta) \hat{\chi}(r, z, \omega)\end{aligned}\quad (5.7)$$

Substitute Eq. (5.7) in the wave equations described in Eq. (5.5) results in wave equations of which the general solution is described with Bessel J functions:

$$\begin{aligned}\left( \frac{\partial^2}{\partial r^2} + \frac{1}{r} \frac{\partial}{\partial r} - \frac{n^2}{r^2} + \frac{\partial^2}{\partial z^2} \right) \hat{\phi}(r, z, \omega) + \frac{\omega^2}{c_p^2} \hat{\phi}(r, z, \omega) &= 0, \\ \left( \frac{\partial^2}{\partial r^2} + \frac{1}{r} \frac{\partial}{\partial r} - \frac{n^2}{r^2} + \frac{\partial^2}{\partial z^2} \right) \hat{\psi}(r, z, \omega) + \frac{\omega^2}{c_s^2} \hat{\psi}(r, z, \omega) &= 0, \\ \left( \frac{\partial^2}{\partial r^2} + \frac{1}{r} \frac{\partial}{\partial r} - \frac{n^2}{r^2} + \frac{\partial^2}{\partial z^2} \right) \hat{\chi}(r, z, \omega) + \frac{\omega^2}{c_s^2} \hat{\chi}(r, z, \omega) &= 0\end{aligned}\quad (5.8)$$

By substituting Eq. (5.7) in both equations for displacements and stresses, the  $\theta$  dependence is separated such that:

$$\begin{aligned}\tilde{u}_r(r, \theta, z, \omega) &= \cos(n\theta) \hat{u}_r(r, z, \omega), & \tilde{\sigma}_{zr}(r, \theta, z, \omega) &= \cos(n\theta) \hat{\sigma}_{zr}(r, z, \omega), \\ \tilde{u}_\theta(r, \theta, z, \omega) &= -\sin(n\theta) \hat{u}_\theta(r, z, \omega), & \tilde{\sigma}_{z\theta}(r, \theta, z, \omega) &= -\sin(n\theta) \hat{\sigma}_{z\theta}(r, z, \omega), \\ \tilde{u}_z(r, \theta, z, \omega) &= \cos(n\theta) \hat{u}_z(r, z, \omega), & \tilde{\sigma}_{zz}(r, \theta, z, \omega) &= \cos(n\theta) \hat{\sigma}_{zz}(r, z, \omega)\end{aligned}\quad (5.9)$$

Which results in:

$$\begin{aligned}\hat{u}_r(r, z, \omega) &= \frac{\partial \hat{\phi}}{\partial r} + \frac{\partial^2 \hat{\psi}}{\partial r \partial z} - \frac{n}{r} \hat{\chi}, \\ \hat{u}_\theta(r, z, \omega) &= \frac{n}{r} \hat{\phi} + \frac{n}{r} \frac{\partial \hat{\psi}}{\partial z} - \frac{\partial \hat{\chi}}{\partial r}, \\ \hat{u}_z(r, z, \omega) &= \frac{\partial \hat{\phi}}{\partial z} - \frac{1}{r} \frac{\partial}{\partial r} \left( \frac{r \partial \hat{\psi}}{\partial r} \right) + \frac{n^2}{r^2} \hat{\psi}\end{aligned}\quad (5.10)$$

And:

$$\begin{aligned}\hat{\sigma}_{zr} &= \mu \left( \frac{\partial \hat{u}_r}{\partial z} + \frac{\partial \hat{u}_z}{\partial r} \right), \\ \hat{\sigma}_{z\theta} &= \mu \left( \frac{n}{r} \hat{u}_z + \frac{\partial \hat{u}_\theta}{\partial z} \right), \\ \hat{\sigma}_{zz} &= (\lambda + 2\mu) \frac{\partial \hat{u}_z}{\partial z} + \lambda \left( \frac{1}{r} \frac{\partial(r \hat{u}_r)}{\partial r} - \frac{n}{r} \hat{u}_\theta \right)\end{aligned}\quad (5.11)$$

To find the general solution of the wave equations, the Hankel transform is applied with respect to the radial coordinate.

$$\begin{aligned}f^{H_n} &= \int_0^\infty r f(r) J_n(kr) dr, \\ f(r) &= \int_0^\infty k f^{H_n} J_n(kr) dk\end{aligned}\quad (5.12)$$

By applying this transform Eq. (5.5) reads:

$$\begin{aligned}\frac{\partial^2 \hat{\phi}^{H_n}}{\partial z^2} - \alpha^2 \hat{\phi}^{H_n} &= 0, \\ \frac{\partial^2 \hat{\psi}^{H_n}}{\partial z^2} - \beta^2 \hat{\psi}^{H_n} &= 0, \\ \frac{\partial^2 \hat{\chi}^{H_n}}{\partial z^2} - \beta^2 \hat{\chi}^{H_n} &= 0\end{aligned}\quad (5.13)$$

The general solution of Eq. (5.13) is

$$\begin{aligned}\hat{\phi}^{H_n} &= A_1 e^{-\alpha z} + A_2 e^{\alpha z}, \\ \hat{\psi}^{H_n} &= A_3 e^{-\beta z} + A_4 e^{\beta z}, \\ \hat{\chi}^{H_n} &= A_5 e^{-\beta z} + A_6 e^{\beta z}\end{aligned}\quad (5.14)$$

With:

$$\alpha = \sqrt{k^2 - \frac{\omega^2}{c_p^2}}, \quad \beta = \sqrt{k^2 - \frac{\omega^2}{c_s^2}}\quad (5.15)$$

And in accordance with the definition of the Hankel transform:

$$\begin{aligned}\hat{\phi}(r, z, \omega) &= \int_0^\infty k \hat{\phi}^{H_n}(k, z, \omega) J_n(kr) dk, \\ \hat{\psi}(r, z, \omega) &= \int_0^\infty k \hat{\psi}^{H_n}(k, z, \omega) J_n(kr) dk, \\ \hat{\chi}(r, z, \omega) &= \int_0^\infty k \hat{\chi}^{H_n}(k, z, \omega) J_n(kr) dk\end{aligned}\quad (5.16)$$

Substituting Eq. (5.16) in the equations for the displacements, Eq. (5.10) results in:

$$\begin{aligned}\hat{u}_r(r, z, \omega) &= \int_0^\infty k \left\{ \left[ \hat{\phi}^{H_n} + \frac{\partial \hat{\psi}^{H_n}}{\partial z} \right] J_n(kr)_{,r} - \hat{\chi}^{H_n} \frac{n}{r} J_n(kr) \right\} dk \\ \hat{u}_\theta(r, z, \omega) &= \int_0^\infty k \left\{ \left[ \hat{\phi}^{H_n} + \frac{\partial \hat{\psi}^{H_n}}{\partial z} \right] \frac{n}{r} J_n(kr) - \hat{\chi}^{H_n} J_n(kr)_{,r} \right\} dk \\ \hat{u}_z(r, z, \omega) &= \int_0^\infty k \left\{ \left[ \frac{\partial \hat{\phi}^{H_n}}{\partial z} - \frac{(-k^2 r^2 + n^2)}{r^2} \hat{\psi}^{H_n} + \frac{n^2}{r^2} \hat{\psi}^{H_n} \right] J_n(kr) \right\} dk\end{aligned}\quad (5.17)$$

Since all  $\zeta^{H_n}$  functions contain arbitrary integration constants, they are allowed to be scaled with any constant (Kausel, 2006). This is necessary to obtain converging integrals after turning the order of the integral with

respect to  $k$  and derivatives with respect to  $r$  and  $z$ . A rescaling factor  $\frac{1}{k}$  is applied to  $\hat{\psi}^{H_n}$  and  $\hat{\chi}^{H_n}$ . By considering  $\frac{1}{k} J_n(kr)_{,r} = J_n(kr)_{,(kr)}$ , Eq. (5.17) results in:

$$\begin{aligned}
\hat{u}_r(r, z, \omega) &= \int_0^\infty k \left\{ \left[ k \hat{\phi}^{H_n} + \frac{\partial \hat{\psi}^{H_n}}{\partial z} \right] \frac{1}{k} J_n(kr)_{,r} - \hat{\chi}^{H_n} \frac{n}{kr} J_n(kr) \right\} dk \\
&= \int_0^\infty k \left\{ r_1(z) J_n(kr)_{,(kr)} + l_1(z) \frac{n}{kr} J_n(kr) \right\} dk, \\
\hat{u}_\theta(r, z, \omega) &= \int_0^\infty k \left\{ \left[ k \hat{\phi}^{H_n} + \frac{\partial \hat{\psi}^{H_n}}{\partial z} \right] \frac{n}{kr} J_n(kr) - \hat{\chi}^{H_n} \frac{1}{k} J_n(kr)_{,r} \right\} dk \\
&= \int_0^\infty k \left\{ r_1(z) \frac{n}{kr} J_n(kr) + l_1(z) J_n(kr)_{,(kr)} \right\} dk, \\
\hat{u}_z(r, z, \omega) &= \int_0^\infty k \left\{ \left[ \frac{\partial \hat{\phi}^{H_n}}{\partial z} + k \hat{\psi}^{H_n} \right] J_n(kr) \right\} dk \\
&= \int_0^\infty k \{ r_2(z) J_n(kr) \} dk
\end{aligned} \tag{5.18}$$

And after some algebra, the corresponding stress equations result in:

$$\begin{aligned}
\hat{\sigma}_{zr}(r, z, \omega) &= \mu \int_0^\infty k \left\{ \frac{\partial r_1(z)}{\partial z} \frac{1}{k} J_n(kr)_{,r} - \frac{\partial l_1(z)}{\partial z} \frac{n}{kr} J_n(kr) + kr_2(z) \frac{1}{k} J_n(kr)_{,r} \right\} dk \\
&= \int_0^\infty k \left\{ r_3(z) J_n(kr)_{,(kr)} + l_2(z) \frac{n}{kr} J_n(kr) \right\} dk, \\
\hat{\sigma}_{z\theta}(r, z, \omega) &= \mu \int_0^\infty k \left\{ kr_2(z) \frac{n}{kr} J_n(kr) + \frac{\partial r_1(z)}{\partial z} \frac{n}{kr} J_n(kr) + \frac{\partial l_1(z)}{\partial z} \frac{1}{k} J_n(kr)_{,r} \right\} dk \\
&= \int_0^\infty k \left\{ r_3(z) \frac{n}{kr} J_n(kr) + l_2(z) J_n(kr)_{,(kr)} \right\} dk, \\
\hat{\sigma}_{zz}(r, z, \omega) &= \int_0^\infty k \left\{ (\lambda + 2\mu) \frac{\partial r_2(z)}{\partial z} J_n(kr) - \lambda kr_1(z) J_n(kr) \right\} dk \\
&= \int_0^\infty k \{ r_4(z) J_n(kr) \} dk,
\end{aligned} \tag{5.19}$$

A collaboration of the  $z$ -dependent variables, wherein  $r_n$  corresponds to the coupled PSV-waves and  $l_n$  to the SH-wave:

$$\begin{aligned}
r_1(z) &= k \hat{\phi}^{H_n}(z) + \frac{\partial \hat{\psi}^{H_n}(z)}{\partial z}, & r_2(z) &= \frac{\partial \hat{\phi}^{H_n}(z)}{\partial z} + k \hat{\psi}^{H_n}(z), & l_1(z) &= -\hat{\chi}^{H_n}(z) \\
r_3(z) &= \mu \left( kr_2(z) + \frac{\partial r_1(z)}{\partial z} \right), & r_4(z) &= (\lambda + 2\mu) \frac{\partial r_2(z)}{\partial z} - \lambda kr_1(z), & l_2(z) &= \mu \frac{\partial l_1(z)}{\partial z}
\end{aligned} \tag{5.20}$$

The equations for the displacements and stresses in the frequency domain are:

$$\begin{aligned}
\tilde{u}_r(r, \theta, z, \omega) &= \cos(n\theta) \int_0^\infty k \left\{ r_1(z) J_n(kr)_{,(kr)} + l_1(z) \frac{n}{kr} J_n(kr) \right\} dk, \\
\tilde{u}_\theta(r, \theta, z, \omega) &= -\sin(n\theta) \int_0^\infty k \left\{ r_1(z) \frac{n}{kr} J_n(kr) + l_1(z) J_n(kr)_{,(kr)} \right\} dk, \\
\tilde{u}_z(r, \theta, z, \omega) &= \cos(n\theta) \int_0^\infty k \{ r_2(z) J_n(kr) \} dk, \\
\tilde{\sigma}_{zr}(r, \theta, z, \omega) &= \cos(n\theta) \int_0^\infty k \left\{ r_3(z) J_n(kr)_{,(kr)} + l_2(z) \frac{n}{kr} J_n(kr) \right\} dk, \\
\tilde{\sigma}_{z\theta}(r, \theta, z, \omega) &= -\sin(n\theta) \int_0^\infty k \left\{ r_3(z) \frac{n}{kr} J_n(kr) + l_2(z) J_n(kr)_{,(kr)} \right\} dk, \\
\tilde{\sigma}_{zz}(r, \theta, z, \omega) &= \cos(n\theta) \int_0^\infty k \{ r_4(z) J_n(kr) \} dk,
\end{aligned} \tag{5.21}$$

It is convenient to rewrite the equations in matrix form, such that the dependence on  $r$ ,  $\theta$  and  $z$  is separated.

$$\begin{aligned}\tilde{\mathbf{u}}(r, \theta, z, \omega) &= \int_0^\infty k \mathbf{T}_n(\theta) \mathbf{J}_n(k, r) \mathbf{R}_u(z) \\ \tilde{\mathbf{s}}(r, \theta, z, \omega) &= \int_0^\infty k \mathbf{T}_n(\theta) \mathbf{J}_n(k, r) \mathbf{R}_s(z)\end{aligned}\quad (5.22)$$

In which  $\mathbf{T}$  is a translation matrix around  $\theta$ ,  $\mathbf{J}$  is a matrix containing the Bessel J functions, describing the propagating and decaying behaviour of the waves and  $\mathbf{R}_n$  are vectors containing the  $z$ -dependence, including the unknowns  $A_n$  that are found by the boundary conditions.

$$\begin{aligned}\mathbf{T}_n &= \text{diag}[\cos(n\theta), -\sin(n\theta), \cos(n\theta)], \\ \mathbf{J}_n &= \begin{bmatrix} J_n(kr), (kr) & \frac{n}{kr} J_n(kr) & 0 \\ \frac{n}{kr} J_n(kr) & J_n(kr), (kr) & 0 \\ 0 & 0 & J_n(kr) \end{bmatrix}, \\ \mathbf{R}_u(z) &= [r_1(z), l_1(z), r_2(z)]^T, \\ \mathbf{R}_s(z) &= [r_3(z), l_2(z), r_4(z)]^T\end{aligned}\quad (5.23)$$

The kernel  $\mathbf{R}_u(z)$  and  $\mathbf{R}_s(z)$ , containing the unknowns  $A_n$  is written out in matrix form as:

$$\begin{bmatrix} \mathbf{R}_u(z) \\ \mathbf{R}_s(z) \end{bmatrix} = \begin{bmatrix} ke^{-\alpha z} & ke^{\alpha z} & -\beta e^{-\beta z} & \beta e^{\beta z} & 0 & 0 \\ 0 & 0 & 0 & 0 & -e^{-\beta z} & -e^{\beta z} \\ -\alpha e^{-\alpha z} & \alpha e^{\alpha z} & ke^{-\beta z} & ke^{\beta z} & 0 & 0 \\ -2k\mu\alpha e^{-\alpha z} & 2k\mu\alpha e^{\alpha z} & \mu e^{-\beta z}(\beta^2 + k^2) & \mu e^{\beta z}(\beta^2 + k^2) & 0 & 0 \\ 0 & 0 & 0 & 0 & \mu\beta e^{-\beta z} & -\mu\beta e^{\beta z} \\ \mu(\beta^2 + k^2)e^{-\alpha z} & \mu(\beta^2 + k^2)e^{\alpha z} & -2k\mu\beta e^{-\beta z} & 2k\mu\beta e^{\beta z} & 0 & 0 \end{bmatrix} \begin{bmatrix} A_1 \\ A_2 \\ A_3 \\ A_4 \\ A_5 \\ A_6 \end{bmatrix}\quad (5.24)$$

## 5.2. Homogeneous boundary conditions

The unique solutions of the homogeneous boundary conditions are expressed in terms of roots and are found by solving the homogeneous boundary conditions (Eq. (5.25)) that holds for all  $r$  and  $\theta$ .

$$\tilde{\mathbf{u}}(r, \theta, h, \omega) = 0, \quad \tilde{\boldsymbol{\sigma}}(r, \theta, 0, \omega) = 0 \quad (5.25)$$

Since  $\mathbf{T}_n$  and  $\mathbf{J}_n$  depend on either  $r$  or  $\theta$ ,  $\mathbf{R}_u(h)$  and  $\mathbf{R}_s(0)$  should be zero to fulfil the boundary conditions for the stress and displacements. The unknowns from Eq. (5.24) for considering homogeneous boundaries are found by solving:

$$\begin{bmatrix} \mathbf{R}_u(h) \\ \mathbf{R}_s(0) \end{bmatrix} = \begin{bmatrix} ke^{-\alpha h} & ke^{\alpha h} & -\beta e^{-\beta h} & \beta e^{\beta h} & 0 & 0 \\ 0 & 0 & 0 & 0 & -e^{-\beta h} & -e^{\beta h} \\ -\alpha e^{-\alpha h} & \alpha e^{\alpha h} & ke^{-\beta h} & ke^{\beta h} & 0 & 0 \\ -2k\mu\alpha & 2k\mu\alpha & \mu(\beta^2 + k^2) & \mu(\beta^2 + k^2) & 0 & 0 \\ 0 & 0 & 0 & 0 & \mu\beta & -\mu\beta \\ \mu(\beta^2 + k^2) & \mu(\beta^2 + k^2) & -2k\mu\beta & 2k\mu\beta & 0 & 0 \end{bmatrix} \begin{bmatrix} A_1 \\ A_2 \\ A_3 \\ A_4 \\ A_5 \\ A_6 \end{bmatrix} = 0 \quad (5.26)$$

The components depending on the anti-plane wave (SH) and the coupled PSV-wave are collected and decoupled, resulting in two matrices, that are solved separately.

$$\begin{bmatrix} \mathbf{R}_u(h) \\ \mathbf{R}_s(0) \end{bmatrix} = \begin{bmatrix} ke^{-\alpha h} & ke^{\alpha h} & -\beta e^{-\beta h} & \beta e^{\beta h} \\ -\alpha e^{-\alpha h} & \alpha e^{\alpha h} & ke^{-\beta h} & ke^{\beta h} \\ -2k\mu\alpha & 2k\mu\alpha & \mu(\beta^2 + k^2) & \mu(\beta^2 + k^2) \\ \mu(\beta^2 + k^2) & \mu(\beta^2 + k^2) & -2k\mu\beta & 2k\mu\beta \end{bmatrix}_{psv} \begin{bmatrix} A_1 \\ A_2 \\ A_3 \\ A_4 \end{bmatrix} + \begin{bmatrix} -e^{-\beta h} & -e^{\beta h} \\ \mu\beta & -\mu\beta \end{bmatrix}_{sh} \begin{bmatrix} A_5 \\ A_6 \end{bmatrix} = 0 \quad (5.27)$$

The determinant of the kernel related to both the PSV- and SH- wave coefficients should be solved to find the unique wavenumbers.

$$\begin{aligned} \Delta_{psv} &= \Delta = \mathbf{Det}[\dots]_{psv} = 0, & \Delta_{sh} &= \Delta^* = \mathbf{Det}[\dots]_{sh} = 0 \\ \Delta &= \mu \left( (\alpha\beta + k^2) \left( -4\beta\alpha k^2 - (\beta^2 + k^2)^2 \right) \left( e^{h(\alpha-\beta)} + e^{-h(\alpha-\beta)} \right) \right. \\ &\quad \left. + (\alpha\beta - k^2) \left( 4\beta\alpha k^2 - (\beta^2 + k^2)^2 \right) \left( e^{-h(\alpha+\beta)} + e^{h(\alpha+\beta)} \right) + 16k^2\beta\alpha(\beta^2 + k^2) \right) \\ \Delta^* &= \mu\beta e^{\beta h} + \mu\beta e^{-\beta h} = 0 \end{aligned} \quad (5.28)$$

The solution to the determinant corresponding to the PSV-wave is exactly the same as found in the 2D plane-strain case as described in Eq. (3.23). Therefore, the same roots are used. The solution of the determinant corresponding to the SH-wave is set to zero results in an infinite amount of roots  $k_{sh}$ :

$$k_{sh} = \begin{cases} \pm k_s \\ \pm \frac{\sqrt{4k_s^2 h^2 - \pi^2(2n+1)}}{2h} \end{cases} \quad (5.29)$$

The unknowns  $A_1$  to  $A_6$  are solved for different boundary conditions. The modes of the soil are similar to the 2D plane-strain case decoupled in a PSV- and SH-wave component and can be solved separately. The roots corresponding to Eq. (5.29) for normalized frequencies are shown in figure 5.2

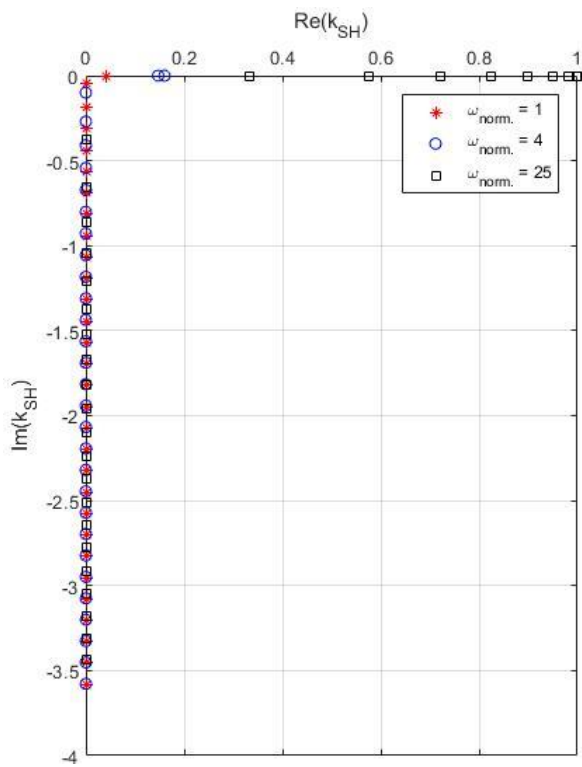


Figure 5.2: First 30 roots ( $k_{SH}$ ) found in the negative half plane for normalized frequencies 1, 4 and 25. ( $\omega_{norm.} = \frac{\omega h}{c_s}$ )

### 5.3. A cylindrical symmetric vertical load

The case considered is a vertical load over a circular area. This load is equal for every  $\theta$ . Therefore, it is called cylindrical symmetric. The index  $s$  refers to the cylindrical symmetric vertical load. The magnitude of the stress is normalized to the area, such that the total stress over the area equals 1. The boundary conditions that are applied in this load case are:

$$\begin{aligned} \tilde{u}_r(r, \theta, h, \omega) &= 0, & \tilde{\sigma}_{zr}(r, \theta, 0, \omega) &= 0, \\ \tilde{u}_\theta(r, \theta, h, \omega) &= 0, & \tilde{\sigma}_{z\theta}(r, \theta, 0, \omega) &= 0, \\ \tilde{u}_z(r, \theta, h, \omega) &= 0, & \tilde{\sigma}_{zz}(r, \theta, 0, \omega) &= -\frac{F_z}{\pi r_e^2} H(r_e - r), \end{aligned} \quad (5.30)$$

Eq. (5.30) is solved in the Hankel domain by applying a forward Hankel transform (Wolf, 1985):

$$\tilde{\mathbf{p}}(k) = -a_n \int_0^\infty r J_n \int_0^{2\pi} \mathbf{T}_n \mathbf{T}_0 \begin{bmatrix} 0 \\ 0 \\ 1 \end{bmatrix} \frac{F_z}{\pi r_e^2} H(r_e - r) d\theta dr \quad (5.31)$$

Where  $r_e$  is the radius of the foundation plate and  $a_n$  is a normalization constant:

$$a_n = \begin{cases} \frac{1}{2\pi} & n = 0 \\ \frac{1}{\pi} & n \neq 0 \end{cases} \quad (5.32)$$

Since the orthogonality conditions need to be satisfied, the integral in the azimuth  $\theta$  only gives a solution for  $n = 0$  (Kausel, 2006):

$$\int_0^{2\pi} \mathbf{T}_m \mathbf{T}_n d\theta = \frac{1}{a_n} \delta_{mn} \quad (5.33)$$

Applying this orthogonality, Eq. (5.31) results in:

$$\begin{aligned} \tilde{\mathbf{p}}(k) &= -\int_0^{r_e} r \begin{bmatrix} J_0(kr), (kr) & 0 & 0 \\ 0 & J_0(kr), (kr) & 0 \\ 0 & 0 & J_0(kr) \end{bmatrix} \begin{bmatrix} 0 \\ 0 \\ 1 \end{bmatrix} \frac{F_z}{\pi r_e^2} dr \\ &= -\int_0^{r_e} r J_0(kr) \frac{F_z}{\pi r_e^2} \begin{bmatrix} 0 \\ 0 \\ 1 \end{bmatrix} dr = -\frac{F_z}{\pi k r_e} J_1(kr_e) \begin{bmatrix} 0 \\ 0 \\ 1 \end{bmatrix} \end{aligned} \quad (5.34)$$

The equations for the displacements are reduced, since only  $n = 0$  is considered. Therefore, Eq. (5.18) becomes:

$$\begin{aligned} \tilde{u}_r^s(r, \theta, z, \omega) &= \int_0^\infty k \{r_1(0) J_0(kr), (kr)\} dk, \\ \tilde{u}_\theta^s(r, \theta, z, \omega) &= 0 \\ \tilde{u}_z^s(r, \theta, z, \omega) &= \int_0^\infty k \{r_2(0) J_0(kr)\} dk \end{aligned} \quad (5.35)$$

Since the z-dependent functions  $l_n$  related to the SH-wave equals zero,  $A_5$  and  $A_6$  are zero and only the unknowns  $A_1$  to  $A_4$  are found by solving for the boundary conditions. Similar to the homogeneous case, the boundary conditions should hold everywhere, and should be independent of  $\theta$  and  $r$ . The kernel is constructed from  $\mathbf{R}_u^s(h)$  and  $\mathbf{R}_s^s(0)$  as preformed in Eq. (5.26) for the homogeneous case.

$$\begin{bmatrix} \mathbf{R}_u^s(h) \\ \mathbf{R}_s^s(0) \end{bmatrix} = \begin{bmatrix} ke^{-\alpha h} & ke^{\alpha h} & -\beta e^{-\beta h} & \beta e^{\beta h} \\ -\alpha e^{-\alpha h} & \alpha e^{\alpha h} & ke^{-\beta h} & ke^{\beta h} \\ -2k\mu\alpha & 2k\mu\alpha & \mu(\beta^2 + k^2) & \mu(\beta^2 + k^2) \\ \mu(\beta^2 + k^2) & \mu(\beta^2 + k^2) & -2k\mu\beta & 2k\mu\beta \end{bmatrix} \begin{bmatrix} A_1^s \\ A_2^s \\ A_3^s \\ A_4^s \end{bmatrix} = \frac{-F_z}{\pi k r_e} J_1(kr_e) \begin{bmatrix} 0 \\ 0 \\ 0 \\ 1 \end{bmatrix} \quad (5.36)$$

The coefficients for this case result in:

$$\begin{bmatrix} A_1^s \\ A_2^s \\ A_3^s \\ A_4^s \end{bmatrix} = \begin{bmatrix} -(\alpha\beta + k^2)(\beta^2 + k^2)e^{h(\alpha-\beta)} + (-\alpha\beta + k^2)(\beta^2 + k^2)e^{h(\alpha+\beta)} + 4\beta\alpha k^2 \\ -(\alpha\beta + k^2)(\beta^2 + k^2)e^{h(-\alpha+\beta)} + (-\alpha\beta + k^2)(\beta^2 + k^2)e^{-h(\alpha+\beta)} + 4\beta\alpha k^2 \\ -2k\alpha \left( e^{h(\alpha+\beta)}\alpha\beta - e^{h(\alpha+\beta)}k^2 - e^{h(-\alpha+\beta)}\alpha\beta - e^{h(-\alpha+\beta)}k^2 + \beta^2 + k^2 \right) \\ 2k\alpha \left( \beta^2 + k^2 + e^{-h(\alpha+\beta)}\alpha\beta - e^{-h(\alpha+\beta)}k^2 - e^{h(\alpha-\beta)}\alpha\beta - e^{h(\alpha-\beta)}k^2 \right) \end{bmatrix} \frac{-F_z}{\pi k r_e} \frac{J_1(kr_e)}{\Delta(k)} \quad (5.37)$$

The equations for the unknowns are substituted into Eq. (5.21). Together with substituting  $n = 0$ , the flexibility functions due to a vertical force are given in form of the inverse Hankel transform.

$$\begin{aligned} \tilde{u}_r^s(r, \theta, 0, \omega) &= -\frac{F_z}{\pi r_e} \int_0^\infty \frac{f_{r_1}^s(k)}{\Delta(k)} J_1(kr_e) J_0(kr)_{,(kr)} dk = \frac{F_z}{\pi r_e} \int_0^\infty \frac{f_{r_1}^s(k)}{\Delta(k)} J_1(kr_e) J_1(kr) dk \\ \tilde{u}_z^s(r, \theta, 0, \omega) &= -\frac{F_z}{\pi r_e} \int_0^\infty \frac{f_{r_2}^s(k)}{\Delta(k)} J_1(kr_e) J_0(kr) dk \end{aligned} \quad (5.38)$$

In which  $f_{r_1}^s$  and  $f_{r_2}^s$  are related to the numerator of  $r_1$  and  $r_2$  for the cylindrical symmetric ( $^s$ ) case.

$$\begin{aligned} f_{r_1}^s(k) &= -k \left( (\alpha\beta + k^2)(2\alpha\beta + \beta^2 + k^2) \left( e^{h(\alpha-\beta)} + e^{-h(\alpha-\beta)} \right) \right. \\ &\quad \left. - (-\alpha\beta + k^2)(-2\alpha\beta + \beta^2 + k^2) \left( e^{-h(\alpha+\beta)} + e^{h(\alpha+\beta)} \right) - 4\alpha\beta(\beta^2 + 3k^2) \right) \\ f_{r_2}^s(k) &= -\alpha(\beta^2 - k^2) \left( (\alpha\beta + k^2) \left( -e^{h(\alpha-\beta)} + e^{-h(\alpha-\beta)} \right) + \left( e^{h(\alpha+\beta)} - e^{-h(\alpha+\beta)} \right) (-\alpha\beta + k^2) \right) \end{aligned} \quad (5.39)$$

The integrals in Eq. (5.38) contain two Bessel J functions, both depending on the integration variable  $k$ . The function can be expanded from the positive domain to the complete domain by making use of the derivation done in appendix A, in which the integration over a Bessel J function is rewritten into the integration over either a Hankel H1 or Hankel H2 function. It is arbitrarily chosen to use the Hankel function of first kind during the further derivation, this is allowed as long as the dispersion conditions are fulfilled. Both equations for both domains fulfil the condition, mentioned in appendix A, that the symmetry (odd or even) of the pre-multiplication is contrary to the Bessel J function, that is rewritten into a Hankel H1 function. Therefore, Eq. (5.38) is rewritten as either:

$$\begin{aligned} \tilde{u}_r^s(r, \theta, 0, \omega) &= \frac{1}{2} \frac{F_z}{\pi r_e} \int_{-\infty}^\infty \frac{f_{r_1}^s(k)}{\Delta(k)} H_1^{(1)}(kr_e) J_1(kr) dk = \frac{1}{2} \frac{F_z}{\pi r_e} \int_{-\infty}^\infty \frac{f_{r_1}^s(k)}{\Delta(k)} J_1(kr_e) H_1^{(1)}(kr) dk \\ \tilde{u}_z^s(r, \theta, 0, \omega) &= -\frac{1}{2} \frac{F_z}{\pi r_e} \int_{-\infty}^\infty \frac{f_{r_2}^s(k)}{\Delta(k)} H_1^{(1)}(kr_e) J_0(kr) dk = -\frac{1}{2} \frac{F_z}{\pi r_e} \int_{-\infty}^\infty \frac{f_{r_2}^s(k)}{\Delta(k)} J_1(kr_e) H_0^{(1)}(kr) dk \end{aligned} \quad (5.40)$$

### 5.3.1. Contour integration for the cylindrical symmetric load

Eq. (5.40) can be solved by making use of contour integration and the residue theorem. In Eq. (5.41), a quick recap is written how to solve an integral over equation  $\phi$  by making use of contour integration. Further explanation about contour integration and the php and nhp is preformed in section 3.4, including a figure with the used integration path.

$$\int_{-\infty}^\infty \phi = \pm 2\pi i \sum_n \text{Res}(k_x, \phi) - \int_{C_1} \phi - \int_{C_2} \phi - \int_{C_n} \phi - \int_{C_\infty} \phi \quad (5.41)$$

The series expansion for  $r \rightarrow \infty$  of the  $H_0^{(1)}(kr)$  function is in the form of  $e^{iC(k)}$ . To fulfil the dispersive condition, i.e. that the Hankel function decays for  $r \rightarrow \infty$ , anticlockwise integration around the positive complex half plane is applied ( $\Im(k) > 0$ ) including the negative real roots. The integration should hold for all values of  $r$  and therefore, it is not allowed to approach infinity at any  $r$ . Since the largest multiplication of  $r$  within the Bessel J function is dominant, the integration domain must be split into two domains:  $0 < r < r_e$  and  $r_e < r$ , since in the exponential representation of the Bessel J functions,  $r$  is only dominant if it is larger than  $r_e$ . This is shown in Eq. (5.42) in which the exponential part is dominant.

$$\text{Series of } \lim_{k \rightarrow \infty} J_n(ak) H_m^{(1)}(bk) = f(k, a, b, n, m) e^{-ik(a-b)}, \quad \text{holds for: } \Im(k) > 0 \quad \& \quad a \leq b \quad (5.42)$$

Applying the residue theorem on Eq. (5.40), this results in:

$$\begin{aligned}\tilde{u}_r^s(r, \theta, \omega) &= \frac{F_z}{2\pi r_e} \times \begin{cases} 2\pi i \sum_{k=k_m} \frac{f_{r_1}^s(k)}{\Delta(k),k} H_1^{(1)}(kr_e) J_1(kr) - \int_{C_\infty} & 0 < r < r_e \\ 2\pi i \sum_{k=k_m} \frac{f_{r_1}^s(k)}{\Delta(k),k} J_1(kr_e) H_1^{(1)}(kr) - \int_{C_\infty} & r_e \leq r \end{cases} \\ \tilde{u}_z^s(r, \theta, \omega) &= -\frac{F_z}{2\pi r_e} \times \begin{cases} 2\pi i \sum_{k=k_m} \frac{f_{r_2}^s(k)}{\Delta(k),k} H_1^{(1)}(kr_e) J_0(kr) - \int_{C_0} - \int_{C_\infty} & 0 < r < r_e \\ 2\pi i \sum_{k=k_m} \frac{f_{r_2}^s(k)}{\Delta(k),k} J_1(kr_e) H_0^{(1)}(kr) - \int_{C_\infty} & r_e \leq r \end{cases}\end{aligned}\quad (5.43)$$

The integral around a complex integration contour vanishes when its radius approaches infinity. Therefore, this term will drop out of the equations. All except for one of the equations, are 0 for  $k = 0$  since the series expansion of the Hankel functions is in the form of a logarithmic function and the series expansion of the Bessel  $J_1$  function is in the form of  $a_1 k + a_2 k^3 + a_3 k^5 + \dots$ . The multiplication of a logarithmic function with a linear (or higher order) function will go to 0 when its argument approaches 0. The singularity at  $k = 0$  is solved by integrating around the singularity and by making use of the assumptions in Eq. (3.52):

$$k_0 = \lim_{\delta \rightarrow 0} \delta e^{i\phi}, \quad dk_0 = \lim_{\delta \rightarrow 0} i\delta e^{i\phi} d\phi \quad (5.44)$$

Substituting Eq. (5.44) into Eq. (5.40) leads to:

$$\begin{aligned}\int_{C_0} &= \int_{\pi}^0 \lim_{\delta \rightarrow 0} \frac{f_{r_2}^s(\delta e^{i\phi})}{\Delta(\delta e^{i\phi})} H_1^{(1)}(\delta e^{i\phi} r_e) J_0(\delta e^{i\phi} r) \delta i e^{i\phi} d\phi, & 0 < r < r_e \\ &= \int_{\pi}^0 \lim_{\delta \rightarrow 0} \frac{f_{r_2}^s(0)}{\Delta(0)} H_1^{(1)}(\delta e^{i\phi} r_e) J_0(0r) \delta i e^{i\phi} d\phi, & 0 < r < r_e\end{aligned}\quad (5.45)$$

Making use of the series expansion of the Hankel H1 function at  $k = 0$  and  $J_0(0) = 1$ :

$$\begin{aligned}\int_{C_0} &= \int_{\pi}^0 \lim_{\delta \rightarrow 0} \frac{f_{r_2}^s(0)}{\Delta(0)} \left( \frac{-2i}{r_e \pi (\delta e^{i\phi})} + \frac{r_e \left( 2i \ln\left(\frac{(\delta e^{i\phi}) r_e}{2}\right) + 2i\gamma + \pi - i \right) (\delta e^{i\phi})}{2\pi} + O((\delta e^{i\phi})^3) \right) \delta i e^{i\phi} d\phi, \\ &= \int_{\pi}^0 \lim_{\delta \rightarrow 0} \frac{f_{r_2}^s(0)}{\Delta(0)} \frac{-2i \delta i e^{i\phi}}{r_e \pi \delta e^{i\phi}} d\phi = \int_{\pi}^0 \frac{2f_{r_2}^s(0)}{r_e \pi \Delta(0)} d\phi = \left[ \frac{2f_{r_2}^s(0)}{r_e \pi \Delta(0)} \phi \right]_{\pi}^0 = -\frac{2f_{r_2}^s(0)}{r_e \Delta(0)}\end{aligned}\quad (5.46)$$

Eq. (5.46) is substituted in Eq. (5.43) obtaining the final flexibility functions due to a force in z direction:

$$\begin{aligned}\tilde{u}_r^s(r, \theta, \omega) &= -\frac{F_z}{2\pi r_e} \times \begin{cases} 2\pi i \sum_{k=k_m} \frac{f_{r_1}^s(k)}{\Delta(k),k} H_1^{(1)}(kr_e) J_1(kr) & 0 < r < r_e \\ 2\pi i \sum_{k=k_m} \frac{f_{r_1}^s(k)}{\Delta(k),k} J_1(kr_e) H_1^{(1)}(kr) & r_e \leq r \end{cases} \\ \tilde{u}_z^s(r, \theta, \omega) &= \frac{F_z}{2\pi r_e} \times \begin{cases} 2\pi i \sum_{k=k_m} \frac{f_{r_2}^s(k)}{\Delta(k),k} H_1^{(1)}(kr_e) J_0(kr) + \frac{2f_{r_2}^s(0)}{r_e \Delta(0)} & 0 < r < r_e \\ 2\pi i \sum_{k=k_m} \frac{f_{r_2}^s(k)}{\Delta(k),k} J_1(kr_e) H_0^{(1)}(kr) & r_e \leq r \end{cases}\end{aligned}\quad (5.47)$$

## 5.4. An antisymmetric horizontal load

In this case, a horizontal load in  $x$ , i.e. in  $\theta = 0$ , is applied over a circular area. The case is antisymmetric with respect to every  $r$ . The antisymmetric case is referenced to with index  $a$ . The boundary conditions corresponding to this load case are:

$$\begin{aligned}\tilde{u}_r(r, \theta, h, \omega) &= 0, & \tilde{\sigma}_{zr}(r, \theta, 0, \omega) &= \frac{F_x}{\pi r_e^2} H(r_e - r) \cos(\theta), \\ \tilde{u}_\theta(r, \theta, h, \omega) &= 0, & \tilde{\sigma}_{z\theta}(r, \theta, 0, \omega) &= -\frac{F_x}{\pi r_e^2} H(r_e - r) \sin(\theta), \\ \tilde{u}_z(r, \theta, h, \omega) &= 0, & \tilde{\sigma}_{zz}(r, \theta, 0, \omega) &= 0,\end{aligned}\quad (5.48)$$

Similar to the the cylindrical symmetric load case, the applied load is transformed into the Hankel domain:

$$\tilde{\mathbf{p}}(k) = a_n \int_0^\infty r J_n \int_0^{2\pi} \mathbf{T}_n \mathbf{T}_1 \begin{bmatrix} 1 \\ 1 \\ 0 \end{bmatrix} \frac{F_x}{\pi r_e^2} H(r_e - r) d\theta dr \quad (5.49)$$

And due to orthogonality obtained in Eq. (5.33), only the modes corresponding to  $n = 1$  remain:

$$\begin{aligned}\tilde{\mathbf{p}}(k) &= \int_0^{r_e} r \begin{bmatrix} J_1(kr), (kr) & \frac{1}{kr} J_1(kr) & 0 \\ \frac{1}{kr} J_1(kr) & J_1(kr), (kr) & 0 \\ 0 & 0 & J_1(kr) \end{bmatrix} \begin{bmatrix} 1 \\ 1 \\ 0 \end{bmatrix} \frac{F_x}{\pi r_e^2} dr \\ &= \frac{F_x}{\pi r_e^2} \int_0^{r_e} r J_0(kr) \begin{bmatrix} 1 \\ 1 \\ 0 \end{bmatrix} dr = \frac{F_x}{\pi k r_e} J_1(k r_e) \begin{bmatrix} 1 \\ 1 \\ 0 \end{bmatrix}\end{aligned}\quad (5.50)$$

The equations for the displacements of Eq. (5.18), when only  $n = 1$  is considered, become:

$$\begin{aligned}\tilde{u}_r^a(r, \theta, 0, \omega) &= \cos(\theta) \int_0^\infty k \left\{ r_1(0) J_1(kr), (kr) + l_1(0) \frac{1}{kr} J_1(kr) \right\} dk, \\ \tilde{u}_\theta^a(r, \theta, 0, \omega) &= -\sin(\theta) \int_0^\infty k \left\{ r_1(0) \frac{1}{kr} J_1(kr) + l_1(0) J_1(kr), (kr) \right\} dk, \\ \tilde{u}_z^a(r, \theta, 0, \omega) &= \cos(\theta) \int_0^\infty k \{ r_2(0) J_1(kr) \} dk\end{aligned}\quad (5.51)$$

In which:

$$J_1(kr), (kr) = J_0(kr) - \frac{1}{kr} J_1(kr) \quad (5.52)$$

The  $z$ -dependent functions  $r_n$  and  $l_n$  related to the PSV- and SH-wave respectively, are both included in the equation. Therefore, the unknowns  $A_1$  to  $A_4$  and  $A_5$  &  $A_6$  are solved by the boundary conditions and the PSV- and SH-kernel respectively. The kernel is constructed from  $\mathbf{R}_u(h)$  and  $\mathbf{R}_s(0)$  similar to Eq. (5.27) for the homogeneous case.

$$\begin{aligned}\begin{bmatrix} \mathbf{R}_u(h)^a \\ \mathbf{R}_s(0)^a \end{bmatrix} &= \begin{bmatrix} \begin{bmatrix} ke^{-\alpha h} & ke^{\alpha h} & -\beta e^{-\beta h} & \beta e^{\beta h} \\ -\alpha e^{-\alpha h} & \alpha e^{\alpha h} & ke^{-\beta h} & ke^{\beta h} \\ -2k\mu\alpha & 2k\mu\alpha & \mu(\beta^2 + k^2) & \mu(\beta^2 + k^2) \\ \mu(\beta^2 + k^2) & \mu(\beta^2 + k^2) & -2k\mu\beta & 2k\mu\beta \end{bmatrix} \begin{bmatrix} A_1^a \\ A_2^a \\ A_3^a \\ A_4^a \end{bmatrix} \\ \begin{bmatrix} -e^{-\beta h} & -e^{\beta h} \\ \mu\beta & -\mu\beta \end{bmatrix}_{sh} \begin{bmatrix} A_5^a \\ A_6^a \end{bmatrix} \end{bmatrix} = \frac{F_x}{\pi k r_e} J_1(k r_e) \begin{bmatrix} 0 \\ 0 \\ 1 \\ 0 \end{bmatrix}\end{aligned}\quad (5.53)$$

Eq. (5.53) can find the variables  $A_n$  resulting in:

$$\begin{aligned}\begin{bmatrix} A_1^a \\ A_2^a \\ A_3^a \\ A_4^a \end{bmatrix} &= \begin{bmatrix} 2\beta \left( (\alpha\beta + k^2) e^{h(\alpha-\beta)} + (-\alpha\beta + k^2) e^{h(\alpha+\beta)} - k^2 - \beta^2 \right) k \\ 2k\beta \left( e^{-h(\alpha+\beta)} \alpha\beta - e^{-h(\alpha+\beta)} k^2 - e^{h(-\alpha+\beta)} \alpha\beta - e^{h(-\alpha+\beta)} k^2 + \beta^2 + k^2 \right) \\ -(\alpha\beta + k^2) (\beta^2 + k^2) e^{h(-\alpha+\beta)} + (-\alpha\beta + k^2) (\beta^2 + k^2) e^{h(\alpha+\beta)} + 4\beta\alpha k^2 \\ -(\alpha\beta + k^2) (\beta^2 + k^2) e^{h(\alpha-\beta)} + (-\alpha\beta + k^2) (\beta^2 + k^2) e^{-h(\alpha+\beta)} + 4\beta\alpha k^2 \end{bmatrix} \frac{F_x}{\pi k r_e} \frac{J_1(k r_e)}{\Delta} \\ \begin{bmatrix} A_5^a \\ A_6^a \end{bmatrix} &= \begin{bmatrix} e^{\beta h} \\ -e^{-\beta h} \end{bmatrix} \frac{F_x}{\pi k r_e} \frac{J_1(k r_e)}{\Delta^*}\end{aligned}\quad (5.54)$$

Eq. (5.54) and Eq. (5.52) are substituted into Eq. (5.51) giving the flexibility function in the form of the inverse Hankel transform due to a load in horizontal direction.

$$\begin{aligned}
\tilde{u}_r^a(r, \theta, 0, \omega) &= \frac{F_x}{\pi r_e} \cos(\theta) \int_0^\infty \left\{ \frac{f_{r1}^a(k)}{\Delta(k)} \left( J_0(kr) - \frac{1}{kr} J_1(kr) \right) + \frac{f_{l1}^a(k)}{kr \Delta^*(k)} J_1(kr) \right\} J_1(kr_e) dk, \\
\tilde{u}_\theta^a(r, \theta, 0, \omega) &= \frac{-F_x}{\pi r_e} \sin(\theta) \int_0^\infty \left\{ \frac{f_{r1}^a(k)}{kr \Delta(k)} J_1(kr) + \frac{f_{l1}^a(k)}{\Delta^*(k)} \left( J_0(kr) - \frac{1}{kr} J_1(kr) \right) \right\} J_1(kr_e) dk, \\
\tilde{u}_z^a(r, \theta, 0, \omega) &= \frac{F_x}{\pi r_e} \cos(\theta) \int_0^\infty \frac{f_{r2}^a(k)}{\Delta(k)} J_1(kr_e) J_1(kr) dk
\end{aligned} \tag{5.55}$$

Wherein:

$$\begin{aligned}
f_{r1}^a(k) &= \beta (\beta^2 - k^2) \left( (\alpha \beta + k^2) \left( -e^{h(\alpha-\beta)} + e^{-h(\alpha-\beta)} \right) - \left( e^{h(\alpha+\beta)} - e^{-h(\alpha+\beta)} \right) (-\alpha \beta + k^2) \right) \\
f_{l1}^a(k) &= -e^{\beta h} + e^{-\beta h} \\
f_{r2}^a(k) &= -k \left( (\alpha \beta + k^2) (2\alpha \beta + \beta^2 + k^2) \left( e^{h(\alpha-\beta)} + e^{-h(\alpha-\beta)} \right) \right. \\
&\quad \left. - (-\alpha \beta + k^2) (-2\alpha \beta + \beta^2 + k^2) \left( e^{-h(\alpha+\beta)} + e^{h(\alpha+\beta)} \right) - 4\alpha \beta (\beta^2 + 3k^2) \right)
\end{aligned} \tag{5.56}$$

Similar to the cylindrical symmetric case Eq. (5.55) is extended from the positive integration domain to the full integration domain by making use of the derivation done in appendix A. This is done for both Bessel J functions in Eq. (5.55). Again the condition of (anti)symmetry described in appendix A is fulfilled in all cases. Therefore, Eq. (5.55) is rewritten as:

$$\begin{aligned}
\tilde{u}_r^a(r, \theta, 0, \omega) &= \frac{F_x}{2\pi r_e} \cos(\theta) \int_0^\infty \left\{ \frac{f_{r1}^a(k)}{\Delta(k)} \left( H_0^{(1)}(kr) - \frac{1}{kr} H_1^{(1)}(kr) \right) + \frac{f_{l1}^a(k)}{kr \Delta^*(k)} H_1^{(1)}(kr) \right\} J_1(kr_e) dk, \\
&= \frac{F_x}{2\pi r_e} \cos(\theta) \int_0^\infty \left\{ \frac{f_{r1}^a(k)}{\Delta(k)} \left( J_0(kr) - \frac{1}{kr} J_1(kr) \right) + \frac{f_{l1}^a(k)}{kr \Delta^*(k)} J_1(kr) \right\} H_1^{(1)}(kr_e) dk, \\
\tilde{u}_\theta^a(r, \theta, 0, \omega) &= \frac{-F_x}{2\pi r_e} \sin(\theta) \int_0^\infty \left\{ \frac{f_{r1}^a(k)}{kr \Delta(k)} H_1^{(1)}(kr) + \frac{f_{l1}^a(k)}{\Delta^*(k)} \left( H_0^{(1)}(kr) - \frac{1}{kr} H_1^{(1)}(kr) \right) \right\} J_1(kr_e) dk, \\
&= \frac{-F_x}{2\pi r_e} \sin(\theta) \int_0^\infty \left\{ \frac{f_{r1}^a(k)}{kr \Delta(k)} J_1(kr) + \frac{f_{l1}^a(k)}{\Delta^*(k)} \left( J_0(kr) - \frac{1}{kr} J_1(kr) \right) \right\} H_1^{(1)}(kr_e) dk, \\
\tilde{u}_z^a(r, \theta, 0, \omega) &= \frac{F_x}{2\pi r_e} \cos(\theta) \int_0^\infty \frac{f_{r2}^a(k)}{\Delta(k)} J_1(kr_e) H_1^{(1)}(kr) dk \\
&= \frac{F_x}{2\pi r_e} \cos(\theta) \int_0^\infty \frac{f_{r2}^a(k)}{\Delta(k)} H_1^{(1)}(kr_e) J_1(kr) dk
\end{aligned} \tag{5.57}$$

#### 5.4.1. Contour integration for the antisymmetric load

Eq. (5.57) can be solved by making use of contour integration and the residue theorem similar as in the cylindrical symmetric load case. The integration is split into domains for  $0 < r < r_e$  and  $r_e \leq r$ . The same properties of the Hankel functions and contour integrals are used as explained for Eq. (5.41) and Eq. (5.43). The integrals

in Eq. (5.57) is rewritten as:

$$\begin{aligned}
\tilde{u}_r^a(r, \theta, 0, \omega) &= \frac{F_x}{2\pi r_e} \cos(\theta) \times \begin{cases} 2\pi i \sum_{k=k_m} \frac{f_{r1}^a(k)}{\Delta(k), k} \left( J_0(kr) - \frac{1}{kr} J_1(kr) \right) H_1^{(1)}(kr_e) \\ + 2\pi i \sum_{k=k_{sh}} \frac{f_{r1}^a(k)}{kr \Delta^*(k), k} J_1(kr) H_1^{(1)}(kr_e) - \int_{C_0} - \int_{C_\infty} & 0 < r < r_e \\ 2\pi i \sum_{k=k_m} \frac{f_{r1}^a(k)}{\Delta(k), k} \left( H_0^{(1)}(kr) - \frac{1}{kr} H_1^{(1)}(kr) \right) J_1(kr_e) \\ + 2\pi i \sum_{k=k_{sh}} \frac{f_{r1}^a(k)}{kr \Delta^*(k), k} H_1^{(1)}(kr) J_1(kr_e) - \int_{C_0} - \int_{C_\infty} & r_e \leq r \end{cases} \\
\tilde{u}_\theta^a(r, \theta, 0, \omega) &= \frac{-F_x}{2\pi r_e} \sin(\theta) \times \begin{cases} 2\pi i \sum_{k=k_m} \frac{f_{r1}^a(k)}{kr \Delta(k), k} J_1(kr) H_1^{(1)}(kr_e) \\ + 2\pi i \sum_{k=k_{sh}} \frac{f_{r1}^a(k)}{\Delta^*(k), k} \left( J_0(kr) - \frac{1}{kr} J_1(kr) \right) H_1^{(1)}(kr_e) \\ - \int_{C_0} - \int_{C_\infty} & 0 < r < r_e \\ 2\pi i \sum_{k=k_m} \frac{f_{r1}^a(k)}{kr \Delta(k), k} H_1^{(1)}(kr) J_1(kr_e) \\ + 2\pi i \sum_{k=k_{sh}} \frac{f_{r1}^a(k)}{\Delta^*(k), k} \left( H_0^{(1)}(kr) - \frac{1}{kr} H_1^{(1)}(kr) \right) J_1(kr_e) \\ - \int_{C_0} - \int_{C_\infty} & r_e \leq r \end{cases} \\
\tilde{u}_z^a(r, \theta, 0, \omega) &= \frac{F_x}{2\pi r_e} \cos(\theta) \times \begin{cases} 2\pi i \sum_{k=k_m} \frac{f_{r2}^a(k)}{\Delta(k), k} H_1^{(1)}(kr_e) J_1(kr) - \int_{C_\infty} & 0 < r < r_e \\ 2\pi i \sum_{k=k_m} \frac{f_{r2}^a(k)}{\Delta(k), k} J_1(kr_e) H_1^{(1)}(kr) - \int_{C_\infty} & r_e \leq r \end{cases}
\end{aligned} \tag{5.58}$$

Eq. (5.58) only holds for the condition that  $\Im(k) > 0$ . The integration along the contour vanish when the radius of the integration path approaches infinity. Therefore,  $\int_{C_\infty} = 0$ . There are four types of singularities at  $k = 0$  in Eq. (5.57), since  $\lim_{z \rightarrow 0} \frac{1}{z} J_1(az) = \frac{a}{2}$  and  $J_0(z) = 1$ . Integration around the singularities is applied:

$$\begin{aligned}
\int_{C_{0-1}} &= \lim_{k \rightarrow 0} \int_{\pi}^0 \frac{f_i^a(k)}{\Delta_i(k)} J_0(kr) H_1^{(1)}(kr_e) dk & 0 < r < r_e \\
\int_{C_{0-2}} &= \lim_{k \rightarrow 0} \int_{\pi}^0 \frac{f_i^a(k)}{kr \Delta_i(k)} J_1(kr) H_1^{(1)}(kr_e) dk & 0 < r < r_e \\
\int_{C_{0-3}} &= \lim_{k \rightarrow 0} \int_{\pi}^0 \frac{f_i^a(k)}{kr \Delta_i(k)} J_1(kr_e) H_1^{(1)}(kr) dk & r_e \leq r
\end{aligned} \tag{5.59}$$

Again, making use of the substitution for  $k$  as performed in Eq. (5.44), the integration around the singularities results in:

$$\begin{aligned}
\int_{C_{0-1}} &= \lim_{\delta \rightarrow 0} \int_{\pi}^0 \frac{f_i^a(\delta e^{i\phi})}{\Delta_i(\delta e^{i\phi})} J_0(\delta e^{i\phi} r) H_1^{(1)}(\delta e^{i\phi} r_e) i \delta e^{i\phi} d\phi & 0 < r < r_e \\
&= \lim_{\delta \rightarrow 0} \int_{\pi}^0 \frac{f_i^a(0)}{\Delta_i(0)} H_1^{(1)}(\delta e^{i\phi} r_e) i \delta e^{i\phi} d\phi & 0 < r < r_e \\
\int_{C_{0-2}} &= \lim_{\delta \rightarrow 0} \int_{\pi}^0 \frac{f_i^a(\delta e^{i\phi})}{\delta e^{i\phi} r \Delta_i(\delta e^{i\phi})} J_1(\delta e^{i\phi} r) H_1^{(1)}(\delta e^{i\phi} r_e) i \delta e^{i\phi} d\phi & 0 < r < r_e \\
&= \lim_{\delta \rightarrow 0} \int_{\pi}^0 \frac{f_i^a(0)}{2\Delta_i(0)} H_1^{(1)}(\delta e^{i\phi} r_e) i \delta e^{i\phi} d\phi & 0 < r < r_e \\
\int_{C_{0-3}} &= \lim_{\delta \rightarrow 0} \int_{\pi}^0 \frac{f_i^a(\delta e^{i\phi})}{\delta e^{i\phi} r \Delta_i(\delta e^{i\phi})} J_1(\delta e^{i\phi} r_e) H_1^{(1)}(\delta e^{i\phi} r) i \delta e^{i\phi} d\phi & r_e \leq r \\
&= \lim_{\delta \rightarrow 0} \int_{\pi}^0 \frac{r_e f_i^a(0)}{2r \Delta_i(0)} H_1^{(1)}(\delta e^{i\phi} r) i \delta e^{i\phi} d\phi & r_e \leq r
\end{aligned} \tag{5.60}$$

The series expansion of the  $H_1^{(1)}$  is performed in Eq. (5.46) and results in:

$$\lim_{\delta \rightarrow 0} \int_{\pi}^0 H_1^{(1)}(\delta e^{i\phi} r_{(e)}) i \delta e^{i\phi} d\phi = \int_{\pi}^0 \frac{2}{r_{(e)} \pi} d\phi \tag{5.61}$$

Substituting Eq. (5.61) into Eq. (5.60) gives:

$$\begin{aligned}
\int_{C_{0-1}} &= \int_{\pi}^0 \frac{2f_i^a(0)}{r_e \pi \Delta_i(0)} d\phi = \left[ \frac{2f_i^a(0)}{r_e \pi \Delta_i(0)} \phi \right]_{\pi}^0 = -\frac{2f_i^a(0)}{r_e \Delta_i(0)} & 0 < r < r_e \\
\int_{C_{0-2}} &= \int_{\pi}^0 \frac{f_i^a(0)}{r_e \pi \Delta_i(0)} d\phi = \left[ \frac{f_i^a(0)}{r_e \pi \Delta_i(0)} \phi \right]_{\pi}^0 = -\frac{f_i^a(0)}{r_e \Delta_i(0)} & 0 < r < r_e \\
\int_{C_{0-3}} &= \int_{\pi}^0 \frac{r_e f_i^a(0)}{r^2 \pi \Delta_i(0)} d\phi = \left[ \frac{r_e f_i^a(0)}{r^2 \pi \Delta_i(0)} \phi \right]_{\pi}^0 = -\frac{r_e f_i^a(0)}{r^2 \Delta_i(0)} & r_e \leq r
\end{aligned} \tag{5.62}$$

Through the substitution of Eq. (5.62) in Eq. (5.58), the final expression for the displacements are obtained.

$$\begin{aligned}
\tilde{u}_r^a(r, \theta, 0, \omega) &= \frac{F_x}{2\pi r_e} \cos(\theta) \times \begin{cases} 2\pi i \sum_{k=k_m} \frac{f_{r1}^a(k)}{\Delta(k)_k} \left( J_0(kr) - \frac{1}{kr} J_1(kr) \right) H_1^{(1)}(kr_e) \\ + 2\pi i \sum_{k=k_{sh}} \frac{f_{r1}^a(k)}{kr \Delta^*(k)_k} J_1(kr) H_1^{(1)}(kr_e) \\ + \frac{f_{r1}^a(0)}{r_e \Delta(0)} + \frac{f_{r1}^a(0)}{r_e \Delta^*(0)} & 0 < r < r_e \\ 2\pi i \sum_{k=k_m} \frac{f_{r1}^a(k)}{\Delta(k)_k} \left( H_0^{(1)}(kr) - \frac{1}{kr} H_1^{(1)}(kr) \right) J_1(kr_e) \\ + 2\pi i \sum_{k=k_{sh}} \frac{f_{r1}^a(k)}{kr \Delta^*(k)_k} H_1^{(1)}(kr) J_1(kr_e) \\ - \frac{r_e f_{r1}^a(0)}{r^2 \Delta(0)} + \frac{r_e f_{r1}^a(0)}{r^2 \Delta^*(0)} & r_e \leq r \end{cases} \\
\tilde{u}_\theta^a(r, \theta, 0, \omega) &= \frac{-F_x}{2\pi r_e} \sin(\theta) \times \begin{cases} 2\pi i \sum_{k=k_m} \frac{f_{r1}^a(k)}{kr \Delta(k)_k} J_1(kr) H_1^{(1)}(kr_e) \\ + 2\pi i \sum_{k=k_{sh}} \frac{f_{r1}^a(k)}{\Delta^*(k)_k} \left( J_0(kr) - \frac{1}{kr} J_1(kr) \right) H_1^{(1)}(kr_e) \\ + \frac{f_{r1}^a(0)}{r_e \Delta(0)} + \frac{f_{r1}^a(0)}{r_e \Delta^*(0)} & 0 < r < r_e \\ 2\pi i \sum_{k=k_m} \frac{f_{r1}^a(k)}{kr \Delta(k)_k} H_1^{(1)}(kr) J_1(kr_e) \\ + 2\pi i \sum_{k=k_{sh}} \frac{f_{r1}^a(k)}{\Delta^*(k)_k} \left( H_0^{(1)}(kr) - \frac{1}{kr} H_1^{(1)}(kr) \right) J_1(kr_e) \\ + \frac{r_e f_{r1}^a(0)}{r^2 \Delta(0)} - \frac{r_e f_{r1}^a(0)}{r^2 \Delta^*(0)} & r_e \leq r \end{cases} \\
\tilde{u}_z^a(r, \theta, 0, \omega) &= \frac{F_x}{2\pi r_e} \cos(\theta) \times \begin{cases} 2\pi i \sum_{k=k_m} \frac{f_{r2}^a(k)}{\Delta(k)_k} H_1^{(1)}(kr_e) J_1(kr) & 0 < r < r_e \\ 2\pi i \sum_{k=k_m} \frac{f_{r2}^a(k)}{\Delta(k)_k} J_1(kr_e) H_1^{(1)}(kr) & r_e \leq r \end{cases}
\end{aligned} \tag{5.63}$$

The displacements in x and y, in Cartesian coordinates, can be obtained by transforming Eq. (5.63) through straight forward multiplication with a sin and cosine.

$$\begin{aligned}
\tilde{u}_x &= \cos(\theta) \tilde{u}_r - \sin(\theta) \tilde{u}_\theta \\
\tilde{u}_y &= \sin(\theta) \tilde{u}_r + \cos(\theta) \tilde{u}_\theta
\end{aligned} \tag{5.64}$$

A stiffness matrix is constructed similar to the 2D case, by Eq. (3.58) to Eq. (3.60).

## 5.5. Flexibility functions

The flexibility functions in the 3D case are similar to these obtained in the 2D case. The flexibility for the cylindrical symmetric load case, i.e. a vertical load, is shown in figure 5.3 and figure 5.4. Figure 5.8 to figure 5.11 show the flexibility function related to the horizontal antisymmetric load in  $x$  ( $\theta = 0$ ). The radius and frequency corresponding to the figures is respectively 1 m and 3.09 Hz. The flexibility functions are compared to the flexibility function of the 2D case. Obviously, for the same frequencies, the period of the waves is equal. It is noticeable that the amplitude in 2D does not decay in distance, while in 3D the amplitude of the propagating waves reduces quickly. This is due to the wave energy spreading over the surface (2D). Instead like in the 2D case, the waves propagate along a line (1D).

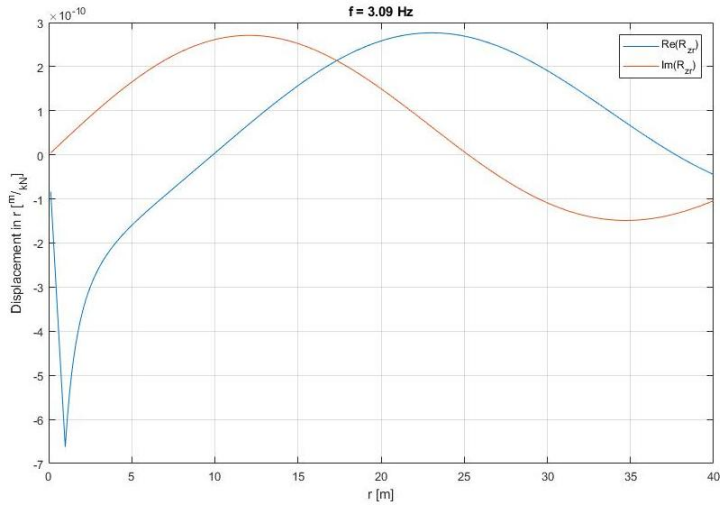


Figure 5.3: Flexibility function for the displacement in  $r$  due to a vertical load

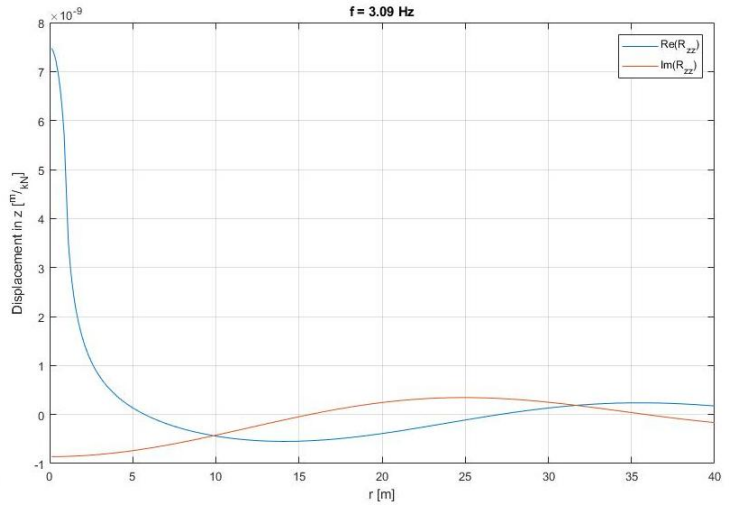


Figure 5.4: Flexibility function for the displacement in  $z$  due to a vertical load

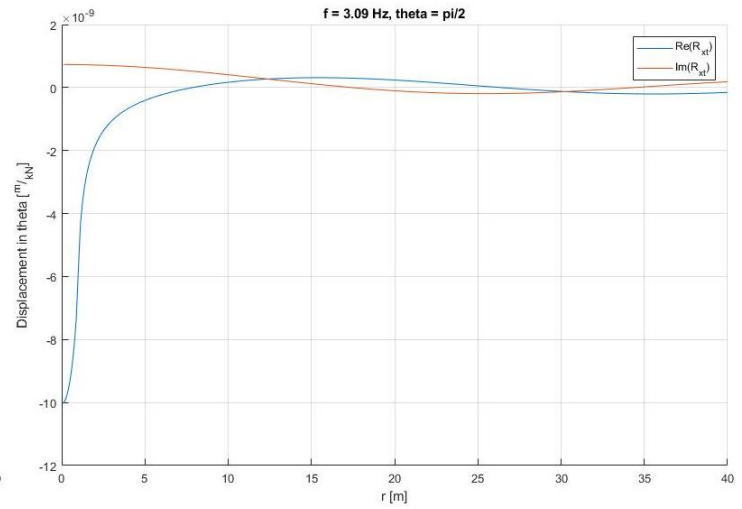
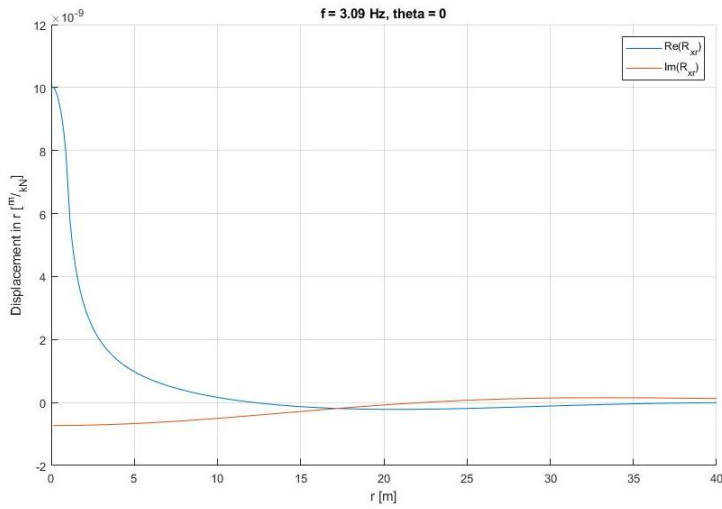


Figure 5.5: Flexibility function for the displacement in  $r$  due to a horizontal load in  $x$  ( $\theta = 0$ )

Figure 5.6: Flexibility function for the displacement in  $\theta$  due to a horizontal load in  $x$  ( $\theta = 0$ )

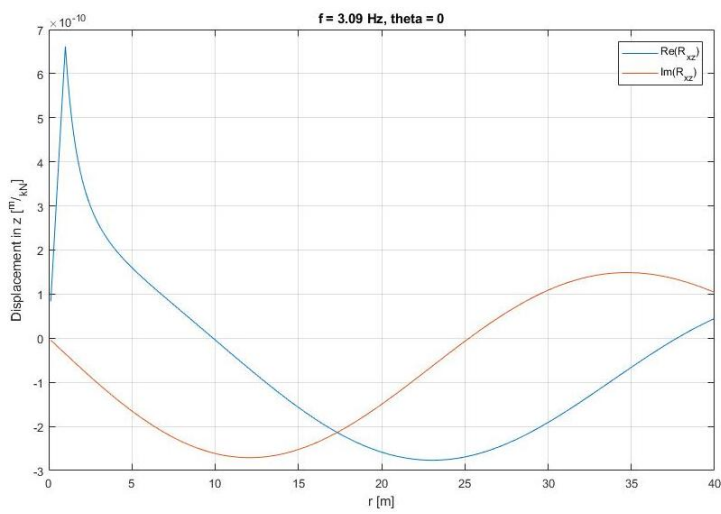


Figure 5.7: Flexibility function for the displacement in  $z$  due to a horizontal load in  $x$  ( $\theta = 0$ )

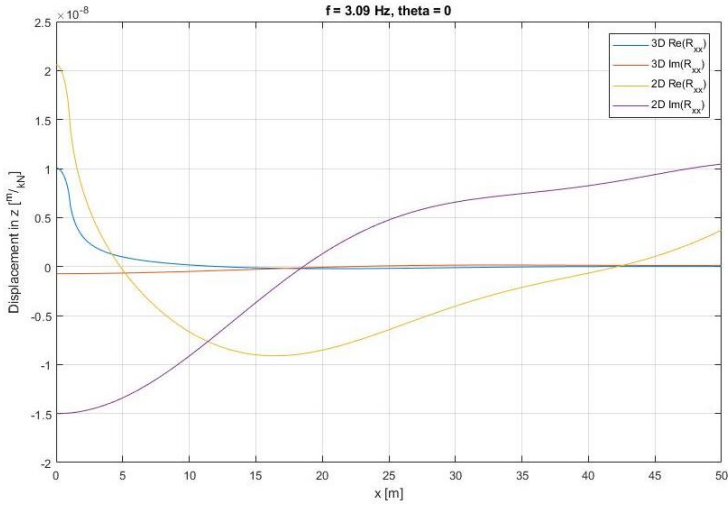


Figure 5.8: Comparison of the flexibility function  $R_{zz}$  in 3D and 2D for the frequency 3.09 Hz.

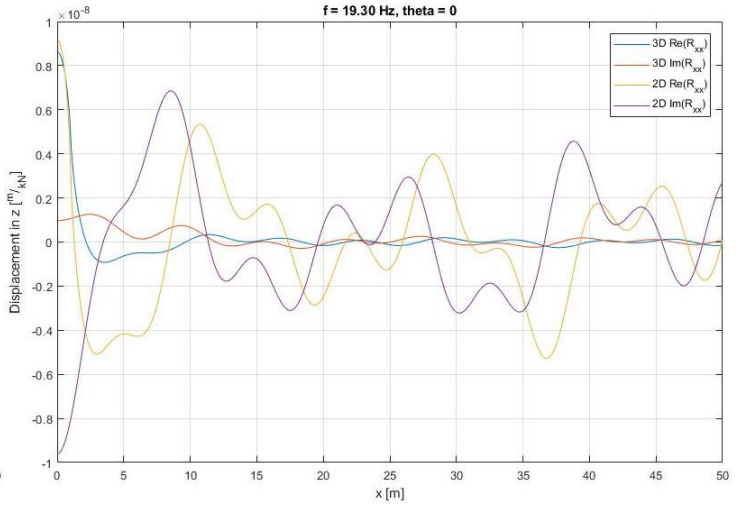


Figure 5.9: Comparison of the flexibility function  $R_{zz}$  in 3D and 2D for the frequency 19.30 Hz.

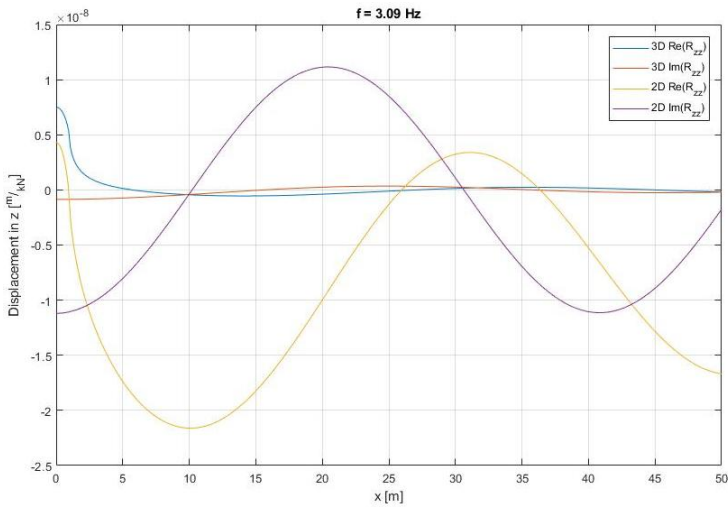


Figure 5.10: Comparison of the flexibility function  $R_{xx}$  in 3D and 2D for the frequency 3.09 Hz.

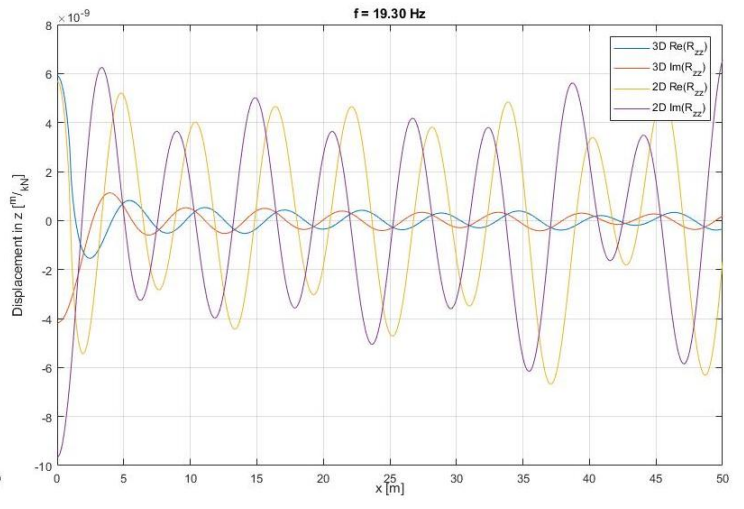


Figure 5.11: Comparison of the flexibility function  $R_{xx}$  in 3D and 2D for the frequency 19.30 Hz.

## 5.6. Validation

The 3D model is validated with work of Gazetas (1983) with adapted earlier work of Kausel (1974). Both static stiffness and dynamic stiffness are compared. Both the stiffness of a discretized rigid plate and a single element are determined. To determine the stiffness and flexibility of a single element, the average displacement over the area is determined. The equivalent vertical flexibility of a single element  $R_{zz}$  is found by:

$$\frac{1}{\pi r_e^2} \int_0^{r_e} \int_0^{2\pi} r \tilde{u}_z^s(r, \theta, \omega) d\theta dr = \frac{2}{r_e^2} \int_0^{r_e} r \tilde{u}_z^s(r, \theta, \omega) dr \quad (5.65)$$

Substituting Eq. (5.47) into the integral results in:

$$\begin{aligned} \frac{2}{r_e^2} \int_0^{r_e} r \tilde{u}_z^s(r, \theta, \omega) dr &= \frac{2F_z}{r_e^2} \int_0^{r_e} r \frac{i}{r_e} \sum_{k=k_m} \frac{f_{r_2}^s(k)}{\Delta(k, k)} H_1^{(1)}(kr_e) J_0(kr) + r \frac{f_{r_2}^s(0)}{\pi r_e^2 \Delta(0)} dr \\ &= \frac{2F_z}{r_e^2} \left[ r \frac{i}{r_e} \sum_{k=k_m} \frac{f_{r_2}^s(k)}{\Delta(k, k)} H_1^{(1)}(kr_e) \frac{J_1(kr)}{k} + r^2 \frac{f_{r_2}^s(0)}{2\pi r_e^2 \Delta(0)} \right]_0^{r_e} \\ &= \frac{2F_z}{r_e^2} \left( i \sum_{k=k_m} \frac{f_{r_2}^s(k)}{\Delta(k, k)} H_1^{(1)}(kr_e) \frac{J_1(kr_e)}{k} + \frac{f_{r_2}^s(0)}{2\pi \Delta(0)} \right) \end{aligned} \quad (5.66)$$

The same procedure is followed for the horizontal flexibility  $R_{xx}$ :

$$\begin{aligned} \frac{1}{\pi r_e^2} \int_0^{r_e} \int_0^{2\pi} r \tilde{u}_x^a(r, \theta, \omega) d\theta dr &= \frac{1}{\pi r_e^2} \int_0^{r_e} \int_0^{2\pi} r (\tilde{u}_r^a(r, \theta, \omega) \cos(\theta) - \tilde{u}_\theta^a(r, \theta, \omega) \sin(\theta)) d\theta dr \\ &= \frac{1}{\pi r_e^2} \int_0^{r_e} \int_0^{2\pi} r (\tilde{U}_r^a \cos^2(\theta) + \tilde{U}_\theta^a \sin^2(\theta)) d\theta dr \\ &= \frac{1}{r_e^2} \int_0^{r_e} r (\tilde{U}_r^a + \tilde{U}_\theta^a) dr \end{aligned} \quad (5.67)$$

In which  $\tilde{U}_r^a$  and  $\tilde{U}_\theta^a$  are the amplitudes of the functions  $\tilde{u}_r^a$  and  $\tilde{u}_\theta^a$  without the factors  $\cos(\theta)$  and  $\sin(\theta)$ . The amplitudes are determined from Eq. (5.63):

$$\begin{aligned} \tilde{U}_r^a &= F_x \left( \frac{i}{r_e} \sum_{k=k_m} \frac{f_{r_1}^a(k)}{\Delta(k, k)} \left( J_0(kr) - \frac{1}{kr} J_1(kr) \right) H_1^{(1)}(kr_e) + \frac{i}{r_e} \sum_{k=k_{sh}} \frac{f_{l_1}^a(k)}{kr \Delta^*(k, k)} J_1(kr) H_1^{(1)}(kr_e) + \frac{f_{r_1}^a(0)}{2\pi r_e^2 \Delta(0)} + \frac{f_{l_1}^a(0)}{2\pi r_e^2 \Delta^*(0)} \right) \\ \tilde{U}_\theta^a &= F_x \left( \frac{i}{r_e} \sum_{k=k_m} \frac{f_{r_1}^a(k)}{kr \Delta(k, k)} J_1(kr) H_1^{(1)}(kr_e) + \frac{i}{r_e} \sum_{k=k_{sh}} \frac{f_{l_1}^a(k)}{\Delta^*(k, k)} \left( J_0(kr) - \frac{1}{kr} J_1(kr) \right) H_1^{(1)}(kr_e) + \frac{f_{r_1}^a(0)}{2\pi r_e^2 \Delta(0)} + \frac{f_{l_1}^a(0)}{2\pi r_e^2 \Delta^*(0)} \right) \end{aligned} \quad (5.68)$$

The integration is solved by:

$$\begin{aligned} \int_0^{r_e} \int_0^{2\pi} r \tilde{u}_x^a(r, \theta, \omega) d\theta dr &= \frac{F_x}{r_e^2} \int_0^{r_e} \frac{ir}{r_e} \sum_{k=k_m} \frac{f_{r_1}^a(k)}{\Delta(k, k)} J_0(kr) H_1^{(1)}(kr_e) + r \frac{f_{r_1}^a(0)}{\pi r_e^2 \Delta(0)} \\ &\quad + \frac{ir}{r_e} \sum_{k=k_{sh}} \frac{f_{l_1}^a(k)}{\Delta^*(k, k)} J_0(kr) H_1^{(1)}(kr_e) + r \frac{f_{l_1}^a(0)}{\pi r_e^2 \Delta^*(0)} dr \\ &= \frac{F_x}{r_e^2} \left[ \frac{ir}{r_e} \sum_{k=k_m} \frac{f_{r_1}^a(k)}{\Delta(k, k)} \frac{J_1(kr)}{k} H_1^{(1)}(kr_e) + r^2 \frac{f_{r_1}^a(0)}{2\pi r_e^2 \Delta(0)} \right. \\ &\quad \left. + \frac{ir}{r_e} \sum_{k=k_{sh}} \frac{f_{l_1}^a(k)}{\Delta^*(k, k)} \frac{J_1(kr)}{k} H_1^{(1)}(kr_e) + r^2 \frac{f_{l_1}^a(0)}{2\pi r_e^2 \Delta^*(0)} \right]_0^{r_e} \\ &= \frac{F_x}{r_e^2} \left( i \sum_{k=k_m} \frac{f_{r_1}^a(k)}{\Delta(k, k)} \frac{J_1(kr_e)}{k} H_1^{(1)}(kr_e) + \frac{f_{r_1}^a(0)}{2\pi \Delta(0)} \right. \\ &\quad \left. + i \sum_{k=k_{sh}} \frac{f_{l_1}^a(k)}{\Delta^*(k, k)} \frac{J_1(kr_e)}{k} H_1^{(1)}(kr_e) + \frac{f_{l_1}^a(0)}{2\pi \Delta^*(0)} \right) \end{aligned} \quad (5.69)$$

### 5.6.1. Static stiffness

The static stiffness derived by Kausel (1974) for a circular rigid foundation on a linear elastic single layer over bedrock with the corresponding range of validity are:

$$\begin{aligned}
 K_z &= \frac{F_z}{u_z} = \frac{4\mu r_p}{1-\nu} \left(1 + 1.28 \frac{r_p}{h}\right) & 2 < \frac{h}{r_p} \\
 K_x &= \frac{F_x}{u_x} = \frac{8\mu r_p}{2-\nu} \left(1 + \frac{r_p}{2h}\right) & 1 < \frac{h}{r_p} \\
 K_r &= \frac{M_y}{\varphi_y} = \frac{8\mu r_p^3}{3(1-\nu)} \left(1 + \frac{r_p}{3h}\right) & 1 < \frac{h}{r_p} \leq 4
 \end{aligned} \tag{5.70}$$

The equations give a good approximation of the stiffness, even outside the range of validity. The rigid foundation is simulated by applying a constant displacement on the stiffness matrix constructed from the flexibility functions Eq. (5.58) and Eq. (5.63). The static case is approximated by the obtained model with a frequency of 0.39Hz. The stiffness is determined almost exactly the same as in the 2D case, shown in figure 3.15. The only difference is that the integration domain is changed from the width of the strip, to the interaction area of the circular plate. The obtained model is compared to stiffness from Eq. (5.70) in table 5.1 to table 5.1. The vertical and horizontal stiffness of the model are within 4% of the expected stiffness, the rocking stiffness of the model is 8-9% less than the stiffness expected from Eq. (5.70). Obviously, the stiffness of a single element describing the plate is less than the stiffness of a rigid plate. However, the reduction in stiffness is only about 8-9%. In general, the 3D model responds properly, validated with earlier work of Gazetas (1983). The 3D soil model improved the horizontal stiffness since, contrary to the plane-strain case, the 3D model performs as expected.

$h/r_p$	Gazetas	Rigid plate		Single element	
2	3.42e9	3.44e9	1%	3.16e9	-7%
3	1.98e9	1.92e9	-3%	1.77e9	-11%
4	1.38e9	1.32e9	-4%	1.22e9	-11%
25	1.75e8	1.69e8	-3%	1.59e8	-9%

Table 5.1: Difference of the vertical stiffness  $K_z$  of a rigid cylindrical plate and single element compared to Eq. (5.70)

$h/r_p$	Gazetas	Rigid plate		Single element	
2	1.95e9	1.88e9	-4%	1.75e9	-11%
3	1.22e9	1.17e9	-4%	1.09e9	-10%
4	8.79e8	8.49e8	-3%	7.93e8	-10%
25	1.28e8	1.24e8	-3%	1.17e8	-8%

Table 5.2: Difference of the horizontal stiffness  $K_x$  of a rigid cylindrical plate and single element compared to Eq. (5.70)

$h/r_p$	Gazetas	Rigid plate	
2	2.35e11	2.16e11	-8%
3	6.79e10	6.18e10	-9%
4	2.83e10	2.59e10	-8%
25	1.12e8	1.03e8	-8%

Table 5.3: Difference of the rocking stiffness  $K_r$  of a rigid cylindrical plate compared to Eq. (5.70)

### 5.6.2. Dynamic stiffness

The dynamic stiffness of a rigid plate and single element on the soil model are compared with the results obtained in Gazetas (1983). It is noted that the material properties do not exactly match. Therefore, trends are compared. The two differences are firstly the Poisson's ratio differs between the model and Gazetas (1983).

The Poisson's ratio is respectively 0.40 and 0.33. Secondly, the soil of Gazetas (1983) includes 5% material damping, contrary to the soil model developed in this thesis, which has no damping.

The same steps are taken as in the 2D case explained in section 3.8. The stiffness and damping ratio are described by Eq. (3.66) and the normalized frequency by Eq. (3.65). The resonance frequencies of a single layer corresponding to the PSV-wave are equal to those found in section 3.8. The first and second resonance frequency found correspond respectively to the frequency of the fundamental shear mode and the frequency of the fundamental compressional mode of the soil layer. The first three resonance frequencies for a single layer for different  $h/r_p$  ratios are repeated in table 5.4. Due to the hysteretic damping in the model of (Gazetas,

$h/r_p$	$a_{0,1} = a_{0,s1}$	$a_{0,2} = a_{0,p1}$	$a_{0,3}$
3	0.52	1.28	1.57
4	0.39	0.96	1.18
25	0.06	0.15	0.19

Table 5.4: First three natural frequencies of a single layer

1983), it is expected that that model will be less sensitive to the resonance pattern and will have more gradual fluctuation of the stiffness for different frequencies.

In figure 5.12 to figure 5.17 the dynamic dependence of the stiffness and damping is compared for different ratios  $\frac{h}{r_p}$ .

### Vertical stiffness and damping

Similar to the 2D case, the vertical stiffness damping and stiffness are strongly sensitive to variation in frequency. The first steep decay in stiffness is found at the second resonance frequency of the layer. Figure 5.12 and figure 5.13 show respectively the frequency dependent normalized vertical stiffness and damping. The second resonance frequency corresponding to the frequency of the fundamental compressional mode of the soil layer is indicated with the vertical dashed lines. Therefore, the reduction of the stiffness for this frequency can be expected, since the layer is loaded in compression. The developed model behaves by the same trends as the reference model from Gazetas (1983). However, it is more sensitive to damping what can be declared by the absence of material damping.

### Horizontal stiffness and damping

The horizontal stiffness and damping are similar to the vertical stiffness and damping strongly sensitive to a variation in frequency. Figure 5.14 and figure 5.15 show the horizontal stiffness and damping, the vertical lines show the first and second resonance frequency of the soil layer. This is especially noticeable for higher frequencies. A decrease in stiffness is observed at the first and second resonance frequency corresponding to the fundamental shear and compression mode of the soil. Contrary to the vertical stiffness, the horizontal stiffness is influenced by the fundamental shear mode, which is reasonable since the load is parallel to the bedrock. The first damping is observed after the first resonance frequency. Both stiffness and damping match the behavior of the reference for low frequencies, independent of the  $\frac{h}{r_p}$  ratio. However, the developed model is more sensitive to higher frequencies, plausibly due the absence of material damping.

### Rocking stiffness and damping

Figure 5.16 and figure 5.17 show the rocking stiffness and damping, the vertical lines show the first and second resonance frequency of the soil layer. The rocking stiffness is less sensitive for variation in frequency and a correlation to the resonance frequencies of the soil layer are not observed. The rocking stiffness and damping of the developed model behaves similar as derived in Gazetas (1983). However, the damping continues increasing for higher frequencies.

Overall, the model behaves as expected. The reduction in stiffness at a specific frequency can be declared for the horizontal and vertical case. The behavior of the model follows, especially for low frequencies, the same trends as the reference model of Gazetas (1983), even despite slightly different material properties.

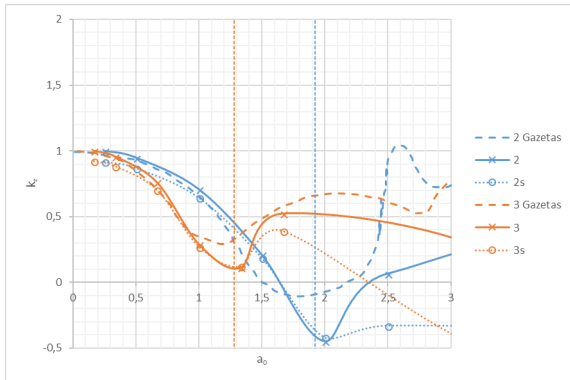


Figure 5.12: Normalized stiffness coefficient  $k_z$ .

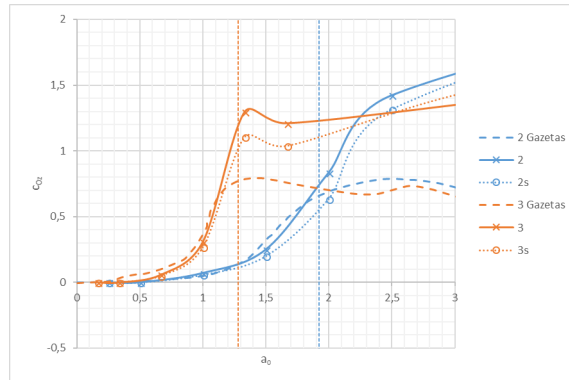


Figure 5.13: Normalized damping coefficient  $c_{0z}$ .

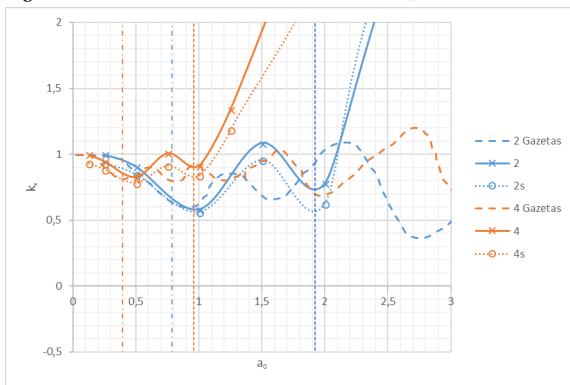


Figure 5.14: Normalized stiffness coefficient  $k_x$ .

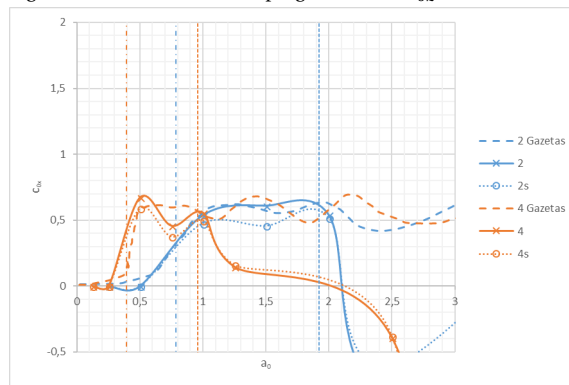


Figure 5.15: Normalized damping coefficient  $c_{0x}$ .

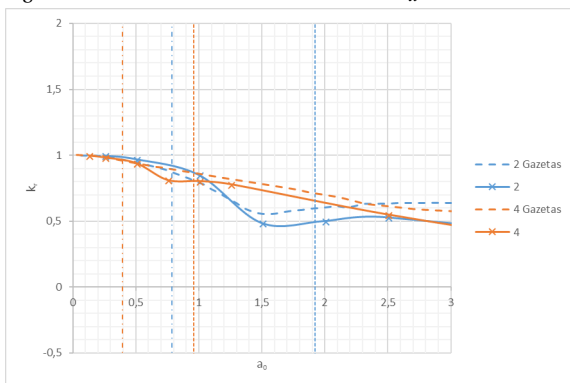


Figure 5.16: Normalized stiffness coefficient  $k_r$ .

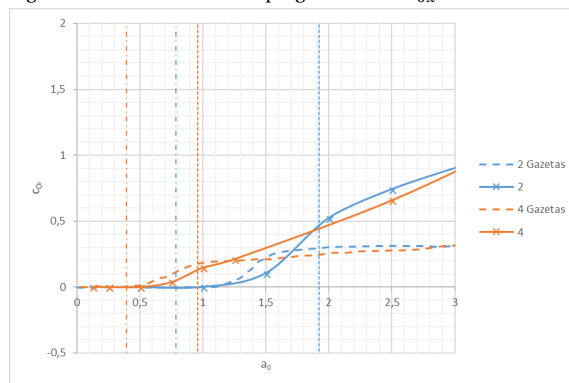


Figure 5.17: Normalized damping coefficient  $c_{0r}$ .



# 6

## 3D Soil structure interaction

This chapter describes how the interaction between soil and structure is established for a circular inextensible plate on linear elastic soil. The deformation of the foundation plate is limited to cylindrical symmetrical and antisymmetry out-of-plane motions, since only circumferential wavenumber  $n = 0$  and  $n = 1$  are considered. The load is applied in terms of an initial harmonic displacement field. These circumferential wavenumbers are the most likely dominant. In most construction codes only these circumferential modes are considered. The plate is assumed to be a thin plate, considering only bending deformation. Furthermore, the plate is inextensible in-plane.

### 6.1. SSI of a plate in cylindrical coordinates

The inextensible Kirchoff-Love plate (pure bending) is chosen to have a height of 1 meter and a 5 meter radius. The soil properties and material properties of the plate are consistent with the 2D case (table 3.1, table 4.1). A scheme of the 3D SSI case is shown in figure 6.1. The governing equations for the soil structure interaction are comparable with Eq. (4.1) to Eq. (4.6) from the 2D case. The only difference with the 2D case is that the

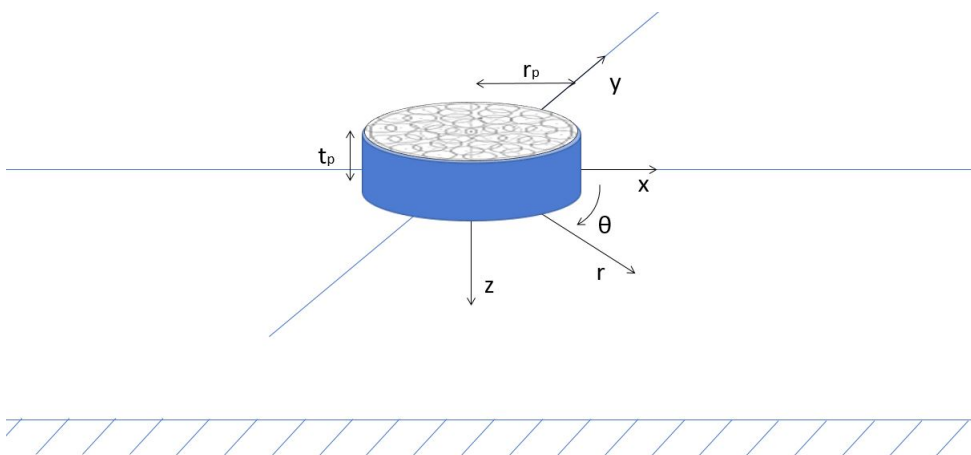


Figure 6.1: Schematization of a finite circular plate supported on linear elastic soil in cylindrical coordinates

beam equations are now replaced with plate equations. This yields the following set of equations:

$$D\nabla^4 \tilde{u}_{z,p} - \rho_p t_p \omega^2 \tilde{u}_{z,p} + \sum_m \tilde{S}_{zm,s} = \sum_m \tilde{S}_{izm,s} \quad (6.1)$$

$$M_{p,r=r_p} = 0 \quad (6.2)$$

$$V_{p,r=r_p} = 0 \quad (6.3)$$

$$u_{x,p}(r, \theta) = \text{constant for } 0 \leq r \leq r_p, \quad 0 \leq \theta \leq 2\pi \quad (6.4)$$

$$-\omega^2 \rho_p A_p L_p \tilde{u}_{x,p} + \sum_m \tilde{S}_{xm,s} = \sum_m \tilde{S}_{ixm,s} \quad (6.5)$$

$$u_{z,p} = u_{z,s}, \quad u_{x,p} = u_{x,s} \quad (6.6)$$

Indices  $_{,p}$  refer to the plate and indices  $_{,s}$  to the soil. The summation over  $m$  refers to a summation of, in this case initial and reaction forces, on element  $m$ . The decomposition of the stiffness matrix is executed in the same manner as in section 4.3. Furthermore, is the horizontal equation of motion reduced to a single degree of freedom system, as performed in the 2D case. The force components are rewritten as:

$$\begin{aligned} \tilde{S}_{ix,s} &= \sum_m \tilde{S}_{ixm,s} = \mathbf{K}_x \tilde{\mathbf{u}}_{i,s} \\ \tilde{S}_{izm,s} &= \mathbf{K}_z \tilde{\mathbf{u}}_{i,s} \\ \tilde{S}_{xm,s} &= \mathbf{K}_{xx} \tilde{\mathbf{u}}_{x,s} + \mathbf{K}_{xz} \tilde{\mathbf{u}}_{zm,s} \\ \tilde{S}_{zm,s} &= \mathbf{K}_{z-u_z} \tilde{\mathbf{u}}_{zm,s} + \mathbf{C}_x \tilde{S}_{ix,s} \end{aligned} \quad (6.7)$$

With:

$$\begin{aligned} \tilde{u}_{x,s} &= \frac{\tilde{S}_{ix,s}}{\sum_m \mathbf{K}_{xx} - \omega^2 \rho_b A_b L_b} - \frac{\sum_m \mathbf{K}_{xz} \tilde{\mathbf{u}}_{zm,s}}{\sum_m \mathbf{K}_{xx} - \omega^2 \rho_b A_b L_b} \\ \mathbf{C}_x &= \frac{\mathbf{K}_{zx,[n,1]}}{\sum_n \mathbf{K}_{xx} - \omega^2 \rho_b A_b L_b} \end{aligned} \quad (6.8)$$

### 6.1.1. Free-edge plate equations

The governing plate equations for plates are described in (Rao, 1999) are used and validated for. Starting from the free-edge boundary conditions to describe the free vibrations of the plate. The equations of motion of the plate is:

$$D\nabla^4 u_{z,p} + \rho_p t_p \ddot{u}_{z,p} = 0 \quad (6.9)$$

In which:

$$D = \frac{Eh^3}{12(1-\nu^2)} \quad (6.10)$$

And since for harmonic motion  $\ddot{u}_{z,p} = -\omega^2 \tilde{u}_{z,p}$ . The equation of motion is rewritten as:

$$(\nabla^2 + \beta^2)(\nabla^2 - \beta^2) \tilde{u}_{z,p} = 0 \quad (6.11)$$

With:

$$\beta^2 = \sqrt{\frac{\rho_p t_p}{D}} \omega \quad (6.12)$$

The solution to equation Eq. (6.11) is written as:

$$\begin{aligned} \tilde{u}_{z,p} &= [A_1 J_n(\beta r) + A_2 Y_n(\beta r) + A_3 I_n(\beta r) + A_4 K_n(\beta r)] \sin(n\theta) \\ &+ [B_1 J_n(\beta r) + B_2 Y_n(\beta r) + B_3 I_n(\beta r) + B_4 K_n(\beta r)] \cos(n\theta) \end{aligned} \quad (6.13)$$

$J_n$  and  $Y_n$  are Bessel functions of order  $n$  and  $I_n$  and  $K_n$  are modified Bessel functions of order  $n$ .  $K_n$  and  $Y_n$  approach infinity as  $r$  approaches zero. Since  $\tilde{u}_{z,p}$  is finite for all  $r$ ,  $A_2$ ,  $A_4$ ,  $B_2$  and  $B_4$  are zero. Therefore, the solution for the displacement is written as:

$$\tilde{u}_{z,p} = \tilde{W}_n [J_n(\beta r) + \mu_n I_n(\beta r)] \cos(n(\theta - \epsilon_n)) \quad (6.14)$$

With unknown amplitude  $W_n$  and  $\cos(n(\theta - \epsilon_n))$  describing the circumferential variation:

$$\begin{aligned}\cos(n\epsilon_n) &= \frac{A_{1n}}{\tilde{W}_n} = \frac{A_{2n}}{\mu_n \tilde{W}_n} \\ \sin(n\epsilon_n) &= \frac{B_{1n}}{\tilde{W}_n} = \frac{B_{2n}}{\mu_n \tilde{W}_n}\end{aligned}\quad (6.15)$$

The boundary conditions of the plate described in Eq. (6.2) and Eq. (6.2) in terms of moment and shear force are:

$$\begin{aligned}M_{p,r=r_p} &= -D \left[ \frac{\partial^2 \tilde{u}_{z,p}}{\partial r^2} + \nu \left( \frac{1}{r} \frac{\partial \tilde{u}_{z,p}}{\partial r} + \frac{1}{r^2} \frac{\partial^2 \tilde{u}_{z,p}}{\partial \theta^2} \right) \right]_{r=r_p} = 0 \\ V_{p,r=r_p} &= \left\{ -D \frac{\partial}{\partial r} (\nabla^2 \tilde{u}_{z,p}) - \frac{1}{r} \frac{\partial}{\partial \theta} \left[ (1-\nu) D \left( \frac{1}{r} \frac{\partial^2 \tilde{u}_{z,p}}{\partial r \partial \theta} - \frac{1}{r^2} \frac{\partial^2 \tilde{u}_{z,p}}{\partial \theta^2} \right) \right] \right\}_{r=r_p} = 0\end{aligned}\quad (6.16)$$

Applying the boundary conditions Eq. (6.16) on Eq. (6.14). The equation is solved for  $\beta$ . The frequency equation corresponding to the free-edge plate is:

$$\left\{ \frac{\beta^2 r_p^2 \left( (\beta^4 r_p^4 + (1-\nu)^2 n^2 (n^2 - 1)) (J_{n-1}(\beta r_p) I_{n+1}(\beta r_p) + J_{n+1}(\beta r_p) I_{n-1}(\beta r_p)) \right)}{2n} - \frac{-2\beta^2 r_p^2 (1-\nu) n (n-1) I_{n-1}(\beta r_p) J_{n-1}(\beta r_p) + (n+1) I_{n+1}(\beta r_p) J_{n+1}(\beta r_p)}{2n} \right\} = 0 \quad (6.17)$$

Eq. (6.17) gives the natural frequencies for all values of  $n$  except for  $n = 0$ . The natural frequencies for  $n = 1$  are found by substituting in Eq. (6.17), resulting in:

$$1/2 \beta^2 r_p^2 (\beta^4 r_p^4 (J_0(\beta r_p) I_2(\beta r_p) + J_2(\beta r_p) I_0(\beta r_p)) - 4\beta^2 r_p^2 (1-\nu) I_2(\beta r_p) J_2(\beta r_p)) = 0 \quad (6.18)$$

The frequency equation for zero nodal diameters is:

$$\beta r_p (J_0(\beta r_p) I_1(\beta r_p) + I_0(\beta r_p) J_1(\beta r_p)) - (2-2\nu) I_1(\beta r_p) J_1(\beta r_p) = 0 \quad (6.19)$$

From both Eq. (6.18) and Eq. (6.19) the frequencies for respectively one and zero nodal diameters are found by:

$$\omega_{ns} = \beta_{ns}^2 \sqrt{\frac{D}{\rho_p t_p}} \quad (6.20)$$

Where  $\beta_{ns}$  are the roots of the frequency equations, in which  $s$  gives the number of nodal circles for each nodal diameter  $n$ . The corresponding modal shapes assuming  $\epsilon_n = 0$ .

$$\phi_{ns}(r, \theta) = [J_n(\beta_{ns} r) + \mu_{ns} I_n(\beta_{ns} r)] \cos(n\theta) \quad (6.21)$$

Where:

$$\mu_{ns} = \begin{cases} \frac{\left( \beta_{ns}^4 r_p^3 \left( -J_{n+1}(\beta_{ns} r_p) + \frac{n J_n(\beta_{ns} r_p)}{\beta_{ns} r_p} \right) + (1-\nu) n^2 \left( \beta_{ns}^2 r_p \left( -J_{n+1}(\beta_{ns} r_p) + \frac{n J_n(\beta_{ns} r_p)}{\beta_{ns} r_p} \right) - J_n(\beta_{ns} r_p) \right) \right)}{\left( \beta_{ns}^4 r_p^3 \left( I_{n+1}(\beta_{ns} r_p) + \frac{n I_n(\beta_{ns} r_p)}{\beta_{ns} r_p} \right) - (1-\nu) n^2 \left( \beta_{ns}^2 r_p \left( I_{n+1}(\beta_{ns} r_p) + \frac{n I_n(\beta_{ns} r_p)}{\beta_{ns} r_p} \right) - I_n(\beta_{ns} r_p) \right) \right)} & n \neq 0 \\ -\frac{J_1(\beta_{ns} r_p)}{I_1(\beta_{ns} r_p)} & n = 0 \end{cases} \quad (6.22)$$

The equation for of the anti-plane displacement of the plate is found by a summation of the modes.

$$\tilde{u}_{z,p} = \sum_{n=0}^{\infty} \sum_{s=0}^{\infty} A_{ns} \phi_{ns} \cos(n\theta) \quad (6.23)$$

The modal shapes are substituted in the equation of motion of the coupled system, Eq. (6.1) results in:

$$\sum_{n=0}^{\infty} \sum_{s=0}^{\infty} A_{ns} \{ D \beta_{ns}^4 \tilde{\phi}_{ns} - \rho_p t_p \omega^2 \tilde{\phi}_{ns} \} \cos(n\theta) + \sum_m \tilde{S}_{zm,s} = \sum_m \tilde{S}_{izm,s} \quad (6.24)$$

Since:

$$\nabla^4 \Phi_{ns} \cos(n\theta) = \beta_{ns}^4 \Phi_{ns} \cos(n\theta) \quad (6.25)$$

After some rewriting and substituting Eq. (6.7), the equation of motion is written as:

$$\sum_{n=0}^{\infty} \sum_{s=0}^{\infty} A_{ns} \left\{ (\omega_{ns}^2 - \omega^2) \rho_p t_p \tilde{\phi}_{ns} + \sum_m \mathbf{K}_{z-u_z} \tilde{\phi}_{ns} \right\} \cos(n\theta) + \mathbf{C}_x \tilde{S}_{ix,s} = \sum_m \tilde{S}_{izm,s} \quad (6.26)$$

### 6.1.2. Discretization of a circular area

The soil structure interface is discretized in single node circular elements. For every node, the SSI conditions are fulfilled. It is chosen to divide the circular plate into rings and divide the rings in elements such that the distance between the elements is about equal to the radius of a single ring. The location of the node within the ring is determined by the assumption that the angular rotation of the ring around  $r$  is constant over the element. The radius of the nodes within a ring is determined by figure 6.2 and Eq. (6.27).

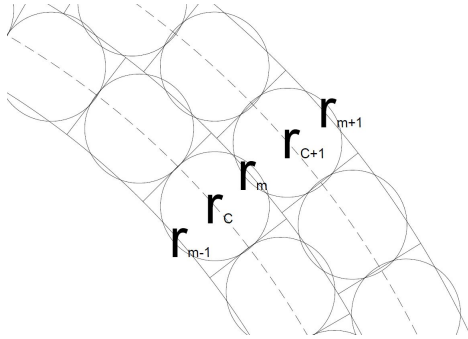


Figure 6.2: Schematization of the discretization of the 9th and 10th ring of a circle

$$\int_0^{2\pi} \int_{r_{m-1}}^{r_m} rCrdrd\theta = \int_0^{2\pi} \int_{r_{m-1}}^{r_m} rCr_cdrd\theta$$

$$\int_{r_{m-1}}^{r_m} rCrdr = \int_{r_{m-1}}^{r_m} rCr_mdr = \left[ \frac{1}{3}Cr^3 \right]_{r_{m-1}}^{r_m} = \left[ \frac{1}{2}Cr_l r^2 \right]_{r_{m-1}}^{r_m} \quad (6.27)$$

$$r_c = \frac{2}{3} \frac{r_m^3 - r_{m-1}^3}{r_m^2 - r_{m-1}^2}$$

In which  $C$  is a constant which describes the rotational angle of the element in  $r$ .  $r_m$  and  $r_{m-1}$  are respectively the outer and inner radius of the ring,  $r_c$  is the radius the nodes are put on, all visualized in figure 6.2. The number of elements in a ring are calculated from  $\frac{2r_c\pi}{r_m - r_{m-1}}$ . The influence area of a single element is determined by dividing the total area over the number of elements, and it is checked that the area of the every ring corresponds to the area of the elements in it. An example of a discretized plate in either 5 or 15 rings results and respectively 80 and 709 elements is shown in figure 6.3.

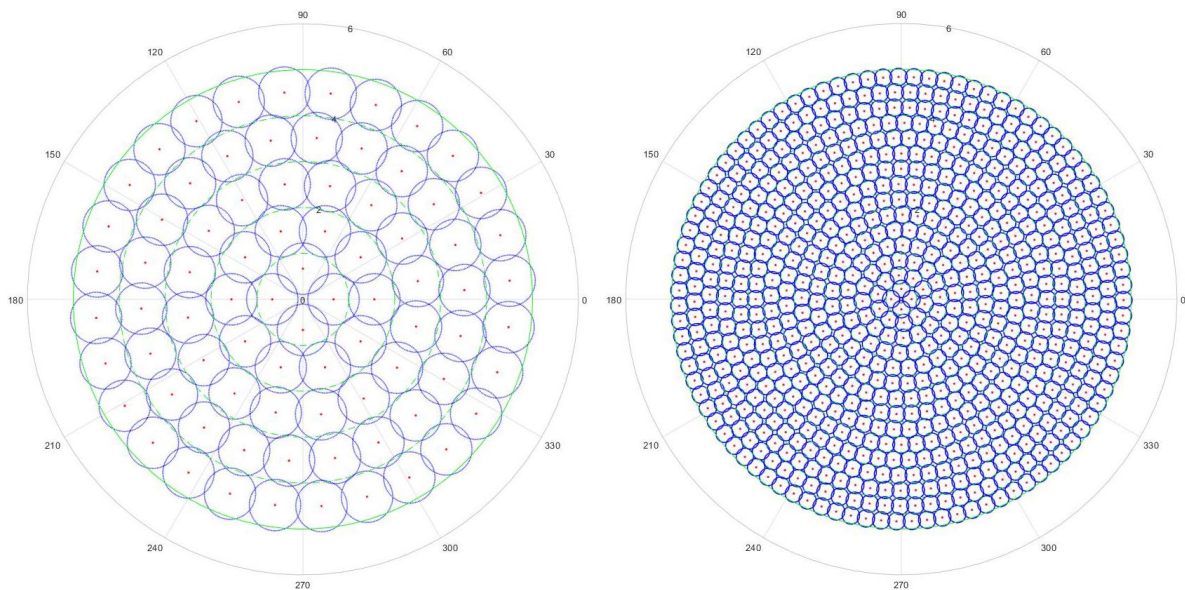


Figure 6.3: Discretization of a plate in either 80 or 709 elements.

## 6.2. Orthogonality of the structural modes

To determine which modes are activated and what their amplitude is, the principle of orthogonality is used, similar to the 2D case. The orthogonality equation applied in cylindrical coordinates is:

$$a_n \int_0^{2\pi} \int_0^{r_p} r \phi_{ns}(r) \cos(n\theta) \phi_{lt}(r) \cos(l\theta) dr d\theta \quad (6.28)$$

With the normalization constant  $a_n$ :

$$a_n = \begin{cases} \frac{1}{2\pi} & n = 0 \\ \frac{1}{\pi} & n \neq 0 \end{cases} \quad (6.29)$$

The orthogonality equation is separated into a the orthogonality in  $\theta$  and in  $r$ . The orthogonality equation in  $\theta$  results in:

$$\int_0^{2\pi} \cos(n\theta) \cos(l\theta) d\theta = \frac{1}{a_n} \delta_{nl} \quad (6.30)$$

So a cylindrical symmetric load cannot activate an antisymmetric deformation and vice versa. The orthogonality relation of Eq. (6.28) is rewritten as:

$$\int_0^{r_p} r \phi_{ns}(r) \phi_{lt}(r) \delta_{nl} dr = \Gamma \delta_{nl} \delta_{st} \quad (6.31)$$

The orthogonality relation is applied on Eq. (6.26) by premultiplying the equation with another modal deformation and integrating over  $r$  and  $\theta$ . Making use of Eq. (6.30) and putting all force components on the left-hand side, the equation results in:

$$\sum_{n=0}^{\infty} \sum_{s=0}^{\infty} A_{ns} \int_0^{r_p} r \tilde{\phi}_{lt} \left\{ (\omega_n^2 - \omega^2) \rho_p t_p \tilde{\phi}_{ns} + \sum_m \mathbf{K}_{z-u_z} \tilde{\phi}_{ns} \right\} \delta_{nl} dr = \int_0^{2\pi} \int_0^{r_e} r \tilde{\phi}_{lt} \left( \sum_m \tilde{S}_{izm,s} - \mathbf{C}_x \tilde{S}_{ix,s} \right) \cos(n\theta) d\theta dr \quad (6.32)$$

To solve Eq. (6.32) for every  $A_{ns}$ , the same amount of orthogonality equations are applied. The only two load cases considered are the cylindrical symmetric and antisymmetric. Therefore, only  $n, l = 0$  and  $n, l = 1$  are considered. Eq. (6.32) solved by numerical integration. Therefore, the modal shapes of the plate are discretized ( $\phi_{ij}(r) \cos(i\theta) = \boldsymbol{\phi}_{ij}$ ) the same way as the soil is. By making use of Eq. (6.31), Eq. (6.32) is:

$$\sum_{n=0}^1 \sum_{s=0}^{\infty} \sum_{l=0}^1 \sum_{t=0}^{\infty} A_{ns} [(\omega_n^2 - \omega^2) \rho_p t_p \Gamma_{nlst} + \tilde{\boldsymbol{\phi}}_{lt}^T \mathbf{K}_{z-u_z} \tilde{\boldsymbol{\phi}}_{ns} \delta_{nl}] = \tilde{\boldsymbol{\phi}}_{lt}^T (\tilde{\mathbf{S}}_{iz,s} - \mathbf{C}_x \tilde{S}_{ix,s}) \quad (6.33)$$

In which:

$$\Gamma_{nlst} = \tilde{\boldsymbol{\phi}}_{lt}^T \tilde{\boldsymbol{\phi}}_{ns} A_e \delta_{nl} \delta_{st} \quad (6.34)$$

And  $A_e$  is the area of a single element. Eq. (6.33) is solved for a finite number of circumferential modes  $s$  and  $t$ . The first modes are expected to have the most influence and the effect of higher modes declines quickly. The exact solution is accurately approached by choosing a sufficient large number of modes should. The equation in between the square brackets is called  $M$  and the right-hand side  $F$ . The unknowns are found for every discrete number of modes considered:

$$\begin{aligned} \mathbf{M}_{nslt} \mathbf{A}_{ns} &= \tilde{\mathbf{F}}_{lt} \\ \mathbf{A}_{ns} &= \mathbf{M}_{nslt}^{-1} \tilde{\mathbf{F}}_{lt} \end{aligned} \quad (6.35)$$

The vertical displacement is found by substituting Eq. (6.35) in Eq. (6.23). The horizontal displacement are found by Eq. (6.8).

### 6.3. 3D SSI case study

For the 3D SS case study presented in this section, ten circumferential symmetric modes and ten antisymmetric modes including the rigid body modes are considered, describing the vertical motion of the plate. The plate is assumed inextensible, and therefore the horizontal displacement is described by only the horizontal rigid body motion. The first five circumferential symmetric and antisymmetric modes of the plate are shown in figure 6.4. The plate considered in this section has a five meter radius and one meter thickness. The E-

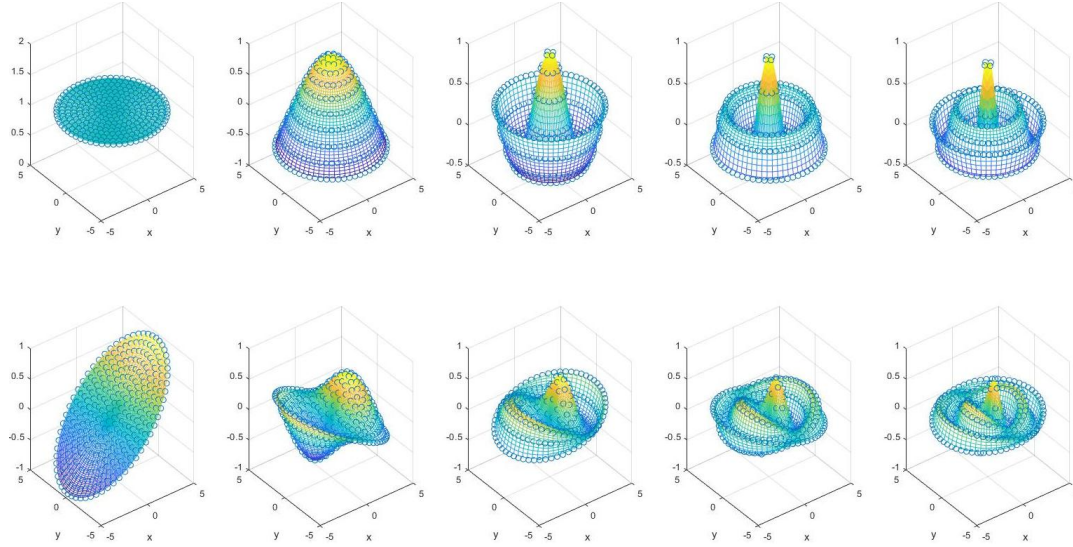


Figure 6.4: The first five circumferential symmetric (top) and antisymmetric (bottom) modes of a free-edge plate

modulus of the plate is  $30 * 10^9 \text{ N/m}^2$  and the Poisson's ratio is set to 0.33. The natural frequencies of the plate, that correspond to the modes in figure 6.4 are given in table 6.1. The response of the plate due to a

Mode	n=0	n=1
0	0	0
1	62 Hz	141 Hz
2	265 Hz	411 Hz
3	604 Hz	818 Hz
4	1078 Hz	1360 Hz

Table 6.1: Natural frequencies of the free-edge plate

horizontal and vertical uniform incident displacement fields are evaluated for the frequencies: 3.09 Hz and 19.30 Hz. The wavelength of the Rayleigh wave corresponding to these frequencies and the soil properties considered, is almost 37 and 7 meters based on Eq. (6.36). In the next sections the response of the plate for incident displacement fields is evaluated and a comparison with a Winkler model subject to same loading is made.

$$\lambda_r = \frac{c_r}{\omega} \approx \frac{0.862 + 1.14\nu}{1 + \nu} \frac{c_s}{\omega} \quad (6.36)$$

#### Incident uniform vertical displacement

Due to an incident uniform vertical displacement of  $10^{-3}$  m, the cylindrical symmetric modes ( $n=0$ ) of the plate are activated. The plate itself has no horizontal displacement due to the symmetry and the fact that it has been set inextensible. However, the inertial interaction of the foundation plates generates waves propagating away from the plate, with both a vertical and a horizontal amplitude. The wavelength at both frequencies in x and z seems to correspond to the wavelength of the Rayleigh wave.

Due to an incident harmonic displacement of the soil at 3.09 Hz, shown in figure 6.5, the plate mainly deforms in its first modal shape, however, this amplitude is very small and less than 5% of the incident displacement.

This is reasonable since the frequency of excitation is significantly lower than the first natural frequency of the plate. The soil displacement is dominant and the plate only deviate slightly due to the mass inertia. As expected, the stresses are the largest at the edges of the plate due to stress distribution. The stress distribution of the vertical stress is symmetric and the stress in  $x$  antisymmetric. The resultant interaction force in  $x$  is equal to zero and cause no rotation of the plate. Therefore, the plate stays at its horizontal position.

At 19.30 Hz, shown in figure 6.6, the deformation of the plate is more significant. The difference between top and center is almost 10 % of the incident displacement. This is reasonable since the frequency of excitation is closer to the first natural frequency of the soil. Stress patterns are similar to those of at 3.09 Hz, except a phase difference for the interaction stresses in  $x$ .

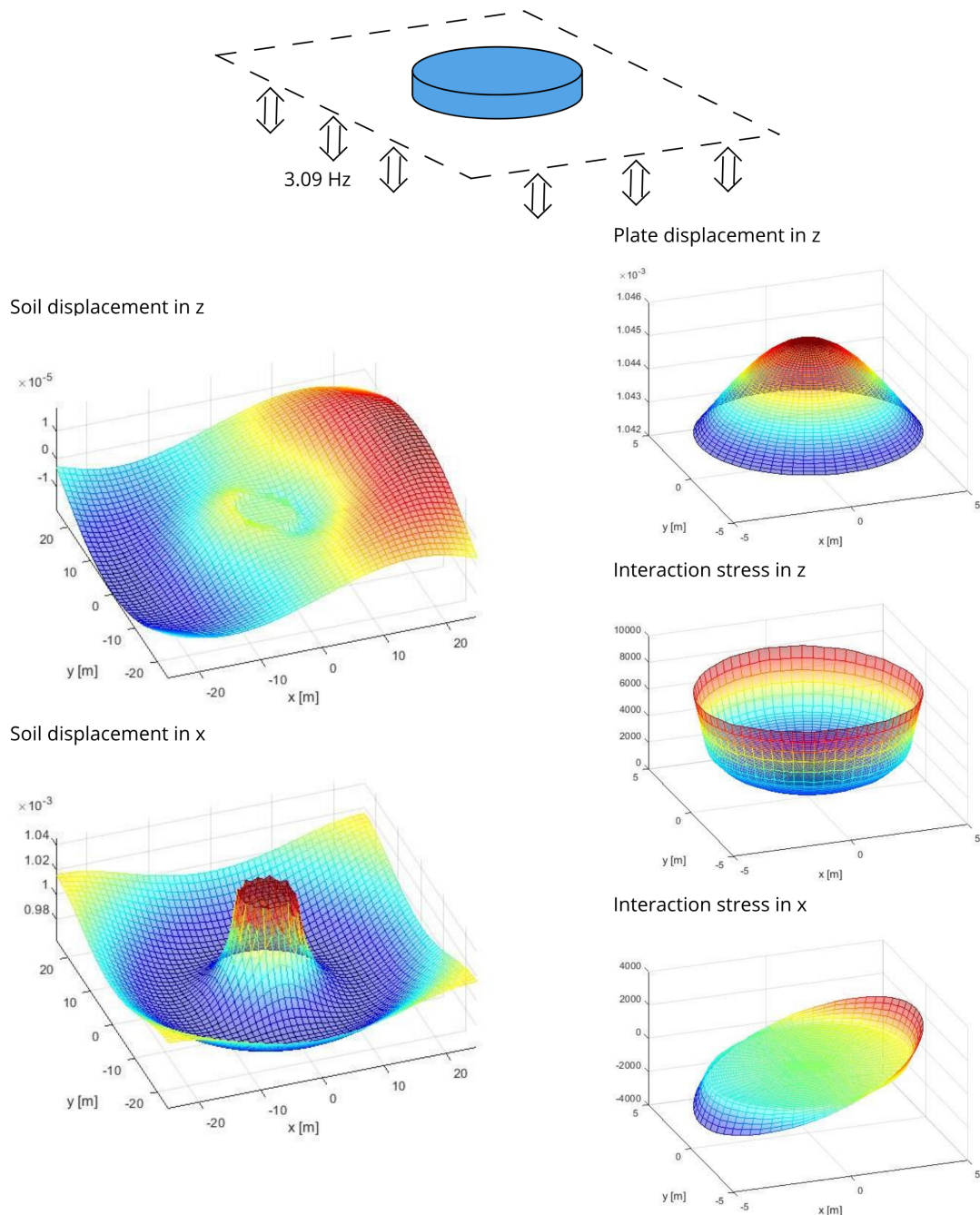


Figure 6.5: Response of a plate excited at 3.09 Hz with an incident uniform vertical displacement

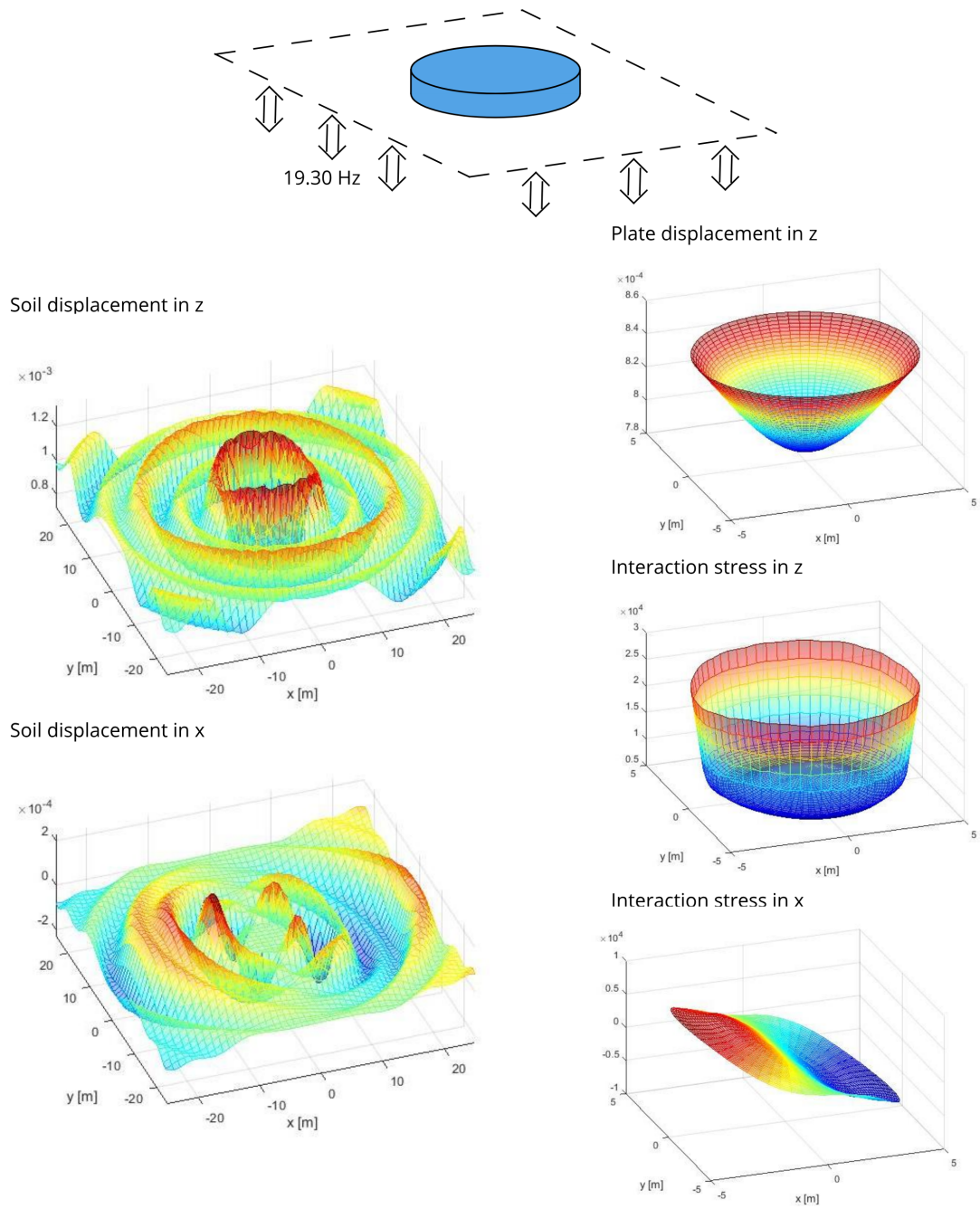


Figure 6.6: Response of a plate excited at 19.30 Hz with an incident uniform vertical displacement

**Incident uniform horizontal displacement**

The horizontal motion of the soil, excites the plate both horizontally and vertically. The plate deforms in the antisymmetric mode shapes. Figure 6.7 and figure 6.8 show the deformations and stresses at 3.09 Hz and 19.30 Hz respectively. In both cases, the rigid body rotation is dominant in the displacement in  $z$ . Furthermore, the amplitude of the vertical displacement due to a horizontal motion is 1% and 10% of the incident motion at 3.09 Hz and 19.30 Hz respectively. The higher frequency causes more rotation what is reasonable since the wavelength of the waves, generated from the motion of the plate is shorter for high frequencies, and therefore the plate rotates more. The wave length of the vertical wave seems to be related to the Rayleigh wave. However, the dominant wave length for both frequencies in  $x$  is longer than the Rayleigh wave. The wave propagating in  $x$  could relate to a compressional wave, with a wavelength of 15 m and 96 m at 3.09 Hz and 19.30 Hz respectively.

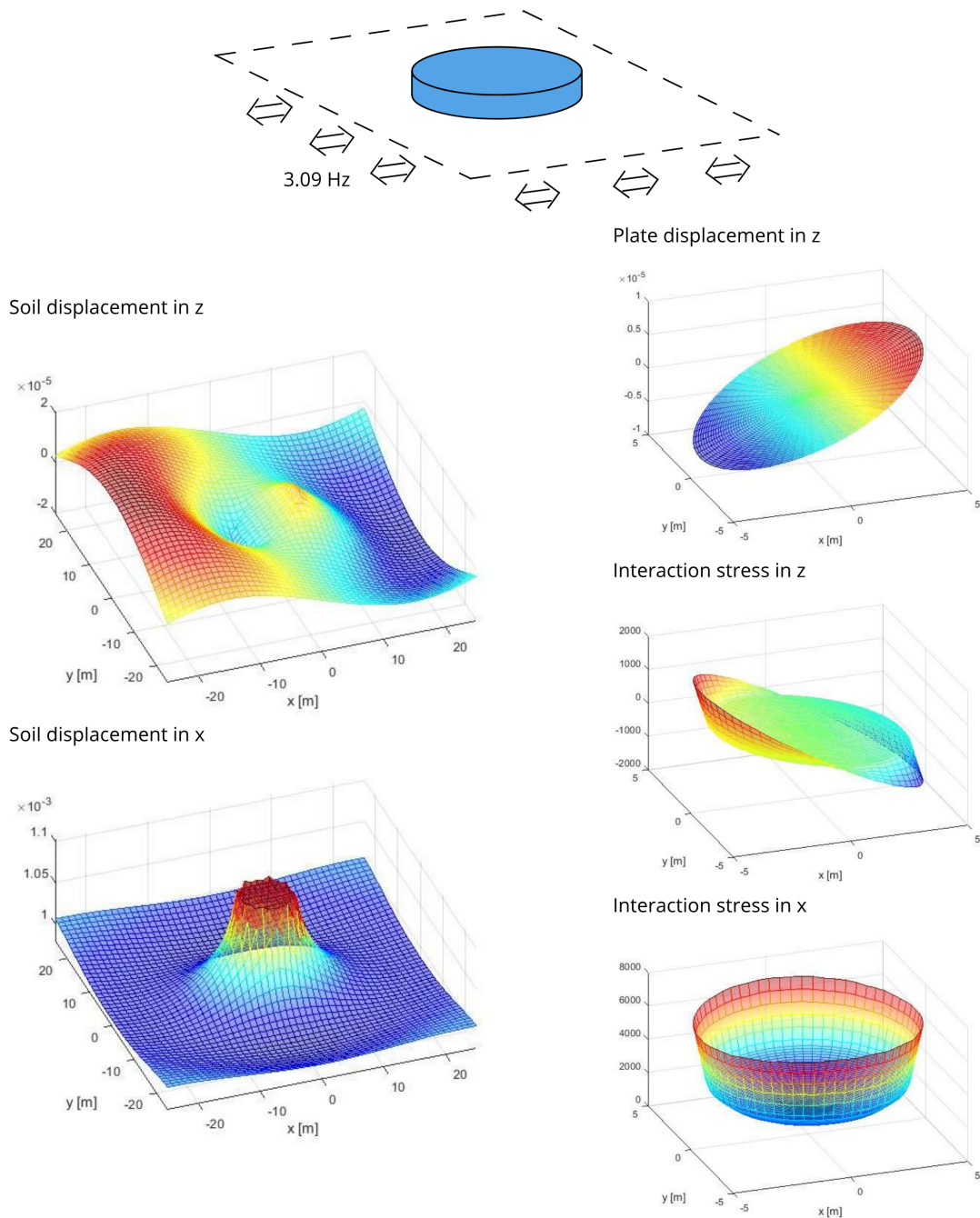


Figure 6.7: Response of a plate excited at 3.09 Hz with an incident uniform displacement in  $x$

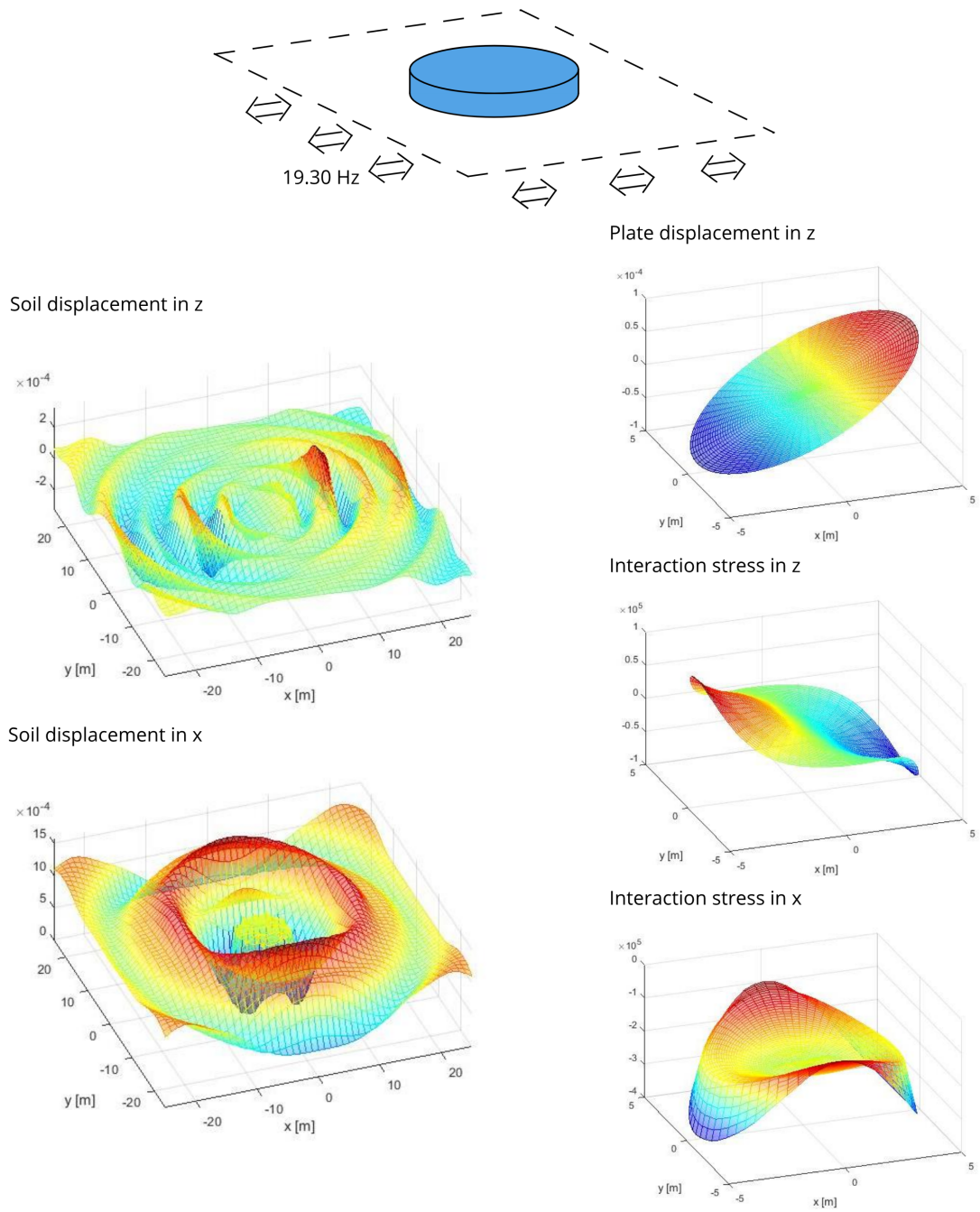


Figure 6.8: Response of a plate excited at 19.30 Hz with an incident uniform displacement in x

### Comparison with Winkler springs

A comparison is made with a independent Winkler spring foundation at 3.09 Hz and 19.30 Hz. The complex stiffness for the Winkler springs is determined by work of Gazetas (1983). The vertical stiffness and damping are determined by:

$$\begin{aligned} K_z &= \frac{4\mu r_p}{1-\nu} \left( 1 + 1.28 \frac{r_p}{h} \right) \\ C_z &= \frac{3.4r_p^2}{1-\nu} \sqrt{\mu\rho} \\ \mathbf{K} &= K_z + i\omega C_z \end{aligned} \quad (6.37)$$

The stiffness and damping is taken constant over the area. Figure 6.9 shows the deformations of the plate foundation on both a linear elastic soil layer and on Winkler springs due to a uniform incident vertical displacement of  $10^{-3}$  m. The results differ strongly, especially at 19.30 Hz, where the deformation of the plate on Winkler springs is 10 times smaller than the foundation plate in the linear elastic soil model and there is a significant phase difference. Furthermore it is noticeable that the deformation of the plate at 3.09 Hz is contrary. This can be explained by the independency of the Winkler springs along the foundation. Since the plate displacement is larger than the incident displacement of the soil, the edges of the plate should have the smallest displacement to be continuous with the soil. The stress distribution of both differ as well, since the stress distribution of the Winkler springs is exactly the same as the deformation shape, while in the linear elastic model the stresses are located at the edge. Furthermore, only the vertical case is considered. Because the plate is inextensible in  $x$  and the Winkler spring model does not couple the horizontal and vertical displacement, the horizontal system reduces to a SDOF system. It is tricky and uncommon to couple the vertical and horizontal stiffness in the Winkler spring model. Therefore, the Winkler model does not include the effects of a coupled vertical and horizontal soil, e.g. it is unable to capture the rotation of the foundation due to a horizontal incident displacement. Aforementioned, the effects of coupling the horizontal and vertical displacements, up to 10% of the incident displacement, is observed in ?? and ?. This confirms the relevance of this phenomena, which is not captured by the Winkler model.

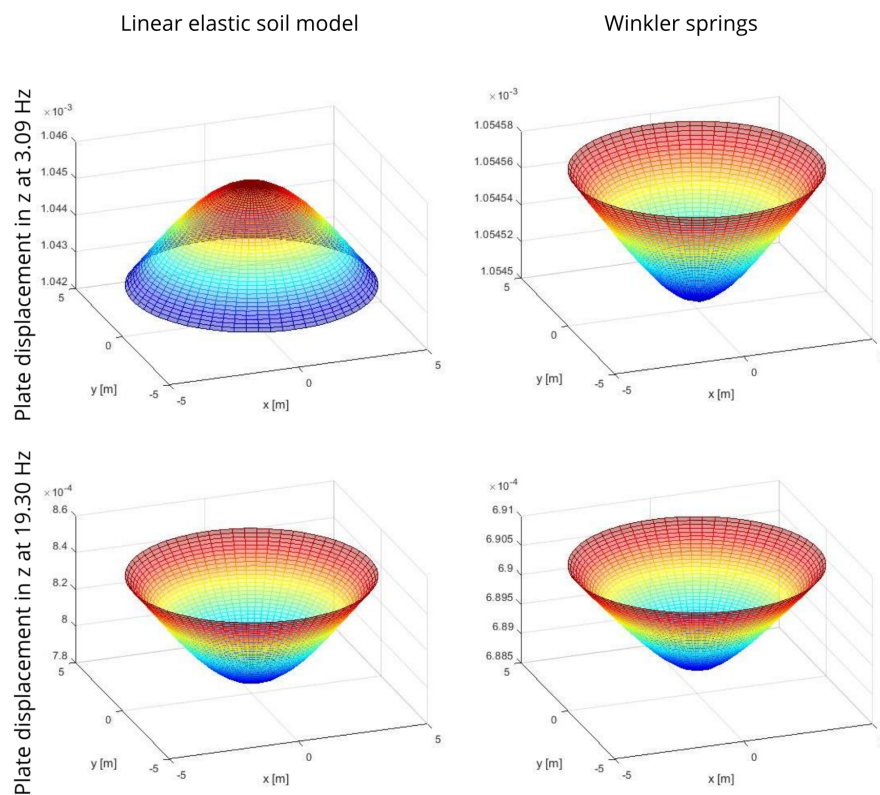


Figure 6.9: Comparison of the vertical displacement with a Winkler spring model at 3.09 Hz and 19.30 Hz

## 6.4. Influence of the flexibility of a circular plate

The flexibility of a foundation plate influences the kinematic SSI. To determine the influence of the flexibility of the foundation, inertial forces are not included. All forcing is done by either a uniform, parabolic ( $2p_0(1 - r^2/r_p^2)$ ) or linear decreasing (rocking) vertical load on top of the foundation, representing a force from the super structure. The system equation of motion. Therefore, Eq. (6.33) is rewritten into:

$$\sum_{n=0}^1 \sum_{s=0}^{\infty} \sum_{l=0}^1 \sum_{t=0}^{\infty} A_{ns} [D\beta_{ns}^A \Gamma_{nlst} + \tilde{\phi}_{lt}^T \mathbf{K}_{z-u_z} \tilde{\phi}_{ns} \delta_{nl}] = \tilde{\phi}_{lt}^T \tilde{\mathbf{S}}_{iz,s} \quad (6.38)$$

The stiffness of the foundation influences the interaction stresses. Therefore, variation in the foundation stiffness influences the complex stiffness of the system. Richart et al. (1970) show that the stress distribution of a machine foundation can influence both period and stiffness of system. The influence of the flexibility of the

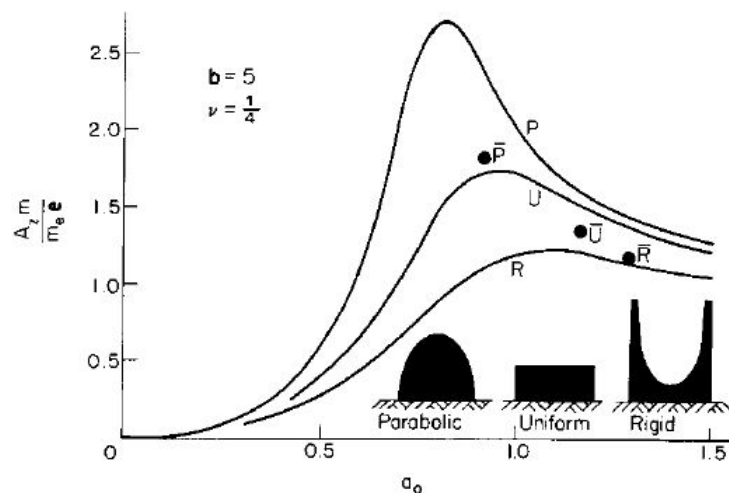


Figure 6.10: Influence of stress distribution on frequency-dependent stiffness. (source: (Richart et al., 1970))

circular plate is determined for two plates with  $\frac{h}{r_p}$  ratio 4 and 25. The stiffness of the system is determined similar as in the 2D case, schematized in figure 6.11. The average stiffness is determined based on the average displacement of the plate. The edge and center stiffness are determined by the displacement of an element respectively closest to the edge and closest to the center of the plate. The difference in stiffness of the system including a flexible foundation are compared with respect to the rigid stiffness. The comparison is made for the edge, center and average stiffness, shown in table 6.2 and table 6.3 for circular plates with ratio  $\frac{h}{r_p}$  4 and 25. The flexibility of the plate is quantified by Eq. (4.29). The effect of the variation in flexibility of the plate is approximately constant for low frequencies with respect to the radius of the plate, as shown in figure 6.12 to figure 6.15. At high frequencies, it is hard to quantify the effect of the flexibility due to resonances, however a change in global stiffness is clearly visible. It is also shown that, a plate with a larger radius is more sensitive to resonance. Therefore, the values in table 6.3 are more reliable than table 6.2. The  $\frac{h}{r_p}$  ratio does not seem to affect the stiffness significantly. The stiffness is influenced by different resonance patterns of the soil layer as discussed in section 5.6.2. Therefore, the results of ratio  $\frac{h}{r_p} = 25$  in table 6.3 are used to draw conclusions.

Figure 6.12 to figure 6.15 show that the average stiffness and damping of the system reduce for flexible plates, with respect to rigid plates. The average stiffness is reduced with 6% for flexible plates under a constant harmonic load. The average damping is more sensitive and reduces with 11%. Figure 6.16 to figure 6.19 show the variation in stiffness at the edge and center of the plate, due to a variation of the foundation stiffness. At the center the stiffness and damping are reduced three times the reduction of the average stiffness and damping. Contrary at the edge, the stiffness and damping increase with respectively 11% and 29%. In case of a parabolic load case, the effect of the reduced foundation stiffness is similar but the effect is twice as large for all cases.

In general, the rocking stiffness is more sensitive to variation in stiffness of the foundation. The average stiffness and damping can reduce with respectively 14% and 23% observed from table 6.3. At the center the

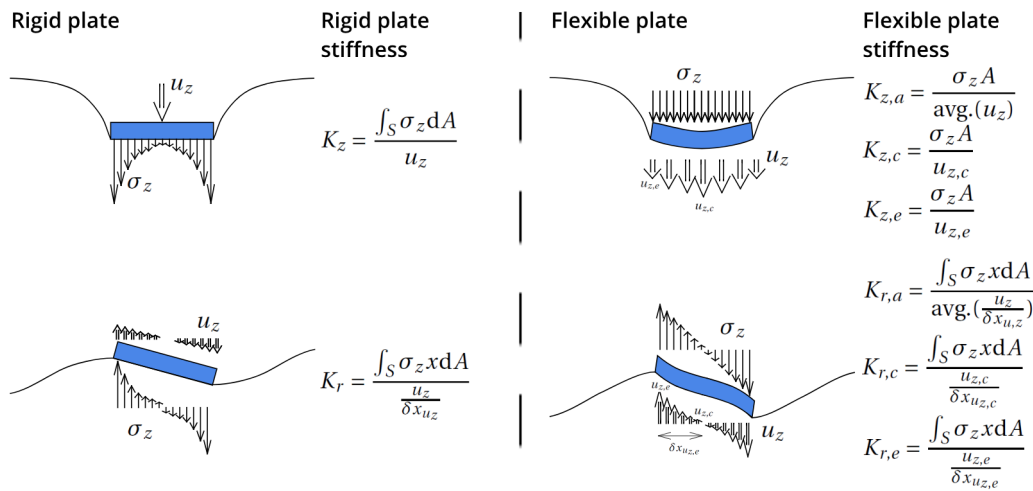


Figure 6.11: Schematization and formulation on how the stiffness is determined

reduction can even be respectively 36% and 58%, while at the edge the stiffness and damping respectively increase with 15% and 33%. Compared to the vertical stiffness, the SSI is more sensitive to the flexibility of the plate for rocking. For a low flexibility indicated with 0-0.01, the effect on the complex rocking stiffness compared to the complex vertical stiffness is about 2-3 times larger, while for a flexibility indicated by 0.1-1 the effect is 3-5 times larger. So also for foundations with a moderate stiffness, SSI is important.

Previous research of Gazetas (1983) describes static stiffness reduction factors of a flexible, circular plate on a half space for both a uniform and parabolic load and the same definition of the flexibility. The reduction found by Gazetas (1983) of the average static stiffness due to the flexibility of the plate is significantly larger than found in this thesis, namely -23%, -28%, -8%, -1% and 0% due to a uniform load and -54%, -46%, -18%, -3% and -2% due to a parabolic load corresponding with flexibility indicated by 0.01, 0.1, 1, 10 and 100 respectively. The difference can be declared by the half-space that is considered. Since a half-space does not consider a bedrock boundary, a higher possible flexibility is assumed, while the layer with bedrock is restricted for vertical displacements. Furthermore, Gazetas (1983) determines the average stiffness out of the average of the edge and center displacement, while in this thesis the displacement is over the area, which is more influenced by the edge displacements than the center displacements. For both reasons it is reasonable that the results are slightly different but it is clear that the flexibility of the foundation does influence SSI strongly.

	Average stiffness			Average damping			Center stiffness			Center damping			Edge stiffness		Edge damping			
	$k_z$	$k_r$	$c_r$	$c_z$	$cr$	$kz$	$kr$	$c_z$	$c_r$	$k_z$	$k_r$	$c_z$	$c_r$	$k_z$	$k_r$	$c_z$	$c_r$	
<b>RF</b>	<i>const.</i>	<i>para.</i>		<i>const.</i>	<i>para.</i>		<i>const.</i>	<i>para.</i>		<i>const.</i>	<i>para.</i>		<i>const.</i>	<i>para.</i>		<i>const.</i>	<i>para.</i>	
<b>0</b>	-7%	-11%	-18%	-9%	-17%	-25%	-19%	-35%	-61%	-28%	-58%	-60%	3%	29%	10%	15%	67%	29%
<b>0.001</b>	-5%	-10%	-18%	-1%	-10%	-25%	-17%	-34%	-40%	-23%	-54%	-60%	5%	30%	10%	25%	76%	29%
<b>0.01</b>	-5%	-10%	-18%	-1%	-10%	-25%	-17%	-34%	-40%	-23%	-54%	-59%	5%	30%	10%	25%	76%	29%
<b>0.1</b>	-5%	-10%	-18%	-1%	-10%	-25%	-17%	-34%	-40%	-23%	-54%	-59%	5%	30%	10%	24%	76%	29%
<b>1</b>	-5%	-10%	-18%	-1%	-10%	-25%	-17%	-34%	-40%	-23%	-54%	-59%	5%	29%	10%	22%	74%	27%
<b>10</b>	-4%	-8%	-16%	-1%	-8%	-23%	-16%	-30%	-41%	-21%	-49%	-61%	4%	24%	7%	16%	58%	20%
<b>100</b>	-2%	-4%	-9%	0%	-3%	-14%	-7%	-14%	-27%	-8%	-26%	-44%	2%	8%	3%	6%	18%	8%

Table 6.2: Relative SSI stiffness and damping for a cylindrical plate over a single layer on bedrock ( $\frac{h}{r_p} = 4$ )

	Average stiffness			Average damping			Center stiffness			Center damping			Edge stiffness			Edge damping					
	$k_z$	$k_r$	$c_z$	$c_r$	$kz$	$kr$	$c_z$	$cr$	$kz$	$kr$	$c_z$	$cr$	$kz$	$kr$	$c_z$	$cr$	$kz$	$kr$	$c_z$	$cr$	
<b>RF</b>	<i>const.</i>	<i>para.</i>																			
<b>0</b>	-4%	-12%	-14%	-11%	-22%	-13%	-20%	-39%	-36%	-37%	-64%	-58%	11%	22%	5%	29%	67%	33%			
<b>0.001</b>	-5%	-11%	-14%	-11%	-22%	-13%	-20%	-39%	-36%	-36%	-64%	-58%	11%	22%	15%	28%	67%	31%			
<b>0.01</b>	-5%	-11%	-14%	-10%	-21%	-12%	-20%	-38%	-36%	-36%	-63%	-51%	10%	21%	13%	26%	63%	27%			
<b>0.1</b>	-4%	-8%	-12%	-7%	-16%	-20%	-16%	-31%	-36%	-30%	-54%	-58%	7%	14%	9%	16%	40%	17%			
<b>1</b>	-1%	-3%	-4%	-2%	-5%	-8%	-5%	-11%	-15%	-10%	-21%	-28%	2%	3%	3%	4%	8%	5%			
<b>10</b>	0%	-1%	0%	0%	-1%	-1%	-1%	-2%	-2%	-1%	-4%	-4%	0%	0%	1%	0%	0%	1%			
<b>100</b>	0%	-1%	0%	0%	-1%	0%	0%	-1%	0%	0%	-1%	0%	0%	-1%	0%	0%	-1%	0%			

Table 6.3: Relative SSI stiffness and damping for a cylindrical plate over a single layer on bedrock ( $\frac{h}{r_p} = 25$ ).

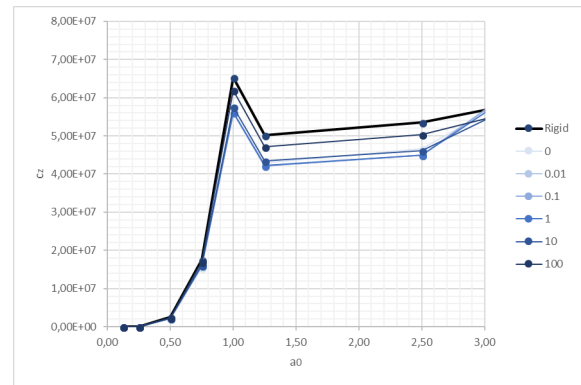
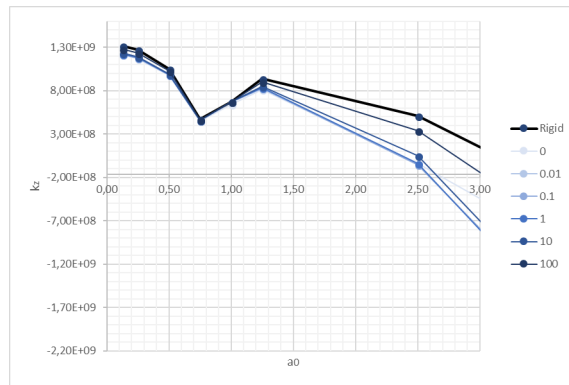


Figure 6.12: Average damping under the plate for a variation in flexibility of the plate ( $\frac{h}{r_p} = 4$ )

Figure 6.13: Average damping under the plate for a variation in flexibility of the plate ( $\frac{h}{r_p} = 4$ )

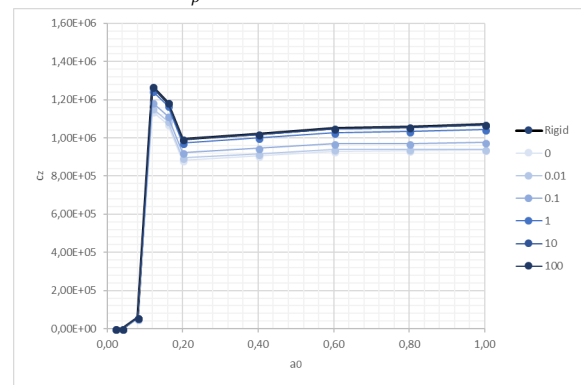
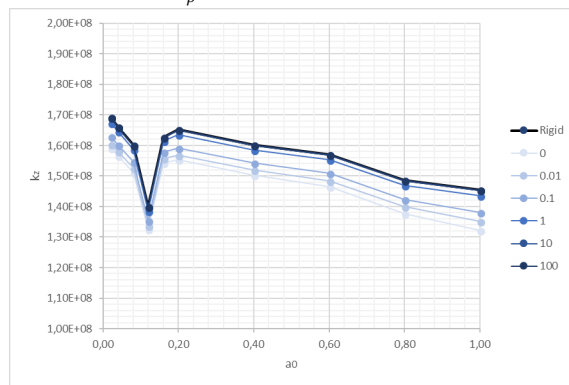


Figure 6.14: Average stiffness under the plate for a variation in flexibility of the plate ( $\frac{h}{r_p} = 25$ )

Figure 6.15: Average damping under the plate for a variation in flexibility of the plate ( $\frac{h}{r_p} = 25$ )

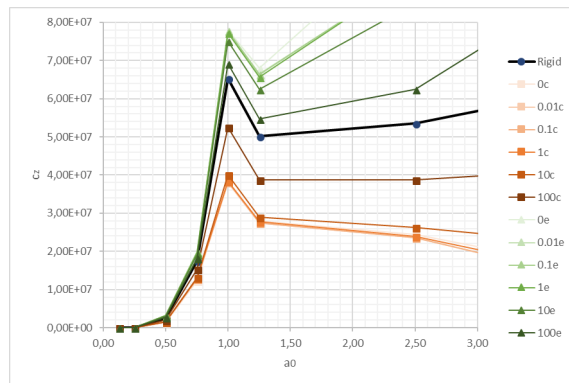
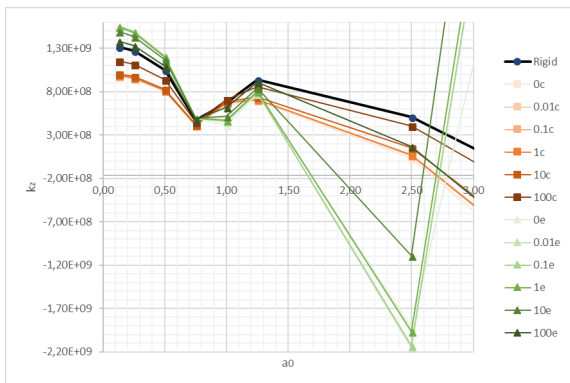


Figure 6.16: Stiffness at the edge (e) and at the center (c) for a variation in flexibility of the plate ( $\frac{h}{r_p} = 4$ )

Figure 6.17: Damping at the edge (e) and at the center (c) for a variation in flexibility of the plate ( $\frac{h}{r_p} = 4$ )

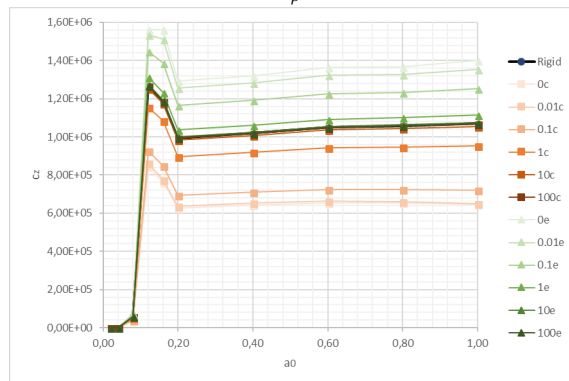
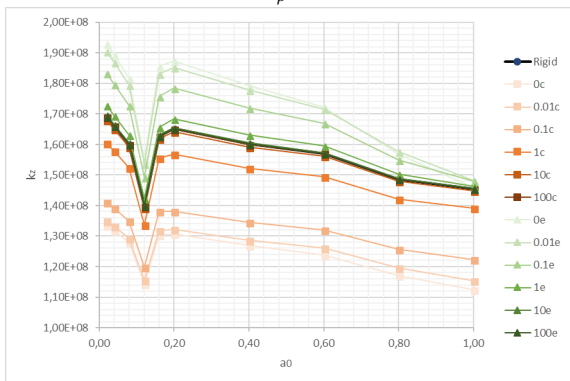


Figure 6.18: Stiffness at the edge (e) and at the center (c) for a variation in flexibility of the plate ( $\frac{h}{r_p} = 25$ )

Figure 6.19: Damping at the edge (e) and at the center (c) for a variation in flexibility of the plate ( $\frac{h}{r_p} = 25$ )



# 7

## Conclusions, recommendations and discussion

This chapter covers the conclusions and recommendations follow from both 2D and 3D case. In addition, selected methods, assumptions made and possible further generalizations are discussed.

### 7.1. Conclusions

To conclude on the research subquestions, the method is evaluated and compared to other methods in a stepwise manner, the validation is discussed and interesting results among other about the influence of a flexible foundation are presented. Hereafter the research question is answered.

#### The modelling method

The main objective of this thesis is the development of a powerful mathematical semi-analytical calculation model for SSI. The model is based on fundamental physics, starting from the wave equation for a linear elastic material without damping. The geometry of the model is based on a single layer over bedrock. The soil behaviour is described by potentials and these are solved for in the wavenumber (2D) or Hankel (3D) - frequency domain. The translation back to the space domain is proceeded by making use of contour integration and the residue theorem, resulting in Green's functions. By superposition of the Green's function, a stiffness matrix describing the complex soil behaviour is created. The soil is combined with a superstructure by numerical integration and the principle of orthogonality.

The foundation used during this thesis is assumed to be inextensible in-plane. However, coupling to an inextensible plate is not a limitation of the model. Since the soil is discretized, the soil model can even be applied on a FEM structure.

Further details of this model cannot be captured in a few sentences and for this information the reader is advised to read the corresponding preceding chapters.

- The Green's functions of the soil are determined by making use of Helmholtz potentials. This turned out to be a convenient way to describe the soil behaviour. The soil boundary conditions could be solved in either the wavenumber or Hankel domain which both turned out to give a correct solution.
- The solution method makes use of contour integration and the residue theorem. Therefore, the convergence of Green's functions, describing the soil flexibility are strongly sensitive to the number of (complex) roots included. This holds especially for forces concentrated on a small area relative to the soil layer depth.
- The interaction model is not capable to allow for gaps or sliding because the interaction stresses of model and foundation are equal at any moment.

Compared to other modelling methods described in section 2.3, the obtained model has the following added values:

- The flexibility of the foundation is included in the developed model while the foundation is often assumed rigid in simplistic models. Moreover, the shift of natural period of the coupled model can be observed by including the flexibility of the foundation.
- Compared to simplistic models, phase differences of soil motion at different locations of the foundation and radiation damping are captured by the model.
- Frequency-dependent stiffness and damping are included, while many simplified models assume a frequency independent stiffness and damping.
- Due to the method used to couple both soil and structure, the stiffness matrix of the soil only needs to be derived once per frequency. Since this is the only relatively 'time consuming' step in the analysis, large benefits in terms of computational effort is achieved compared to FE modelling of the soil.

### Validation of the model

The developed and implemented SSI model is validated by comparison with earlier derived analytical solution of both the static (2D & 3D) and dynamic (3D) stiffness of a rigid foundation on a layer over bedrock. The dynamic validation cases available in literature are not exactly identical to the calculations performed with the newly developed model. For example, material damping differs. These deviations are caused by the limited time that was left at the stage of model validation combined and the fact that reference papers not in all cases did present the results for exactly the model parameters that were used in the analysis of the present study.

The static stiffness for both 2D and 3D model are observed to be within a 7% error compared with the validation cases included from literature. The dynamic trends are the same for low frequencies and differences can clearly be explained. For frequencies expected during an earthquake, the interaction is sensitive to only a small number of foundation modes. On the contrary, the number of (complex) soil modes influences the SSI outcome strongly. The number of interaction elements is sufficient when a full sinusoidal wave is described with at least 6 elements. For the studied range of frequencies and load cases considered, including 10 foundation modes and 100 soil modes should be sufficient.

### Results

The soil response shows a strong frequency dependency. Interesting results obtained from the model concerning the behavior of the soil are:

- Due to the absence of hysteretic damping the stiffness of the model is strongly sensitive to resonance frequencies of the soil.
- Both vertical and horizontal stiffness are strongly sensitive to a variation in frequency. The vertical stiffness decays strongly at the frequency of the fundamental compressional mode of the soil layer, while the horizontal stiffness is sensitive to the frequency of the fundamental shear mode of the soil layer. The rocking stiffness is moderately sensitive to the frequency and shows a linear decay with increasing frequency.
- No damping is observed before the cut-off frequency for propagating waves of the soil layer. Due to the bedrock boundary, energy cannot dissipate in vertical direction and since propagating waves cannot exist for these frequencies, no energy dissipate in horizontal direction.
- In 3D, geometrical spreading of energy over the surface reduces the amplitude of propagating waves compared with the 2D case.

The complex SSI stiffness depends on the stiffness of the foundation. The variation in complex SSI stiffness for flexible foundations with respect to the rigid foundations is observed for different frequencies. It can be concluded that:

- Depending on the type of load, the average stiffness and damping for low frequencies can reduce respectively with up to ~20% and ~25% for a small flexible foundations compared with rigid foundations.
- The distribution of the system stiffness depends on the stiffness of the foundation. Generally, the stiffness and damping contributions at the edges increase for a decreasing foundation stiffness and vice versa for the center of the foundation.

- The rocking stiffness and damping is more sensitive to the flexibility of the foundation compared to the vertical stiffness.
- The flexibility of the foundation influences the complex SSI stiffness strongly for high frequencies within the earthquake domain. However, the influence is hard to quantify or generalize due to resonance of the soil layer, variation in stiffness and damping for flexible and non flexible foundations is clearly noticeable.

**Research question: Develop and implement a semi analytical analysis method to describe SSI for rigid and flexible shallow foundations on soil.**

During this thesis a model is developed which is able to couple a superstructure to soil, the model is able to capture frequency dependency and the flexibility of a foundation. Moreover, the model describes radiation damping and takes into account phase differences at the interaction plane in 2D and 3D. Therefore, the model overcomes problems that are associated to simplistic models. The soil model is able to be combined with any other linear model by linear superposition. The coupling can be done, either by matching modes or by coupling to a superstructure model with a discretized SSI interface.

## 7.2. Recommendations

The modelling technique needs further improvement and validation before it can be used to its full extent in practice. The authors recommend the following main improvements to be implemented in the present model:

- It is recommended to include hysteretic damping in the model to reduce the sensibility on the resonance frequencies of the soil. Therefore, another root finder algorithm needs to be used since the one used for this thesis cannot find the propagating roots when material damping is included.
- The model is based on a single layer on a bedrock. A situation that is not representative for real cases. The model could be extended with additional layers to improve the usability.
- The model needs additional validation e.g. by a comparison with a FE model, also for more complex situations.

### 7.3. Discussion

During the development of the model, selections for methods, techniques, and assumptions have been made. After finishing the entire thesis some reflection on the selected approach is valuable. The modelling technique used in this thesis starts from the derivation of Green's functions and describes the behaviour of the soil by superposition of Green's functions.

A stress block is used instead of a point load. In my opinion this is a justified choice, since it does overcome a singularity at the origin. Moreover, force distributed over the area of an element represents the average behaviour of a single element better than a point load at its center.

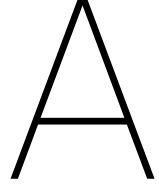
The Green's functions are derived by contour integration and applying the residue theorem. This procedure is exact when all roots are included, however there are infinite many roots. Therefore, there is always a reduction in accuracy. This especially plays a role for relative small elements with respect to the height of the soil layer.

The interaction is established by discretizing the modal deformations of the foundation and match Green's functions to the elements. The displacement of both soil and structure are solved by applying the orthogonality principle on the kinematic equilibrium, i.e. the global system of equation of motion. From my perspective this is not the most straight-forward method of combining both soil and structure. I think that the soil model developed in this thesis fits better on a discretized super structure. For a simple beam or plate, a dynamic stiffness matrix can be formed and the coupling is straight forward omitting the principle of orthogonality. For coupling soil to a superstructure which is described in the summation of modes, it is more straight forward to describe the soil as well in a summation of modes. The amplitudes of the modes can be coupled and the problem can be solved for linearly without discretization by matching modes and making use of the principle of orthogonality. Then, the accuracy of the solution can be determined by convergence, while the accuracy is now partly determined by engineering judgement.

However the object of this thesis was to develop a model that describes SSI and is generalized such that it is applicable on multiple applications. Moreover, the model should allow coupling with a fluid-tank superstructure which behaviour is described by a summation over modes. The present model is able to do both. However, applying the model on a structure response described by the summation of modes is concluded to be less straight-forward.

Finally, extending the model with soil material damping will give significant added value. Excluding soil material damping as done in this thesis provides interesting insights in the physical phenomena related to SSI and radiation damping. However, by including soil material damping the frequency dependent sensitivity to resonances will reduce and results will become more realistic, representing the actual SSI response of systems.





## Rewriting the Hankel transform

In this appendix, an integral over a Bessel J function from 0 to  $a$  is rewritten into an integral from  $-a$  to  $a$  premultiplied with both a symmetric and antisymmetric function. Both occur often as result of a (inverse) Hankel transform.

### A.1. An integral over a Bessel J transform premultiplied with an antisymmetric function

In the first case considered, the Bessel J function is premultiplied with a linear antisymmetric equation  $\xi$ .

#### A.1.1. A cylindrical symmetric load ( $n=0$ )

Rewriting the integral over a Bessel J function starting from:

$$\int_0^a \xi J_0(\xi) d\xi \tag{A.1}$$

$$J_0(\xi) = \frac{1}{2} \left( H_0^{(1)}(\xi) + H_0^{(2)}(\xi) \right) \tag{A.2}$$

$$\int_0^a \xi J_0(\xi) d\xi = \frac{1}{2} \int_0^a \xi \left( H_0^{(1)}(\xi) + H_0^{(2)}(\xi) \right) d\xi \tag{A.3}$$

Since the BesselJ function is purely real:

$$\int_0^a \xi J_0(\xi) d\xi = \int_0^a \xi \Re(J_0(\xi)) d\xi = \frac{1}{2} \int_0^a \xi \left( \Re(H_0^{(1)}(\xi)) + \Re(H_0^{(2)}(\xi)) \right) d\xi \tag{A.4}$$

For  $\xi > 0$  it holds that:

$$\Re(H_0^{(1)}(\xi)) = \Re(H_0^{(2)}(\xi)) \tag{A.5}$$

and

$$\int_0^a \xi \Re(H_0^{(2)}(\xi)) d\xi = \int_0^a \xi \Re(H_0^{(1)}(\xi)) d\xi \tag{A.6}$$

Substitute Eq. (A.6) into Eq. (A.4):

$$\int_0^a \xi \Re(J_0(\xi)) d\xi = \int_0^a \xi \Re(H_0^{(1)}(\xi)) d\xi = \int_0^a \xi \Re(H_0^{(2)}(\xi)) d\xi \tag{A.7}$$

For  $\xi \rightarrow -\xi$ :

$$\int_0^a \xi \Re(H_0^{(1)}(\xi)) d\xi = \int_0^{-a} -\xi \Re(H_0^{(1)}(-\xi)) - d\xi = - \int_{-a}^0 \xi \Re(H_0^{(1)}(-\xi)) d\xi \quad (\text{A.8})$$

Due to antisymmetry:

$$-\Re(H_0^{(1)}(-\xi)) = \Re(H_0^{(1)}(\xi)) \quad (\text{A.9})$$

Therefore:

$$\int_{-a}^a \xi \Re(H_0^{(1)}(\xi)) d\xi = \int_{-a}^0 \xi \Re(H_0^{(1)}(\xi)) d\xi + \int_0^a \xi \Re(H_0^{(1)}(\xi)) d\xi = 2 \int_0^a \xi \Re(H_0^{(1)}(\xi)) d\xi \quad (\text{A.10})$$

Substitute Eq. (A.10) into Eq. (A.7):

$$\int_0^a \xi \Re(J_0(\xi)) d\xi = \frac{1}{2} \int_{-a}^a \xi \Re(H_0^{(1)}(\xi)) d\xi \quad (\text{A.11})$$

Considering the combination of both real and imaginary parts of the Hankel function:

$$\int_{-a}^a \xi (H_0^{(1,2)}(\xi)) d\xi = \int_{-a}^a \xi \Re(H_0^{(1,2)}(\xi)) d\xi + \int_{-a}^a \xi \Im(H_0^{(1,2)}(\xi)) d\xi \quad (\text{A.12})$$

Due to symmetry of the imaginary parts:

$$\int_{-a}^a \xi \Im(H_0^{(1,2)}(\xi)) d\xi = 0 \quad (\text{A.13})$$

Therefore:

$$\int_0^a \xi J_0(\xi) d\xi = \frac{1}{2} \int_{-a}^a \xi H_0^{(1)}(\xi) d\xi \quad (\text{A.14})$$

Furthermore:

$$\frac{1}{2} \int_{-a}^a \xi H_0^{(1)}(\xi) d\xi = \int_{-a}^a \xi J_0(\xi) d\xi - \frac{1}{2} \int_{-a}^a \xi H_0^{(2)}(\xi) d\xi \quad (\text{A.15})$$

Due to the symmetry of the Bessel J function for  $n = 0$ :

$$\int_{-a}^a \xi J_0(\xi) d\xi = 0 \quad (\text{A.16})$$

For  $a = \infty$ , this results in:

$$\int_0^{\infty} \xi J_0(\xi) d\xi = \frac{1}{2} \int_{-\infty}^{\infty} \xi H_0^{(1)}(\xi) d\xi = -\frac{1}{2} \int_{-\infty}^{\infty} \xi H_0^{(2)}(\xi) d\xi \quad (\text{A.17})$$

### A.1.2. An antisymmetric case (n=1)

Simpler than the axissymmetric case the Bessel J function of  $n = 1$  is antisymmetric therefore, for  $\xi \rightarrow -\xi$ :

$$\int_0^a \xi J_1(\xi) d\xi = \frac{1}{2} \int_{-a}^a \xi J_1(\xi) d\xi \Rightarrow \int_0^{\infty} \xi J_1(\xi) d\xi = \frac{1}{2} \int_{-\infty}^{\infty} \xi J_1(\xi) d\xi \quad (\text{A.18})$$

## A.2. A integral over a Bessel J transform premultiplied with a symmetric function

In the first case considered, the Bessel J function is premultiplied with a symmetric quadratic equation  $\xi^2$ . The approach is similar to the case of an antisymmetric premultiplication.

### A.2.1. A cylindrical symmetric load (n=0)

The solution to the cylindrical symmetric load is rather obvious since the Bessel J function itself is also symmetric for  $n = 0$ . Therefore, for  $\xi \rightarrow -\xi$ :

$$\int_0^a \xi^2 J_0(\xi) d\xi = \int_0^{-a} \xi^2 J_0(-\xi) - d\xi = \int_{-a}^0 \xi^2 J_0(-\xi) d\xi = \int_{-a}^0 \xi^2 J_0(\xi) d\xi \quad (\text{A.19})$$

Therefore:

$$\int_0^a \xi^2 J_0(\xi) d\xi = \frac{1}{2} \int_{-a}^a \xi^2 J_0(\xi) d\xi \Rightarrow \int_0^\infty \xi^2 J_0(\xi) d\xi = \frac{1}{2} \int_{-\infty}^\infty \xi^2 J_0(\xi) d\xi \quad (\text{A.20})$$

### A.2.2. An antisymmetric case (n=1)

The antisymmetric case starts from:

$$\int_0^a \xi^2 J_1(\xi) d\xi = \frac{1}{2} \int_0^a \xi^2 (H_1^{(1)}(\xi) + H_1^{(2)}(\xi)) d\xi \quad (\text{A.21})$$

Since the Bessel J function is purely real:

$$\int_0^a \xi^2 J_1(\xi) d\xi = \int_0^a \xi^2 \Re(J_1(\xi)) d\xi = \frac{1}{2} \int_0^a \xi^2 (\Re(H_1^{(1)}(\xi)) + \Re(H_1^{(2)}(\xi))) d\xi \quad (\text{A.22})$$

For  $\xi > 0$  it holds that:

$$\Re(H_1^{(1)}(\xi)) = \Re(H_1^{(2)}(\xi)) \quad (\text{A.23})$$

and

$$\int_0^a \xi^2 \Re(H_1^{(2)}(\xi)) d\xi = \int_0^a \xi^2 \Re(H_1^{(1)}(\xi)) d\xi \quad (\text{A.24})$$

Substitute Eq. (A.24) into Eq. (A.22):

$$\int_0^a \xi^2 \Re(J_1(\xi)) d\xi = \int_0^a \xi^2 \Re(H_1^{(1)}(\xi)) d\xi = \int_0^a \xi \Re(H_1^{(2)}(\xi)) d\xi \quad (\text{A.25})$$

For  $\xi \rightarrow -\xi$ :

$$\int_0^a \xi^2 \Re(H_1^{(1)}(\xi)) d\xi = \int_0^{-a} \xi^2 \Re(H_1^{(1)}(-\xi)) - d\xi = \int_{-a}^0 \xi^2 \Re(H_1^{(1)}(-\xi)) d\xi \quad (\text{A.26})$$

Due to symmetry of Eq. (A.26):

$$\Re(H_1^{(1)}(-\xi)) = \Re(H_1^{(1)}(\xi)) \quad (\text{A.27})$$

Therefore:

$$\int_{-a}^a \xi^2 \Re(H_1^{(1)}(\xi)) d\xi = \int_{-a}^0 \xi^2 \Re(H_1^{(1)}(\xi)) d\xi + \int_0^a \xi^2 \Re(H_1^{(1)}(\xi)) d\xi = 2 \int_0^a \xi^2 \Re(H_1^{(1)}(\xi)) d\xi \quad (\text{A.28})$$

Substitute Eq. (A.28) into Eq. (A.25):

$$\int_0^a \xi^2 \Re(J_1(\xi)) d\xi = \frac{1}{2} \int_{-a}^a \xi^2 \Re(H_1^{(1)}(\xi)) d\xi \quad (\text{A.29})$$

Considering the combination of both real and imaginary parts of the Hankel function:

$$\int_{-a}^a \xi (H_0^{(1,2)}(\xi)) d\xi = \int_{-a}^a \xi \Re(H_0^{(1,2)}(\xi)) d\xi + \int_{-a}^a \xi \Im(H_0^{(1,2)}(\xi)) d\xi \quad (\text{A.30})$$

Due to antisymmetry of the imaginary parts:

$$\int_{-a}^a \xi^2 \Im(H_1^{(1,2)}(\xi)) d\xi = 0 \quad (\text{A.31})$$

Therefore:

$$\int_0^a \xi^2 J_1(\xi) d\xi = \frac{1}{2} \int_{-a}^a \xi^2 H_1^{(1)}(\xi) d\xi \quad (\text{A.32})$$

Furthermore:

$$\frac{1}{2} \int_{-a}^a \xi^2 H_1^{(1)}(\xi) d\xi = \int_{-a}^a \xi^2 J_1(\xi) d\xi - \frac{1}{2} \int_{-a}^a \xi^2 H_1^{(2)}(\xi) d\xi \quad (\text{A.33})$$

Due to the antisymmetry of the Bessel J function for  $n = 1$ :

$$\int_{-a}^a \xi^2 J_1(\xi) d\xi = 0 \quad (\text{A.34})$$

For  $a = \infty$ , this results in:

$$\int_0^\infty \xi^2 J_2(\xi) d\xi = \frac{1}{2} \int_{-\infty}^\infty \xi^2 H_1^{(1)}(\xi) d\xi = -\frac{1}{2} \int_{-\infty}^\infty \xi^2 H_1^{(2)}(\xi) d\xi \quad (\text{A.35})$$

### A.2.3. General solution

In general, there are four cases. The combination of a symmetric and antisymmetric Bessel J premultiplied with either a symmetric (even) or antisymmetric (odd) function. The symmetric and antisymmetric Bessel J functions correspond respectively to an even or odd  $n$ . Therefore, the general solution may be written as:

$$\int_0^a f(\xi) J_n(\xi) d\xi = \begin{cases} \frac{1}{2} \int_{-a}^a f(\xi) H_n^{(1)}(\xi) d\xi = -\frac{1}{2} \int_{-a}^a f(\xi) H_n^{(2)}(\xi) d\xi & f(\xi) = \text{odd} \quad \& \quad n = \text{even} \\ \frac{1}{2} \int_{-a}^a f(\xi) J_n(\xi) d\xi & f(\xi) = \text{odd} \quad \& \quad n = \text{odd} \\ \frac{1}{2} \int_{-a}^a f(\xi) J_n(\xi) d\xi & f(\xi) = \text{even} \quad \& \quad n = \text{even} \\ \frac{1}{2} \int_{-a}^a f(\xi) H_n^{(1)}(\xi) d\xi = -\frac{1}{2} \int_{-a}^a f(\xi) H_n^{(2)}(\xi) d\xi & f(\xi) = \text{even} \quad \& \quad n = \text{odd} \end{cases} \quad (\text{A.36})$$

# B

## Derivation of the potential representation of the displacement by Helmholtz decomposition

A generalized derivation of the coupling of between P- and SV-waves and the independent SH-wave is performed in here based on work of Aki and Richards (2002). Starting from the wave equations based on Lamé's theorem:

$$\begin{aligned}\ddot{\phi} &= \frac{\Phi}{\rho} + \alpha^2 \nabla^2 \phi \\ \ddot{\boldsymbol{\psi}} &= \frac{\boldsymbol{\Psi}}{\rho} + \beta^2 \nabla^2 \boldsymbol{\psi}\end{aligned}\tag{B.1}$$

Eq. (B.1) is satisfied by potentials related to displacement  $\boldsymbol{u}$  and force  $\boldsymbol{f}$  via:

$$\begin{aligned}\boldsymbol{u} &= \nabla \phi + \nabla \times \boldsymbol{\psi} \\ \boldsymbol{f} &= \nabla \Phi + \nabla \times \boldsymbol{\Psi}\end{aligned}\tag{B.2}$$

With:

$$\begin{aligned}\nabla \cdot \boldsymbol{\psi} &= 0 \\ \nabla \cdot \boldsymbol{\Psi} &= 0\end{aligned}\tag{B.3}$$

The wave equations, Eq. (B.1) are equivalent to three scalar equations:

$$\begin{aligned}\ddot{\phi} &= \frac{\Phi}{\rho} + \alpha^2 \nabla^2 \phi \\ \frac{d^2}{dt^2} (\nabla \times \boldsymbol{\psi})_z &= \frac{1}{\rho} (\nabla \times \boldsymbol{\Psi})_z + \beta^2 \nabla^2 [(\nabla \times \boldsymbol{\psi})_z] \\ \ddot{\psi}_z &= \frac{\Psi_z}{\rho} + \beta^2 \nabla^2 \psi_z\end{aligned}\tag{B.4}$$

In absence of body forces, Eq. (B.4) can be decomposed into three kinds of motion; namely those which two out of the three functions  $\phi$ ,  $(\nabla \times \boldsymbol{\psi})_z$  and  $\psi_z$  vanish everywhere:

For  $(\nabla \times \boldsymbol{\psi})_z$  and  $\psi_z$  equal to zero, clearly the P-waves motion remains:

$$\boldsymbol{u} = \nabla \phi\tag{B.5}$$

For  $\phi$  and  $\psi_z$  equal to zero and  $\nabla \cdot \boldsymbol{\psi} = 0$ ,  $\frac{\partial \psi_x}{\partial x} + \frac{\partial \psi_y}{\partial y} = 0$ . Therefore, some function  $M$  exists that  $\psi_x = \frac{\partial M}{\partial y}$  and  $\psi_y = -\frac{\partial M}{\partial x}$ , i.e.  $\boldsymbol{\psi} = \nabla \times (0, 0, M)$ . It is chosen to rename  $M$  as scalar  $\psi$ . The remaining wave is in the category that describes SV-waves:

$$\boldsymbol{u} = \nabla \times \nabla \times (0, 0, \psi)\tag{B.6}$$

$\phi$  and  $(\nabla \times \psi)_z$  equal to zero corresponds to  $\nabla \cdot \mathbf{u} = 0$  and  $\mathbf{u}_z = 0$ . Therefore, the displacement is like  $\boldsymbol{\psi}$  in the previous situation. Therefore, a function  $\chi$  exists, like  $M$  and the motion is clearly like a SH-wave.

$$\mathbf{u} = \nabla \times (0, 0, \chi) \quad (\text{B.7})$$

Combining the aforementioned results in the displacement field in terms of potentials. Similarly, the three types of body forces can be described:

$$\begin{aligned} \mathbf{u} &= \nabla\phi + \nabla \times \nabla \times (0, 0, \psi) + \nabla \times (0, 0, \chi) \\ \mathbf{f} &= \nabla\Phi + \nabla \times \nabla \times (0, 0, \Psi) + \nabla \times (0, 0, X) \end{aligned} \quad (\text{B.8})$$

Where the P-, SV- and SH- wave equations being respectively:

$$\begin{aligned} \ddot{\phi} &= \frac{\Phi}{\rho} + \alpha^2 \nabla^2 \phi \\ \ddot{\psi} &= \frac{\Psi}{\rho} + \beta^2 \nabla^2 \psi \\ \ddot{\chi} &= \frac{X}{\rho} + \beta^2 \nabla^2 \chi \end{aligned} \quad (\text{B.9})$$

# Bibliography

- Keiiti Aki and Paul G. Richards. *Quantitative Seismology, Second Edition-University Science Books*. University Science Books Sausalito, California, second edi edition, 2002.
- Khairina A. Canny. *Seismic Response of Liquid Storage Tank in a Semi Analytical Method*. Master thesis, TU Delft, 2018.
- Aron Caselunghe and Jonas Eriksson. *Structural Element Approaches for Soil-Structure Interaction*. PhD thesis, Chalmers University of Technology, 2012.
- Consultants Joint Venture. *Soil-Structure Interaction for Building Structures*. *Nehrp*, 2012.
- Ricardo Dobry, Issa Oweis, and Alfredo Urzua. Simplified procedures for estimating the fundamental period of a soil profile. *Bull. Seism. Soc. Am.*, 66(4):1293–1321, 1976. URL <http://www.bssaonline.org/content/66/4/1293.short>.
- Gillian R. Foulger, Miles P. Wilson, Jon G. Gluyas, Bruce R. Julian, and Richard J. Davies. Global review of human-induced earthquakes. Technical Report July, 2017. URL <http://dx.doi.org/10.1016/j.earscirev.2017.07.008>.
- George Gazetas. Analysis of Machine foundation vibration, state of the art. *Structural Dynamics and Earthquake Engineering*, 2(1):1–42, 1983.
- P. J P Gonçalves, M. J. Brennan, and S. J. Elliott. Numerical evaluation of high-order modes of vibration in uniform Euler-Bernoulli beams. *Journal of Sound and Vibration*, 301(3-5):1035–1039, 2007. ISSN 10958568. doi: 10.1016/j.jsv.2006.10.012.
- Paul Hölscher. *Soil dynamics in urban areas*. TU Delft, 2016.
- Eduardo Kausel. *Forced vibrations of circular foundations on layered media.pdf*. PhD thesis, Massachusetts Institute of Technology, 1974.
- Eduardo Kausel. *Fundamental solutions in elastodynamics. A compendium*. Cambridge University Press, 2006. ISBN 9788578110796. doi: 10.1017/CBO9781107415324.004.
- MIT OpenCourseWare. *Introduction to Seismology (12.510)*. 2008.
- George Mylonakis, Costis Syngros, George Gazetas, and Takashi Tazoh. The role of soil in the collapse of 18 piers of Hanshin expressway in the Kobe earthquake. *Earthquake Engineering and Structural Dynamics*, 35(5):547–575, 2006. ISSN 10969845. doi: 10.1002/eqe.543.
- Normcommissie 351 001 "Technische Grondslagen voor Bouwconstructies". NPR 9998: Assessment of buildings in case of erection, reconstruction and disapproval – Basic rules for seismic actions: induced earthquakes. Technical Report december, Nederlands Normalisatie-instituut, Delft, 2015.
- Frank Press. The role of science and engineering in mitigating natural hazards. *Bulletin of the new zealand national society ofr earthquake engineering*, 18(2):4, 1985.
- J. S. Rao. *Dynamics of Plates*. Narosa Publishing House, Narosa, 1999. ISBN 81-7319-250-2.
- E.E. Richart, J.R. Hall, and R.D. Wood. *Vibrations of Soils and Foundations*. Prentice-Hall, Inc, Michigan, 1970. ISBN 13-91716-8.
- Rob Semper. Faultline: Seismic Science at the Epicenter, 2017. URL <http://www.exploratorium.edu/faultline/index.html>.

- Johanathan P. Stewart, Gergory L. Fenves, and Raymond B. Seed. Seismic Soil-Structure Interaction in Buildings. I: Analytical Methods. *Journal of geotechnical and geoenvironmental engineering*, 125(January):26–37, 1999.
- Jelena Tomic. Are Love- and Rayleigh seismic waves detectable in Groningen? Technical Report June, NAM, 2017.
- A Tsouvalas. *Underwater noise generated by offshore pile driving*. PhD thesis, Delft University of Technology, 2015.
- Karel N. Van Dalen. *Body waves in an elastic continuum & Rayleigh waves at the free surface*. 2015.
- Arnold Verruijt. *An Introduction to Soil Dynamics*. Springer, Dordrecht, 2010. ISBN 9789048134403. doi: <https://doi.org/10.1007/978-90-481-3441-0>.
- John P. Wolf. *Dynamic soil-structure interaction*. Number 1. Prentice-Hall, Englewood Cliffs, 1985. ISBN 0-13-221565-9.